Two-dimensional discontinuous Galerkin shallow water model for practical flood modelling applications

Janice Lynn Ayog

A thesis submitted in partial fulfilment of the requirements
for the degree of Doctor of Philosophy

Department of Civil and Structural Engineering
Faculty of Engineering
The University of Sheffield

September 2021

Declaration

I, Janice Lynn Ayog, confirm that the thesis is my own work. I am aware of the University's Guidance on the Use of Unfair Means (www.sheffield.ac.uk/ssid/unfair-means). This work has not previously been presented for an award at this, or any other, university.

Janice Lynn Ayog
September 2021

Abstract

Finite volume (FV) numerical solvers to the two-dimensional shallow water equations are the foundation of the current state-of-the-practice, industry-standard flood models. The second-order Discontinuous Galerkin (DG2) alternative show a promising way to improve current FV-based flood model formulations, but is yet under-studied and rarely utilised to support flood modelling applications. This is contributed by the mathematical complexity constructed within the DG2 formulation that could lead to large computational costs and compromise its stability and robustness when used for practical modelling. Therefore, this PhD research aims to develop a new flood model based on simplified DG2 solver that is improved for flood modelling practices. To achieve this aim, three objectives have been formed and addressed through analyses involving academic and experimental test cases, as well as test cases that are recommended by the UK Environment Agency to validate 2D flood model capabilities, whilst benchmarking the simplified DG2 solver against four FV-based industrial models. Key research findings indicate that the simplified DG2 solver can equally retain conservative properties and provide second-order accurate predictions as the standard DG2 solver whilst offering around 2.6 times runtime speed up. Additionally, the simplified DG2 solver can be reliably efficient to provide predictions close to the outputs of industrial models, in simulating flood scenarios covering large catchment-scale areas and at a grid resolution $\geq$ 5 m, particularly when the local limiting is disabled. However, the local limiting is still needed by the simplified DG2 solver when modelling detailed velocity fields at sub-metre grid resolutions, particularly in regions of highly active wave-structure interactions as commonly encountered in urban flooding around steep-sloped building structures.

Acknowledgements

I would like to thank my supervisors, Dr Georges Kesserwani and Dr Domenico Bau, for their continual guidance and mentoring throughout my PhD research. I would also like to thank the members (both former and current) of the SEAMLESS-WAVE research group, namely Dr James Shaw, Dr Mohammd Kazem Sharifian, Mohammad Shirvani and Sun Xitong, for many constructive discussions that helped me address questions and challenges encountered in my research. To Mercedes, Gaby, Henry, Emma, Bastian, Rosa and the rests of my office mates, I thank you for the making my research life in the university a memorable one.

I would like to remember those who have supported me mentally and emotionally, particularly during the global pandemic of Covid-19. I thank the members of the Go Global ladies support group who have provided emotional and spiritual care whilst I juggle between PhD-related works and my caring responsibilities during the national lockdowns in the UK. I also thank the Online Writing Club in the Universiti Malaysia Sabah for the constant writing supports and encouragements during long period of movement control orders in Malaysia. To those I have not named, I am forever indebted for the support they have indirectly provided during this challenging period.

Special appreciation goes to my two children, Jia and Joel, who have been my constant source of happiness, and also to my husband, Jurin Gunsalam, who dutifully ensures that our family are always well taken care of whilst I focus on working on my research. I would also like to thank my parents, Ayog and Betty, and my siblings with their families for their continued blessings and encouragement. I dedicate this PhD research to you all.

Table of Contents

List of Figures

List of Tables

Nomenclature

β	Parameter of the Sweby symmetric limiter
Δx	Spatial grid size in x-direction
Δy	Spatial grid size in y-direction
Ω	2D computational domain
∂_t	partial derivatives of time
∂_x	partial derivatives of the horizontal distance
∂_x	partial derivatives of the vertical distance
ϕ	Slope limiter function
$\mathbf{F(U)}$	x-directional spatial flux vector
$\mathbf{G(U)}$	y-directional spatial flux vector
$\mathbf{S(U)}$	Source term vectors
$\mathbf{U}$	Vector of state (or flow) variables
$\mathbf{U}^0$	Mean coefficient of flow variables
$\mathbf{U}^{1x}$	x-slope coefficient of flow variables
$\mathbf{U}^{1y}$	y-slope coefficient of flow variables

$\mathbf{U_h}$	DG2 approximation of the state (or flow) variables
t	Time
x	Coordinate along the horizontal axis of a plane/longitudinal distance in a channel
y	Coordinate along the vertical axis of a plane/lateral distance in a channel
1D	One-dimension
2D	Two-dimension
3D	Three-dimension
CFL	Courant-Friedrichs-Lewy
DEM	Digital Elevation Model
DG2-LL	DG2 solver with local limiter
DG2-NL	DG2 solver without local limiter
DG2	Second-order Discontinuous Galerkin
DG	Discontinuous Galerkin
E	Energy
FV1	First-order finite volume
FV2	Second-order finite volume
FV	Finite volume
MUSCL	Monotonic Upstream-centred Scheme for Conservation Laws
M	Mass
NS	Navier Stokes
PIV	Particle image velocimetry

RI	Relevance index
RK2	Second-order Runge-Kutta time integration
R^2	Correlation coefficient
SWE	Shallow water equations
TVD	Total Variation Diminishing
c	Reference index of spatial grid element
E	East
G	Gaussian points
g	gravitational acceleration
h	Water depth
i	Reference index for the grid element faces and Gaussian points
K	Reference index for DG2 coefficients/operators
M_Q	Number of grids in x-direction
N	North
n_M	Manning's roughness coefficient
N_Q	Number of grids in y-directions
N_s	The size of time series/Number of samples
nei	Neighbouring element
p	Reference index for the grid faces
Q	Grid element
q_x^0	Mean discharge in x-direction

q_y^0	Mean discharge in y-direction
q_x^{1x}	x-directional slope discharge in x-direction
q_y^{1x}	x-directional slope discharge in y-direction
q_x^{1y}	y-directional slope discharge in x-direction
q_y^{1y}	y-directional slope discharge in y-direction
q_x	x-directional flow discharge
q_y	y-directional flow discharge
r	Radial distance
S	South
T	Simulation output time
u	x-directional velocity
u^{EXP}	x-directional velocity component from experiments
u^{NUM}	x-directional velocity component from numerical models
v	y-directional velocity
V^M	water level/velocity magnitude from the modelled time series
V^R	water level/velocity magnitude from the reference time series
V^{EXP}	Velocity magnitude from experimental measurements
v^{EXP}	y-directional velocity component from experiments
V^{NUM}	Velocity magnitude from numerical models
v^{NUM}	y-directional velocity component from numerical models
v_h	Test function

x_c	x-coordinate of the grid centre
y_c	y-coordinate of the grid centre
z	Bed topography level
z^0	Mean coefficient of bed topography
z^{1x}	x-slope coefficient of bed topography
z^{1y}	y-slope coefficient of bed topography
z_h	DG2 approximation of the bed topography

Publications

Most of the contents in this thesis have been published in:

- Ayog, J. L., Kesserwani, G. 2018. *"Reformulation of 2D DG2 Scheme for Shallow Water Modelling"*, Proceedings of the HIC 2018: 13th International Conference on Hydroinformatics, Palermo, Italy. EPiC Series in Engineering, https://doi.org/10.29007/xlvx.
- Kesserwani, G., Ayog, J. L., Bau, D. 2018. *Discontinuous Galerkin formulation for 2D hydrodynamic modelling: Trade-offs between theoretical complexity and practical convenience*, Comput. Method Appl. Mech. Engrg. 342 (2018) 710-741. https://doi.org/10.1016/j.cma.2018.08.003.
- Ayog, J. L., Kesserwani, G., Shaw, J., Sharifian, M. K., Bau, D. 2021. *Second-order discontinuous Galerkin flood model: Comparison with industry-standard finite volume models*, J. Hydrol. 593 125924. https://doi.org/10.1016/j.jhydrol.2020.125924.
- Ayog, J. L., Kesserwani, G, Bau, D. 2021. *Well-resolved velocity fields using discontinuous Galerkin shallow water solutions*, J. Hydraul. Eng. *in review*. The preprint is available in http://arxiv.org/abs/2104.11308.

Chapter 1

Introduction

Some contents used to prepare for this chapter have been published in the following publications:

1. *Ayog, J. L., Kesserwani, G., Shaw, J., Sharifian, M. K., Bau, D. 2021. Second-order discontinuous Galerkin flood model: Comparison with industry-standard finite volume models, J. Hydrol. 593 125924. https://doi.org/10.1016/j.jhydrol.2020.125924*
2. *Ayog, J. L., Kesserwani, G, Bau, D. 2021. Well-resolved velocity fields using discontinuous Galerkin shallow water solutions, J. Hydraul. Eng. in review. The preprint is available in http://arxiv.org/abs/2104.11308.*

1.1 Background of the research

1.1.1 Industry-standard finite volume flood models

Floods account for 43% of the natural disasters occurring worldwide, and have resulted in 242,000 global fatalities and US$ 662 billion in financial losses over the past two decades (CRED 2015). To lessen the impacts of floods, stakeholders have increasingly relied on predictions from computational hydraulic models to develop flood risk reduction and management strategies (Afifi et al. 2019, Löwe et al. 2017, Şen & Kahya 2017). Most of these models are built around numerical solvers of the full two-dimensional shallow water equations

(2D-SWE) (Teng et al. 2017). Within this scope, the finite volume (FV) method is the most widely adopted 2D-SWE solvers and has been enhanced, particularly in the past years, in the current industrial flood modelling packages (Alcrudo 2004, Neelz & Pender 2009, Teng et al. 2017). They are also often preferred by government agencies in the UK, Netherlands and Australia for flood risk assessment and for the management of urban and rural floodplains (Engineers Australia 2012, Henckens & Engel 2017, Neelz & Pender 2013). FV-based flood models are known for their ability to capture the widest range of flow transitions, making them well-suited to provide reliable predictions for complex, real-world flood applications. For example, FV models are applied to produce hydrographs with detailed velocity transients to estimate structural damages on residential buildings (Pistrika & Jonkman 2010), to identify safe parking locations for emergency vehicles during flood evacuation (Arrighi et al. 2019), and to develop quantifiable hazard classification for flood vulnerability assessment (Costabile et al. 2020, Shirvani et al. 2020, 2021). Similarly, for gradually propagating floods, hydrographs produced by the FV-based models are used to estimate arrival times and flood levels in low-lying areas (Alkema 2007, Latrubesse et al. 2020), e.g. to assess the clearance time for flood evacuation (Cheng et al. 2011) and to identify zones for flood rescue prioritisation (Patel et al. 2017).

One issue with industry-standard FV models is that they often employ a first-order accurate finite volume (FV1) solver, as in the case, for example, of TUFLOW-FV1 (BMT-WBM 2016), Infoworks ICM (Lhomme et al. 2010), JFlow+ (Crossley et al. 2010), LISFLOOD-FP with Roe solver (Neal et al. 2012), RiverFlow2D (Hydronia LLC 2019), and BASEMENT (Vetsch et al. 2018). Such models may not be ideal for certain applications, as the outputs of an FV1 solver can be severely affected by rapid accumulation of numerical diffusion, particularly when the fine grid resolution needed to alleviate these errors is unaffordable (Lhomme et al. 2010, Neal et al. 2012). For example, an FV1-based flood model tends to predict late arrival times and narrower wetting extents (Schubert et al. 2008, Kesserwani & Sharifian 2020), and fails to capture small-scale transients in hydrograph predictions (Soares-Frazão & Zech 2008, de Almeida et al. 2018). Error analyses in the published literature show that

FV1-based models tend to produce larger deviations in hydrograph predictions when gauging stations are located far from the inflow and the flood duration lasts several days (Echeverribar et al. 2019, Horváth et al. 2020, Xia et al. 2019).

To improve the capability of FV-based models, second-order accurate finite volume (FV2) solvers have been used in existing industrial flood models, for example in TUFLOW-FV2 (BMT-WBM 2016), TUFLOW-HPC (BMT-WBM 2018), ANUGA (Mungkasi & Roberts 2013), and Iber (Bladé et al. 2014). Many FV2-based models adopt the Monotonic Upstream-centred Scheme for Conservation Laws (MUSCL) approach to reconstruct piecewise-linear solutions, but this widens the calculation stencil to the neighbour's neighbour of the element where local flow data are updated. The MUSCL approach comes hand-in-hand with a Total Variation Diminishing (TVD) slope limiter to ensure that the reconstructed flow solutions are free from unphysical oscillations. As the slope limiter is inherent to any MUSCL-FV2 solver and is applied globally over each grid element, choosing a slope limiter function that can simultaneously retain second-order accurate, oscillatory-free solutions, and ensure reliable reproduction of real-world features (Delis et al. 2011, Delis & Nikolos 2013, Hou et al. 2015, Zhao et al. 2018, Bai et al. 2018) and wave arrival times if the resolution is insufficiently fine (Kesserwani & Wang 2014, Zhao et al. 2018) can be challenging.

When modelling velocity fields around regions of wave-structure interactions, such as around houses and building blocks in an urban residential areas and cities during flash flooding, MUSCL-FV2 solvers have been reported to require the addition of an eddy viscosity term as the resolution becomes finer and when there is drastic change in the velocity magnitude and direction (Collecutt & Syme 2017, Syme 2008). Adding the eddy viscosity term can reduce the MUSCL-FV2 solver tendency to over-expand the extent of the recirculation flows and, thereby, improves the modelling of spatial velocity profiles (Bazin 2013). However, the eddy viscosity approach require case-dependent and often quite onerous calibration efforts. Additionally, the fast growth rate of numerical diffusion in MUSCL-FV2 solvers has been observed to smear the presence of small-scale eddies in the recirculation zones (Cea et al. 2007, Özgen-Xian et al. 2021), leading to significant discrepancies in the velocity field predictions around hydraulic structures such as bridge piers (Horritt et al. 2006).

1.1.2 Second-order Discontinuous Galerkin solver

The second-order discontinuous Galerkin (DG2) solver provides an alternative approach to the MUSCL-FV2 solver by generating and updating a piecewise-planar solution per grid element, where the solution slopes are defined intrinsically, thereby avoiding slope reconstruction and reducing the calculation stencil to the direct neighbours. With a DG2 solver, slope limiting becomes irrelevant and can drastically spoil the quality the predictions if applied globally as with MUSCL-FV2. Rather, the slope limiter should only be applied locally to stabilise the DG2 solution at very steep discontinuities within the wet portions of the computational domain (Kesserwani & Liang 2012*b*, Krivodonova et al. 2004). Hence, the choice for the limiter function is not pertinent with a DG2 solver, for which the key challenge has rather been to identify and apply a method to localise the operation of the slope limiter, which increases the computational cost of a DG2 solver (Fu & Shu 2017, Le et al. 2020, Marras et al. 2018, Qiu & Shu 2005, Vater et al. 2019).

Compared to the MUSCL-FV2 solver, the DG2 solver is more resistant to numerical diffusion, as demonstrated in the comparative study by Kesserwani & Wang (2014). This property enables the DG2 solver of the 2D-SWE to capture small-scale eddies in velocity fields for coastal and estuary modelling applications without the need of an eddy viscosity term, as hinted in a few published papers. Kubatko et al. (2006) studied the performance of DG2 and higher-order DG solvers in reproducing 2D velocity fields for a tidal flow over an idealised channel. The investigators concluded that the DG2 solver can deliver well-captured eddies outside of the channel inlet, leading to velocity fields that are as accurate as those produced by higher-order DG solvers. Alvarez-Vázquez et al. (2008) applied a DG2 solver for the simulation of fish migration to support the design of vertical slots along a fishway structure, with results showing a great potential for the DG2 solver to reproduce small-scale eddies within its 2D velocity field predictions. Beisiegel et al. (2020) explored a DG2 solver to simulate flow circulation, reporting that their DG2 solver was able to replicate the asymmetrical patterns of the recirculation eddies extracted from a 3D model. Despite this, very few 2D hydraulic modelling packages have adopted DG-based solvers, of which DG-SWEM (Bunya et al. 2009, Kubatko et al. 2006), SLIM (Lambrechts et al. 2010) and Thetis (Kärnä et al. 2018) are among the examples. Existing DG-based solvers have been primarily aimed to support modelling applications in lake, estuary and coastal systems (Le Bars et al. 2016, Clare et al. 2020, Le et al. 2020, Mulamba et al. 2019, Pham Van et al. 2016, Wood et al. 2020). However, the application of DG2 solvers for 2D flood inundation modelling has been little explored (Kesserwani & Sharifian 2020, Engineers Australia 2012) due to its expensive runtime cost contributed by excessive mathematical complexity (Kesserwani & Wang 2014). Although DG2 can naturally preserve well-balanced properties (which means that the model is able to simulate motionless water surface over an uneven topography for a long time period), complications relating to the numerical integration of steep topographic slopes do arise, and this has not yet been fully resolved (Caviedes-Voullième & Kesserwani 2015, Caleffi et al. 2016).

1.2 Research aim and objectives

Based on the research gaps identified in Sec. 1.1, this PhD research main aim to present a newly-developed hydraulic model based on a 2D-SWE DG2 solver that is made less complex, yet robust and competitive as industry-standard FV-based solvers for practical flood modelling applications. This DG2 solver applies square grids considering the reported benefits in terms of the accuracy and the computational efficiency compared to its triangular mesh counterpart (Wirasaet et al. 2010, 2014). With this purpose in mind, the following research objectives have been formed to support the achievement of the main aim of this research, namely:

1. To develop a 2D-SWE model based on a simplified grid-based DG2 formulation, and analyse its robustness and conservation properties against a standard DG2 formulation over varying flow types and topography shapes.

2. To assess the performance of the simplified DG2 flood model relative to commonly used FV-based models, including FV1- and FV2-based industry-standard modelling packages.
3. To identify suitable settings within the simplified DG2 model for flood modelling applications involving gradually and rapidly propagating floods, and with detailed velocity fields predictions around building structures.

1.3 The structure of the thesis

Immediately after this current chapter, the research approach and findings obtained from this PhD research are discussed and organised in this thesis following the structure presented below:

Chapter 2 contains the reviews of previous literatures describing the 2D-SWE and classical numerical methods solving the 2D-SWE used in practical flood modelling software packages. This chapter also overviews existing research involving the DG2 method and highlights research gaps pertaining to 2D-SWE modelling, including some discussion on past studies that have compared the performance of the DG2 relative to FV2 within the similar scope. The evolution of benchmark tests that have been used to analyse the capabilities of the industry-standard 2D flood models are also discussed, ranging from catchment- and regional-scale applications to smaller urban flood modelling practices.

Chapter 3, dedicated to address **Objective 1**, is centred around the simplified DG2 formulation, whilst highlighting its difference relative to the standard DG2 formulation. Both the simplified and standard DG2 formulation are compared over test cases that assess their 2D characteristics and ability to capture shock and rarefaction waves. Further exploration is made on the simplified DG2 formulation with respect to its conservation properties over varying topography and with dynamic movement of wetting and drying relevant to practical 2D-SWE modelling.

Chapter 4 extends the exploration performed in **Chapter 3** through the development of a flood model based on the simplified 2D-SWE DG2 solver. The key similarities and differences between simplified 2D-SWE solver and the FV-based solvers are identified. This chapter also aims to address **Objective 2**, whereby the capabilities of the simplified DG2 flood model are evaluated against established industry-standard FV1- and FV2-based modelling packages. The comparative assessments are done using well-known 2D hydraulic model benchmark tests with gradual and rapid flood propagation. Analysing the performance of the 2D-SWE DG2 solver also entails finding the suitable setting for the 2D-SWE DG2 solver for common flood modelling applications, thus addressing in part **Objective 3**.

Based on the findings observed in **Chapter 4**, **Chapter 5** investigates further the capabilities of the simplified DG2 solver involving less common modelling applications requiring detailed velocity field predictions. This chapter also intends to address the remaining part of **Objective 3** by identifying potential applications of an alternate setting than the one proposed for the simplified DG2 solver in **Chapter 4**. Selected test cases with extensive coverage of building structures, modelled at sub-metre grid resolutions, are used to assess the simplified DG2 capabilities relative to FV2 solver, particularly in predicting spatial velocity fields with small-scale recirculation eddies at regions of wave-structure interactions.

Chapter 6 presents the conclusion of the thesis, including the highlights of the research objectives achievement along with significance of the major findings. This chapter ends with several suggestions for future works.

Chapter 2

Literature Review

Hydraulic models are often applied to comprehend, analyse and forecast flooding and the transport of debris and water contaminants in order for key stakeholders and decision makers to take steps that can safeguard vulnerable population. These hydraulic models have been widely applied for flood risk mapping (e.g. Webster et al. (2014), Mudashiru et al. (2021)), flood damage assessment (e.g. Jonkman et al. (2008)), real-time flood forecasting (e.g. Barthélémy et al. (2017)), design of flood defence structures (e.g. Siviglia et al. (2009)), validation of insurance claims (Zischg et al. 2018) and management of water resources (e.g. Leskens et al. (2014)). Additionally, these models have been made as an important part of the assessments of sediment erosion and transport (e.g. Mouri et al. (2013)), pollutant transport (e.g. Drago et al. (2001)), floodplain ecology (e.g. Karim et al. (2015)), river system hydrology (e.g. Inthasaro & Wu (2012)) and catchment hydrology (e.g. (Yu & Coulthard 2015)). They have also frequently been coupled with climate, hydrological and sewerage models, and further extended to analysing risk related to climate change (e.g. Morita (2011), Banks et al. (2014)) and subsurface flows (e.g. Sommer et al. (2009)). Progressive improvement in modern hydraulic models have produced reliable and robust simulations, making them feasible to effectively manage environmental flows for healthy aquatic environment (e.g. Salmon et al. (2017)).

Computational-based hydraulic models, which typically solve mathematical equations derived from the laws of physics, are often the preferred choice to represent the movement of water in areas that are flood-prone (i.e. towns and cities located in a floodplain). Amongst these models, the three-dimensional models based on Navier-Stokes equations (3D-NS) can provide the closest physical representation of the water dynamics. However, they tend to be very complex mathematically thus entail very high computational costs (Toombes & Chanson (2011), Mintgen & Manhart (2018)) and are impractical for river reach-scale of more than 1 km, along with other issues associated with the representation of the water levels, high-order turbulence and the movement of shorelines (Teng et al. (2017)). In contrast with the 3D-NS models, the two-dimensional models solving shallow water equations (2D-SWE), despite having reduced numerical complexity, are more commonly used for flood modelling particularly in areas with poorly defined flow path (Toombes & Chanson (2011)) and also in riverine systems with frequent flow exchange between the main channel and the floodplain. This is because the 2D-SWE models can provide very good representation of floodplain conveyance and are well suited to simulate the extent of inundation that constantly change over time. These features have made the 2D-SWE models the favourite selection for modelling flood flows in urban and coastal settings, and also in riverine systems recurrent with overbank flows.

2.1 Two-dimensional shallow water equations (2D-SWE)

The 2D hydraulic models are generally developed around the 2D-SWE, which is achieved by averaging the 3D-NS equations over the flow depth (Teng et al. 2017, Alcrudo 2004). This simplification thus eradicates the complications encountered with the 3D-NS equations in calculating the position of the free water surface (Alcrudo 2004). The 2D-SWE can be expressed in Eqs. 2.1, assuming a uniform and constant flow density (Cozzolino et al. 2021):

$$\frac{\partial h}{\partial t} + \frac{\partial q_x}{\partial x} + \frac{\partial q_y}{\partial y} = 0 \tag{2.1a}$$

$$\frac{\partial q_x}{\partial t} + \frac{\partial}{\partial x}\left(\frac{gh^2}{2} + \frac{q_x^2}{h}\right) + \frac{\partial}{\partial y}\frac{q_x q_y}{h} = -gh\frac{\partial z}{\partial x} - ghS_{f_x} \tag{2.1b}$$

$$\frac{\partial q_y}{\partial t} + \frac{\partial}{\partial x}\frac{q_x q_y}{h} + \frac{\partial}{\partial y}\left(\frac{gh^2}{2} + \frac{q_y^2}{h}\right) = -gh\frac{\partial z}{\partial y} - ghS_{f_y} \tag{2.1c}$$

where x and y indicate the coordinates of a given location, t is the time, h is the water depth, $q_x = hu$ and $q_y = hv$ are the unit-width discharge components along x and y directions, with u and v the directional components of the depth-averaged velocity, z is the bed topography, S_{f_x} and S_{f_y} are the friction terms, with $S_{f_x} = -n_M^2 u(u^2 + v^2)^{1/2}/h^{4/3}$ and $S_{f_y} = -n_M^2 v(u^2 + v^2)^{1/2}/h^{4/3}$ (where n_M is the Manning's resistance coefficient), and g is the gravity acceleration. Eq. 2.1a represents the mass equation, whilst Eqs. 2.1b and 2.1c are the x- and y-directional momentum equations respectively.

Other influences such as the viscosity effects, Coriolis terms, wind shear stress terms and wall friction terms can be included in the 2D SWE as well. In flood modelling however, the Coriolis terms that accounts the effects of the Earth's rotation are normally neglected. The wind shear stress terms are normally considered if the wind strength and direction can significantly influence flood predictions in very large flat plains, whilst wall friction is generally relevant in applications involving very high resolution modelling.

Although flood models based on the 2D-SWE are the most popular, they are not representative of the true water movements on the Earth's surface. Besides the discrepancies instigated from the averaging procedure for the 2D SWE, the following lists the known limitations of this approximation (Alcrudo 2004):

- Velocities in the vertical directions are ignored (resulting in zero vertical accelerations),
- A hydrostatic pressure distribution is assumed in the flow system,
- The topography gradient is assumed small,
- The horizontal velocity is assumed to be uniform,
- The effects due to turbulence are ignored,

- The friction value is determined from uniform flow conditions.

Regardless of the limitations described above, majority of the modern industry-standard flood models are built upon solving the 2D-SWE, indicating that using these models in representing the physical processes of flooding are still relevant (Duan 2005, Neelz & Pender 2009, Aureli et al. 2015). The 2D-SWE can be solved using a variety of numerical methods, but these mostly fall into one of the three classical methods described in the next section.

2.2 Classic numerical methods in 2D-SWE flood models

Many of the numerical methods applied to discretise the spatial domain can be classified into one of the following major groups: the finite difference (FD), finite element (FE) and the finite volume (FV) methods (Teng et al. 2017, Alcrudo 2004, Neelz & Pender 2009, Hinkelmann et al. 2015) regardless whether the computational grids used is either of structured (square or quadrilateral), unstructured (triangular) or more recently, flexible, mixed-type mesh.

Among these groups, the finite difference (FD) method is the most straightforward to be implemented and much more established for practical applications. This method approximate unknown variables for the derivative involved in the 2D-SWE in sets of grid points. Despite the rather simple approach, the popularity of these methods is in decline among the academic communities due to their rigidity in geometrical sense especially around curving river channels and floodplains (Alcrudo 2004, Neelz & Pender 2009). Furthermore, FD flood models are generally based on the ADI (Alternating Direction Implicit) approach, which can very reliable when modelling flood flows on mild slope, but tend to generate spurious numerical oscillation around sharp gradients in the solution particularly in flash flooding and on short hilly catchments (Liang et al. 2007, Kvočka et al. 2015). On the other hand, modelling software packages built on the FD method are still popular among industrial communities and academic researchers dealing with real-world flooding applications e.g. DIVAST-2D (Musolino et al. 2020, Kvočka et al. 2016, 2017) and MIKE FLOOD (Beden & Ulke Keskin 2021, Shrestha et al. 2020, Löwe et al. 2017) mainly because they are more compatible with raster-based digital terrain and bathymetry models, although such software packages may need to adopt shock-capturing algorithms such as the TVD approach, that can be more than 8 times longer to run compared to the ADI approach (Kvočka et al. 2015).

The finite element (FE) method works by solving the weak formulations of the conservation laws using selected test functions (usually via the Galerkin method) for a solution space that is discretised into a finite number of elements. Unlike the FD method, the FE method conserves mass over the whole spatial domain (but not within each grid element) (Bradford & Sanders 2002), although the underlying mathematical foundation is more rigorous, which perhaps the reason why this method are not widely used in commercial software packages. The FE-based software packages may produce large computational time, as a result of its high mathematical complexity, and can complicate mesh generation if no proper mesh generating tool is available (Alcrudo 2004, Neelz & Pender 2009). Despite the shortcomings, the mathematical theory behind the FE method is well-developed, hence they could accommodate more flexibility (as unstructured grids are usually applied) and achieve higher accuracy, especially in domains with complex boundaries and boundary conditions. A well-established FE-based flood modelling software developed by Électricité de France (EDF) called TELEMAC-2D has successfully been applied to simulate real cases of flood inundation (Bates et al. 1999, Horritt & Bates 2001, Horritt et al. 2006, Alho & Aaltonen 2008, Vu et al. 2015, Pavlíček & Bruland 2019) although later versions of this model are blended with the finite volume methods (Ata 2012).

In the recent decades, the finite volume (FV) method has become the most adopted spatial discretisation approach in modern flood models. This methods discretises the solution space into certain number of non-overlapping finite volumes, in which the integral form of the hyperbolic 2D-SWE is applied. Also known as the conservative Godunov-type formulations (Godunov 1959, Toro 2001, Toro & Garcia-Navarro 2007, García-Navarro et al. 2019), the FV method is inherently local and first-order accurate in the sense that the flux balance evolves a mean coefficient, which is a piecewise-constant approximation of the state variables. Based on their advantages in terms of intrinsic shock-capturing ability, great geometrical flexibility (i.e. can be applied to structured, unstructured and flexible meshes), conservation properties and simplicity in the underlying mathematical concept, the FV-based method is preferred to FD or FE methods to be applied in many known industry-standard flood modelling packages, both for commercial and academic purposes (Neelz & Pender 2009, 2013, Teng et al. 2017). These FV-based packages have been proven to be stable and robust in modelling real-world flooding problems. However, first order FV method tends to be strongly affected by numerical diffusion, thus causing undesired effects in the predictions such as smearing of the solution along with smooth, rounded edges of wave fronts in flows containing discontinuities (e.g. dam-break cases) that can deliver inaccurate numerical results (Neal et al. 2012, Hou et al. 2015).

To increase the accuracy of the FV-based models, second-order formulations have been developed by reconstructing piecewise-linear approximations from the initial piecewise-constant data beyond immediate neighbouring cells, but in doing so the locality of the computational stencil will be sacrificed (Van Leer 1979, Yamamoto et al. 1998, Caleffi et al. 2006, Xing 2016). FV2-based flood models have relatively wider calculation stencil, which has been observed to adversely affect practical applications, such as wetting and drying (Begnudelli & Sanders 2006, 2007, Bradford & Sanders 2002, Kesserwani & Wang 2014, Morales-Hernández et al. 2021), and conservation properties needed to deal, for example, with slope limiters (Hou et al. 2014, Kesserwani & Wang 2014, Nikolos & Delis 2009, Sanders & Bradford 2006) that can potentially reduce the accuracy of the FV2 model to first order. Challenges pertaining to slope limiters in the FV2 models are further discussed in Sec. 4.2.2. To address these challenges, investigation on other types of the Godunov-type numerical methods is significantly progressing in recent years particularly for the application in flood risk assessment and management. One of the said methods is the Discontinuous Galerkin (DG) method in Section 2.2.1.

2.2.1 Discontinuous Galerkin (DG) method

In light of the Godunov-type philosophy, the DG method is naturally an extension to the finite volume method, by combining the locally-conservative finite volume principles and the flexibility of the finite element weak formulation to form a solution over a computational element. This is achieved by evolving a polynomial solution while restricting to use the initial data that is locally contained within an element alongside its immediate adjacent neighbours for numerical flux calculation. But compared to the traditional FE (based on the continuous Galerkin) and the FV methods, the DG method needs to store and evolve more than a mean coefficient to define the local polynomial solution. The number of coefficients needed to be stored and evolved depends on the order of accuracy, spatial dimensionality and spatial resolution (Caviedes-Voullième & Kesserwani 2015). In this respect, the mathematical complexity that forms the basis of the DG formulations increases in proportion to these influences; increasing the expected order of accuracy will affect the computational efficiency and numerical stability, which pose a challenge when integrating salient features crucial for practical applications. Therefore, a second-order DG method (DG2) is often a selected option as a trade-off (Kesserwani & Liang 2011, Kesserwani & Wang 2014).

In formulating a robust DG2 method for 2D-SWE modelling, there are less developments involving square grids and quadrilateral mesh types (Kesserwani & Liang 2010, 2012*a*, 2015), compared to their triangular counterparts, despite reported benefits in terms of accuracy and computational efficiency (Wirasaet et al. 2010, 2014). Previous studies exploring square grids and quadrilateral meshes (Gerhard et al. 2015, Kesserwani & Wang 2014, Kesserwani & Liang 2012*a*) only focused on the mean coefficients in the DG2 solutions when studying well-balanced properties, which generally involved smooth-shaped topography. Thus, further investigation is still deemed necessary to investigate the full extent of the well-balancedness properties beyond the mean (average) coefficients along with considering the steep-sloped topography shapes. Furthermore, most investigations (Gerhard et al. 2015, Kesserwani & Wang 2014, Kesserwani & Liang 2012*a*) adopted the pre-balanced form of the SWE (Lu & Xie 2016), in which the main variable is represented by the water level, instead of the water depth. In contrast to the conventional form of the SWE, the pre-balanced form is likely unneeded and can entail additional computational runtimes (Lu & Xie 2016).

In recent decades, the development of the DG method is progressively maturing in the context of practical 2D-SWE modelling. Increased interests on this method is also noted in the field of water resources in tandem with the advancement of finite volume modelling (Bokhove 2005, Ern et al. 2008, Gourgue et al. 2009, Kesserwani & Liang 2011). This method is also highly compatible for parallel computing technologies, both in the conventional central-processing unit (CPU) platforms (Biswas & Devine 1994, Eskilsson et al. 2009, Brus et al. 2017, Dawson et al. 2013, Samii et al. 2016, Shaw et al. 2021) and also in graphics-processing units (GPUs) (Fuhry et al. 2014, Klöckner et al. 2009, DuChene et al. 2011, Chan et al. 2016, Shaw et al. 2021), as the DG method remains local (i.e. data transfer and storage are restricted only between local grid and its immediate neighbours) when higher-order accuracy is required. It also forms the basis for local mesh, polynomial order and time step adaptivity (Dawson et al. 2013, Samii et al. 2016, Chan et al. 2016, Conroy & Kubatko 2016). Despite these merits, the DG method is not widely used for flood inundation modelling and hydraulic engineering applications, partly due to the expensive runtime costs (Kesserwani & Wang 2014)) as well as issues pertaining to well-balancedness and stability (Caviedes-Voullième & Kesserwani 2015, Caleffi et al. 2016). Hence, the reduction in the complexity level of DG formulations is necessary in favour of affordable computational costs and robustness for modelling realistic flooding scenarios. In addition, an accurate topography discretisation should be established so that the precise equilibrium between the flux and the topography source terms can be achieved, ensuring the conservativeness (i.e. preservation of well-balanced property) of the DG2 method.

2.2.2 Comparative studies between FV2 and DG2 methods

Previous studies assessing the performance of the DG2 method relative to the FV2 method using academic and experimental test cases have demonstrated the potential benefits of the DG2 method for practical 2D-SWE modelling. Wang & Liu (2005) compared DG2 against

FV2 in producing a smooth, symmetrical flow curvature in a uniformly rotating flow field. They found that after one rotation, the FV2 predicted a much flatter and assymetrical curving of the flow with significant underestimation of the peak depth and the extent of recirculating eddies. In contrast, the DG2 method produced solutions that are less diffusive and preserves the shape of the flow curvatures and the recirculation flows. Duran & Marche (2014) assessed the capability of DG2 against FV2 based on the profiles of the water depth extracted from the 2D outputs of water drop in the middle of a square pool. The resulting DG2 profiles showed better capturing of the wave crest propagating away from the pool centre and followed very well a small curving around the wave trough in the analytical solution. In a laboratory experiment analysing flood propagating along a crossroad, Ghostine et al. (2009) analysed the water surface profiles replicated by the DG2 and FV2 from the experimental data and compared to a 3D model. They found that DG2 is able to replicate the profiles of the experimental data and the 3D model much closer than FV2 particularly around the regions of recirculation flows, thus affirming the findings made by Wang & Liu (2005).

A more comprehensive assessment on the capabilities of DG2 and FV2 for flood inundation modelling has been done by Kesserwani & Wang (2014). The assessment covered test cases involving realistic flooding scenarios caused by a dam-break and fluvial flooding over real-world terrain conditions. Their findings showed that the FV2 predictions tends to degrade as the meshes coarsened, with more diffusive predictions around the regions of high flow curvature (corroborating with the results of Wang & Liu (2005) and Duran & Marche (2014)) and mispredictions of the vanishing velocity at the wet-dry interfaces. On the other hand, DG2 is capable to provide results with increased prediction quality on very coarse grids and with detailed capturing of the velocity transients, albeit with at least 10 times more expensive in runtimes compared to the FV2. The capability of DG2 to produce reliable results on coarse resolutions is also supported by the findings of Ghostine et al. (2019) who simulated flooding over urbanised environments. They found that the water depth predicted by DG2 around regions of wave-structure interactions are closer to reference data than FV2 on coarse meshes. Despite these studies highlighted the advantages of using DG2 for real-world flood modelling, which are also noted by some industrial community (Engineers Australia 2012), there is still the need to affirm the utility of the DG2 method for industry-standard modelling applications.

2.3 Benchmarking of industry-standard 2D flood models

Initially, flood model benchmarking exercises focus on tracking development of new numerical methods and techniques based on the input data and computing resources available at that time. These exercises however, were more focused on using the model equations that solve hyperbolic conservation laws, with less emphasis on real-life applications. Early benchmarking exercises within this scope were done in the 1990s and reviewed by Leopardi et al. (2002). With the introduction to sophisticated data gathering techniques, such as high resolution satellite imagery and Light Detection and Ranging (LiDAR) scanner, the collation of hydraulic data to build digital elevation models (DEM) and to estimate flow friction have tremendously improved, making 2D flood modelling much more appealing (Cobby et al. 2001, Pender 2006, Sanders & Bradford 2006). As these techniques progress, studying the effects of applying 2D flood models for flood risk studies has become necessary in cases where complex floodplain flow processes are much more dominant.

Considering that many decision-making activities are dependent on the results obtained from the 2D flood models, several countries have written modelling guidelines to ensure flood models are able to perform tasks relevant to flooding assessments in riverine and urban areas (Engineers Australia 2012, Scottish Environment Protection Agency 2016, Henckens & Engel 2017). Hence, the benchmarking tasks lately focus on identifying models suitable for given flood risk mapping and management studies. These models are identified based on their current capabilities that meet the minimum modeling requirement of each industry-relevant application. In the United Kingdom, such benchmarking efforts were initially done using real-world hydrometric data and images of flood extent from aerial photographs and airborne radars that were obtained from several, specifically chosen flooding events. Horritt & Bates (2001) tested an FE-based 2D-SWE flood model, TELEMAC-2D, against inundation map and hydrometric data for River Thames which were then compared to those from a raster-based flood model, LISFLOOD-FP. They later conducted similar study on TELEMAC-2D for River Severn (Horritt & Bates 2002). In a more rigorous comparative study on industry-standard 2D hydraulic models, Hunter et al. (2008) tested six models (three 2D-SWE FD-based models (TUFLOW, DIVAST-ADI and DIVAST-TVD), one 2D-SWE FV-based model (TRENT) and two simplified 2D models (JFLOW and LISFLOOD-FP)) in simulating a flood event in the city of Glasgow, Scotland. They found that in areas where there are less friction and shallower water depths, 2D-SWE flood models without shock-capturing capability yields more numerical oscillations in the water depth predictions. The full 2D-SWE models were also computationally cheaper than the simplified models when modelling on very fine mesh resolution (i.e. 2 m), but significant optimisation works on the simplified models, along with the addition of parallel computing technologies, have made both models to be equally competitive in recent years (Neal et al. 2018, Shaw et al. 2021).

Since 2009, 2D flood model benchmarking has been shifted from using specific flood events to assess the overall performance of the model, to using only simple academic test cases that can reliably validate the numerical robustness required for a given practical engineering application. Lhomme et al. (2010) evaluated an FV-based model IW2D (also known as Infoworks 2D) against another FV model, TELEMAC-FV and one FD-based model (TUFLOW), all of which are commonly-used in consultancy works, over five academic test cases with available analytical solutions. They reported that whilst IW2D and TELEMAC-FV performed equally well when modelling dam break and rapid transients over dry surfaces, both fall short in tidal environments with cyclic wetting and drying, with TELEMAC-FV generated significant dampening of wave amplitude compared to IW2D. Realising that better understanding is needed for a range of 2D hydraulic modelling packages used for flood-related projects, the UK Environment Agency (UK EA) has proposed and recommended eight benchmark tests to assess frequently used 2D flood models and mapped the tests to specific flood-related applications (Neelz & Pender 2009, 2010, 2013). A summary of the benchmark tests is shown in Table 2.1, with the mapping of the tests to each modelling application of the UK EA provided in Table 2.2. The capabilities of eight 2D-SWE flood models using FD- and FV-

Table 2.1: *The summary of UK EA benchmark tests (Neelz & Pender 2010, 2013).*

EA Test No.	Description	Model dimensionality
1	Flooding a disconnected water body.	2D model only
2	Filling of floodplain depressions.	
3	Momentum conservation over a small (0.25m) obstruction.	
4	Speed of flood propagation over an extended floodplain.	
5	Valley flooding.	
6A & 6B	Dam break.	
7	River to floodplain linking.	2D model with 1D river network
8A & 8B	Rainfall and sewer surcharge flood in urban areas.	2D model with 2D rainfall or 1D sewer model

based solvers were assessed in the first UK EA benchmarking exercise (Neelz & Pender 2010) followed by another round of benchmarking using additional or more updated version of 2D modelling packages (Neelz & Pender 2013). Since UK EA benchmarking tasks involved many well-known industry-standard flood models and with thorough analyses of the models' capabilities, the benchmark tests become popular that these have been implemented to newly-developed and enhanced 2D models that are not part of original UK EA benchmarking assessments, such as HEC-RAS 2D (Brunner 2016), 3Di (Schuurmans & Leeuwen 2014), Swift (Cohen et al. 2016), PCSWMM/SWMM5 (James et al. 2013) and MOHID (Pina et al. 2015). Also, the developers of TUFLOW (who participated in the UK EA benchmarking exercises) have reapplied the same tests to their latest software packages equipped with state-of-the-art modelling technology (i.e. parallelised and/or GPU computing) (Huxley et al. 2017). A list of flood models based on full 2D SWE that have been benchmarked using the UK EA tests is shown in Table 2.3.

2.3.1 Detailed velocity field predictions

Most of the flood modelling applications listed in Table 2.2 indicate that the spatial scope of applications relevant to the UK EA tests are of large catchment- or regional-scale. However, comprehensive assessments of the capabilities of industry-scale 2D flood models for smaller

Table 2.2: *Mapping of benchmark test cases to model for UK EA applications (Neelz & Pender 2010, 2013).*

Application	**Prediction required**	**Relevant benchmark tests**
Large-scale flood risk mapping (up to 1000 km^2)	flood extent	1 & 2
Catchment flood management plan	flood extent; maximum depth	1, 2 & 7
Flood risk assessment and detailed flood mapping	flood extent; maximum depth	1, 2, 3 and 7
Strategic flood risk assessment	flood extent; maximum depth and velocity	1, 2, 3, 4, 7 and 8
Flood hazard mapping	flood extent; maximum depth and velocity	1, 2, 3, 4, 7 and 8
Contingency planning for real time flood risk management	time-varied flood extent, depth and velocity	1, 2, 3, 4, 5, 7 and 8
Reservoir inundation mapping	time-varied flood extent, depth and velocity	1, 2, 3, 4, 5 and 6

Table 2.3: *List of flood modelling software packages based on full 2D-SWE that have been tested using the UK EA benchmark tests.*

Model name	Numerical method	Mesh type	Sources
ANUGA	FV	Flexible	Neelz & Pender (2010, 2013)
FloodFlow	FD	Square grid	Neelz & Pender (2010)
Infoworks 2D	FV	Flexible	
ISIS2D	FD	Square grid	Neelz & Pender (2010, 2013)
MIKE FLOOD	FD	Square grid	
SOBEK	FD	Square grid	
TUFLOW (ADI)	FD	Square grid	
TUFLOW (FV)	FV (1^{st} and 2^{nd} order)	Flexible	
Flowroute-i^{TM}	FV	Square grid	Neelz & Pender (2013)
Infowork ICM	FV	Flexible	
ISIS 2D GPU	FV	Square grid	
JFLOW +	FV	Square grid	
XPStorm	FD	Square grid	
LISFLOOD-Roe	FV	Square grid	Neal et al. (2012)
HEC-RAS 2D	FV	Flexible	Brunner (2016)
3Di	FV	Flexible	Schuurmans & Leeuwen (2014)
Swift	FV	Square grid	Cohen et al. (2016)
PCSWMM/ SWMM5	FV	Flexible	James et al. (2013)
MOHID	FV	Square grid	Pina et al. (2015)
TUFLOW-Classic	FD	Square grid	Huxley et al. (2017)
TUFLOW-HPC	FV (2^{nd} order)	Square grid	
TUFLOW-GPU	FV (1^{st} order)	Square grid	
TUFLOW FV (2014 Release)	FV (1^{st} and 2^{nd} order)	Flexible	
RiverFlow2D Plus	FV	Flexible	Jenkins & Garcia (2015)
RiverFlow2D Plus GPU	FV	Flexible	
Tygron Geodesign Platform	FV	Square grid	TYGRON (2019)

spatial scale, such as urban flooding along complex road networks around buildings in a city, is also important. For smaller spatial scope, it is necessary that the selected 2D flood model is able to provide reliable information on the spatial velocity fields in order to estimate the flood hazard over the whole inundation area, which often the goal of flood inundation modelling (Bates et al. 2014, Smith et al. 2012). This would mean that in urban areas with irregular flood extent and with many regions of wave-structure interfaces, the flood model can produce sufficiently realistic velocity fields with localised variability of the distribution pattern around the buildings (Hunter et al. 2007, Schubert & Sanders 2012, Dottori et al. 2013). Additionally, there is also a need for detailed spatial information of velocity within city streets to mobilise operational flood management during an urban flooding (Guo et al. 2021).

At present, there is no specific set of benchmark tests, such as the UK EA tests, that is available to assess the suitability of industry-standard 2D flood models for producing detailed spatial velocity fields for urban flood modelling. This is perhaps due to the difficulties in acquiring observation data to validate the models, particularly when the inundation coverage is extensive and direct *in-situ* measurements can pose safety concerns if conducted during flooding (Bates et al. 2014). Instead, the 2D flood models are assessed using velocity fields measured from physical models that were purposely designed to replicate real-world hydrodynamics around dense urban structures. For instance, the velocity fields produced by two FD-based flood models (TUFLOW and MIKE-FLOOD) were analysed against measured velocity data collated from a physical model representing an urban residential area with small piers (Smith et al. 2016). An industry-standard FV2-based model, Rubar20, is used to study spatial velocity fields predictions relative to the velocity measured using particle imagery velocimetry (PIV), around raised sidewalks and obstacles smaller than a common building structure within a right angle junction (Bazin et al. 2017, Bazin 2013). Although these assessments were made to analyse the reproduction of the velocity field around urban fixtures as seen from the physical models, deeper investigation is still required to identify the capabilities of the 2D flood models to predict spatial velocity for field-scale modelling applications.

Chapter 3

Grid-based DG2 formulation for 2D-SWE modelling

Contents used to prepare for this chapter have been published in the following publications:

1. *Ayog, J. L., Kesserwani, G. 2018. "Reformulation of 2D DG2 Scheme for Shallow Water Modelling", Proceedings of the HIC 2018: 13th International Conference on Hydroinformatics, Palermo, Italy. EPiC Series in Engineering, https://doi.org/10.29007/xlvx.*
2. *Kesserwani, G., Ayog, J. L., Bau, D. 2018. Discontinuous Galerkin formulation for 2D hydrodynamic modelling: Trade-offs between theoretical complexity and practical convenience, Comput. Method Appl. Mech. Engrg. 342 (2018) 710-741. https://doi.org/10.1016/j.cma.2018.08.003.*

3.1 Chapter overview

This chapter, which seeks to address Objective 1, elucidates the formulation of the simplified DG2 solver based on the conservative form of the 2D-SWE, along with the analyses of its well-balanced properties not only for the mean coefficients but also the slope coefficients. In Sec. 3.2, the standard DG2 formulation is firstly described, then followed by the simplified DG2 formulation. The simplified DG2 formulation, which has been developed to produce a slope-decoupled formulation, is made capable in preserving well-balanced properties fully (for all mean and slope coefficients) considering a range of realistic flow cases and topography shapes. Sec. 3.3. presents the test cases that are tailored to compare the performance of the simplified DG2 solver against the standard DG2 solver, and later to verify the simplified DG2 solver practical capabilities in terms of its accuracy and conservation properties. Finally, the key findings from these test cases are summarised in the concluding remarks in Sec. 3.4.

3.2 DG2 formulations on grid elements

By considering the hyperbolic conservation laws, which is expressed in its conservative form in Eq. 3.1, the DG2 numerical solutions are explored over a 2D domain Ω:

$$\partial_t \mathbf{U} + \partial_x \mathbf{F}(\mathbf{U}) + \partial_y \mathbf{G}(\mathbf{U}) = \mathbf{S}(\mathbf{U}) \tag{3.1}$$

where $\mathbf{U}(x, y, t)$ is the vector of the state variables at location (x, y) and time t, $\mathbf{F}(\mathbf{U})$ and $\mathbf{G}(\mathbf{U})$ are spatial flux vector corresponding to the x- and y-directions, and $\mathbf{S}(\mathbf{U})$ represents the source term vectors. In Eq. 3.1, ∂_t, ∂_x and ∂_y are the partial derivatives relative to t, x and y, respectively.

The 2D domain Ω is discretised into $M_Q \times N_Q$ uniform grid elements Q_c $(c = 1, ..., M_Q \times N_Q)$. Each element Q_c is centred at (x_c, y_c) with a size of $\Delta x = \Delta y$, and can be expressed as $Q_c = [x_c - \frac{\Delta x}{2}, x_c + \frac{\Delta x}{2}] \times [y_c - \frac{\Delta y}{2}, y_c + \frac{\Delta y}{2}]$ (see Fig. 3.1).

3.2.1 Standard DG2 formulation

An approximate solution of $\mathbf{U_h}$ of Eq. 3.1 is sought by multiplying both-hand sides of the equation by a test function $v_h(x, y)$, which is compactly supported on Q_c, and then integrating over Ω. These produce the following weak formulation:

$$\begin{aligned}&\iint_{Q_c} \partial_t \mathbf{U_h}(x,y,t) v_h(x,y)dxdy + \iint_{Q_c} \partial_x \mathbf{F(U_h)} v_h(x,y)dxdy + \iint_{Q_c} \partial_y \mathbf{G(U_h)} v_h(x,y)dxdy \\ &= \iint_{Q_c} \mathbf{S(U_h)} v_h(x,y)dxdy\end{aligned} \tag{3.2}$$

Integration by parts of the second and third terms at the left-hand side of Eq. 3.2 gives:

$$\begin{aligned}&\iint_{Q_c} \partial_x \mathbf{F(U_h)} v_h(x,y)dxdy \\ &= \left[\int_{y_c-\Delta y/2}^{y_c+\Delta y/2} \mathbf{F(U_h)} v_h(x,y)dy\right]_{x_c-\Delta x/2}^{x_c+\Delta x/2} - \iint_{Q_c} \mathbf{F(U_h)} \partial_x v_h(x,y)dxdy\end{aligned} \tag{3.3}$$

$$\begin{aligned}&\iint_{Q_c} \partial_y \mathbf{G(U_h)} v_h(x,y)dxdy \\ &= \left[\int_{x_c-\Delta x/2}^{x_c+\Delta x/2} \mathbf{G(U_h)} v_h(x,y)dx\right]_{y_c-\Delta y/2}^{y_c+\Delta y/2} - \iint_{Q_c} \mathbf{G(U_h)} \partial_y v_h(x,y)dxdy\end{aligned} \tag{3.4}$$

In Eqs. 3.3 and 3.4, the spatial derivatives are now removed from the flux terms. By inserting these two equations into Eq. 3.2, and moving the spatial components to the right-hand side of the equation, the weak formulation can be expressed as:

$$\iint_{Q_c} \partial_t \mathbf{U}_h(x,y,t) v_h(x,y)dxdy = \mathbf{L_h} \tag{3.5}$$

$$\mathbf{L_h} = -[(\mathbf{I_h} + \mathbf{J_h}) - (\mathbf{M_h} + \mathbf{N_h} + \mathbf{S_h})] \tag{3.6}$$

In Eq. 3.6, $\mathbf{L_h}$ is the spatial operator, in which $\mathbf{I_h}$ and $\mathbf{J_h}$ are local flux balance terms throughout the x- and y-direction, respectively:

$$\mathbf{I_h} = \left[\int_{y_c-\Delta y/2}^{y_c+\Delta y/2} \mathbf{F(U_h)} v_h(x,y)dy\right]_{x_c-\Delta x/2}^{x_c+\Delta x/2} \tag{3.7}$$

$$\mathbf{J_h} = \left[\int_{x_c-\Delta x/2}^{x_c+\Delta x/2} \mathbf{G(U_h)} v_h(x,y)dx\right]_{y_c-\Delta y/2}^{y_c+\Delta y/2} \tag{3.8}$$

and $\mathbf{M_h}$, $\mathbf{N_h}$ and $\mathbf{S_h}$ are local volume integral terms for the fluxes and source terms, given by:

$$\mathbf{M_h} = \iint_{Q_c} \mathbf{F(U_h)} \partial_x v_h(x,y)dxdy \tag{3.9}$$

$$\mathbf{N_h} = \iint_{Q_c} \mathbf{G(U_h)} \partial_y v_h(x,y)dxdy \tag{3.10}$$

$$\mathbf{S_h} = \iint_{Q_c} \mathbf{S(U_h)} v_h(x,y)dxdy \tag{3.11}$$

To construct a local planar DG2 solution on the grid elements, a suitable choice for the test function v_h is by using the 2D tensor product of the Legendre polynomial basis, over which the stencil of a grid element Q_c in Fig. 3.1 is applied. This then generates the following planar approximate solution, $\mathbf{U_h}$, expressed as:

$$\mathbf{U_h}(x,y,t)|_{Q_c} = \mathbf{U}_c^0(t) + \frac{(x-x_c)}{\Delta x/2}\mathbf{U}_c^{1x}(t) + \frac{y-y_c}{\Delta y/2}\mathbf{U}_c^{1y}(t) \tag{3.12}$$

The planar solution in Eq. 3.12 is defined by a set of coefficients, consisting of the mean coefficient, $\mathbf{U}_c^0$ and the slope coefficients in the x-direction, $\mathbf{U}_c^{1x}$ and y-direction, $\mathbf{U}_c^{1y}$. These coefficients needed to be initialised using the formulae below:

$$\mathbf{U}_c^0 = \frac{1}{4}\left[\mathbf{U}_0(\mathrm{G1}) + \mathbf{U}_0(\mathrm{G2}) + \mathbf{U}_0(\mathrm{G3}) + \mathbf{U}_0(\mathrm{G4}))\right] \tag{3.13a}$$

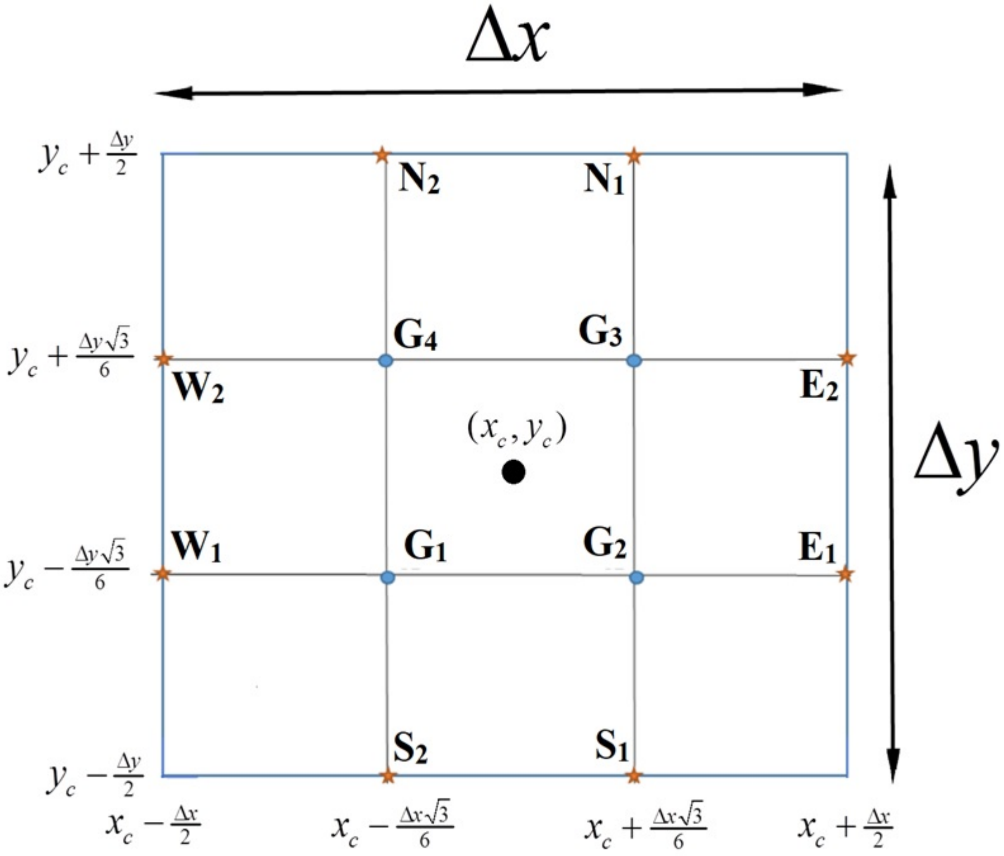

Figure 3.1: *The stencil of a grid element* Q_c *for the standard DG2 form.* G_i ($i = 1, 2, 3$ *and* 4) *are the local Gaussian points where the volume integral terms in Eqs. 3.9-3.11 are evaluated. Meanwhile,* E_i, W_i, N_i *and* $S_i (i = 1, 2)$ *are the Gaussian points at the eastern, western, northern and southern faces that aggregates Riemann fluxes contribution in Eqs. 3.7-3.8.*

.

$$\mathbf{U}_c^{1x} = \frac{\sqrt{3}}{4}\left[\mathbf{U}_0(\mathrm{G3}) - \mathbf{U}_0(\mathrm{G4}) + \mathbf{U}_0(\mathrm{G2}) + \mathbf{U}_0(\mathrm{G1}))\right] \tag{3.13b}$$

$$\mathbf{U}_c^{1y} = \frac{\sqrt{3}}{4}\left[\mathbf{U}_0(\mathrm{G3}) - \mathbf{U}_0(\mathrm{G2}) + \mathbf{U}_0(\mathrm{G4}) + \mathbf{U}_0(\mathrm{G1}))\right] \tag{3.13c}$$

where G_i $(i = 1, ..., 4)$ are 2D Gaussian points (see Fig. 3.1), which are mapped from a reference element via mathematical transformation:

$$\mathrm{G}_i = \left(x\left(\frac{\pm 1}{\sqrt{3}}\right), y\left(\frac{\pm 1}{\sqrt{3}}\right)\right) = \left(x_c \pm \frac{\sqrt{3}}{6}\Delta x, y_c \pm \frac{\sqrt{3}}{6}\Delta y\right) \tag{3.13d}$$

The coefficients $\mathbf{U}_c^0$, $\mathbf{U}_c^{1x}$ and $\mathbf{U}_c^{1y}$ are evolved by the local spatial operators $\mathbf{L}_c^0$, $\mathbf{L}_c^{1x}$ and $\mathbf{L}_c^{1y}$ that are obtained by considering Eq 3.12:

$$\mathbf{L}_{\boldsymbol{c}}^{\boldsymbol{K}} = -\left[(\mathbf{I}_{\boldsymbol{c}}^{\boldsymbol{K}} + \mathbf{J}_{\boldsymbol{c}}^{\boldsymbol{K}}) - (\mathbf{M}_{\boldsymbol{c}}^{\boldsymbol{K}} + \mathbf{N}_{\boldsymbol{c}}^{\boldsymbol{K}} + \mathbf{S}_{\boldsymbol{c}}^{\boldsymbol{K}})\right] \quad (K = 0, 1x, 1y) \tag{3.14}$$

The flux balance terms, $\mathbf{I}_{\boldsymbol{c}}^{\boldsymbol{K}}$ and $\mathbf{J}_{\boldsymbol{c}}^{\boldsymbol{K}}$, are computed by resolving solution discontinuities at the faces between adjacent grid elements using an approximate Riemann solver (Toro 1999, 2001), which in this work, is based on the Roe solver (Roe 1997). The term $\mathbf{I}_{\boldsymbol{c}}^{\boldsymbol{K}}$ is approximated at the Gaussian integration points (Fig. 3.1) at the Eastern (i.e. $E_{1,2} = (x(1), y(\pm\frac{1}{\sqrt{3}})) = (x_c + \frac{\Delta x}{2}, y_c \pm \frac{\sqrt{3}}{6}\Delta y))$ and the Western faces (i.e. $W_{1,2} = (x(-1), y(\pm\frac{1}{\sqrt{3}})) = (x_c - \frac{\Delta x}{2}, y_c \pm \frac{\sqrt{3}}{6}\Delta y))$, where the x-directional Riemann flux $\widetilde{\mathbf{F}}$ is evaluated by averaging across the faces. Similarly, the term $\mathbf{J}_{\boldsymbol{c}}^{\boldsymbol{K}}$ is approximated considering the Gaussian integration points (Fig. 3.1) at the Northern (i.e. $N_{1,2} = (x(\pm\frac{1}{\sqrt{3}}), y(1)) = (x_c \pm \frac{\sqrt{3}}{6}\Delta x, y_c + \Delta y/2))$ and the Southern faces (i.e. $S_{1,2} = (x(\pm\frac{1}{\sqrt{3}}), y(-1)) = (x_c \pm \frac{\sqrt{3}}{6}\Delta x, y_c - \Delta y/2))$ where the y-directional flux $\widetilde{\mathbf{G}}$ is evaluated for averaging across the faces. The terms involving volume integrals of the fluxes, $\mathbf{M}_{\boldsymbol{c}}^{\boldsymbol{K}}$ and $\mathbf{N}_{\boldsymbol{c}}^{\boldsymbol{K}}$, and the source terms, $\mathbf{S}_{\boldsymbol{c}}^{\boldsymbol{K}}$, are approximated via the 2D quadrature rules at four Gaussian points (i.e. $\mathrm{G}_1, \mathrm{G}_2, \mathrm{G}_3$ and G_4 in Eq. 3.18, with reference to Fig. 3.1).

Special notes

The spatial discretisation described within Eq. 3.14 is applied within a two-stage Runge-Kutta (RK) time integration (Eq. 3.15) to form the so-called RKDG2 approach. The RK time integration is used to update the DG2 solution from n to n+1 ($n = 1, 2, ...,$ total number of iteration):

$$(\mathbf{U}_c^{\boldsymbol{K}})^{n+1/2} = (\mathbf{U}_c^{\boldsymbol{K}})^n + \Delta t(\mathbf{L}_c^{\boldsymbol{K}})^n \tag{3.15a}$$

$$(\mathbf{U}_c^{\boldsymbol{K}})^{n+1} = \frac{1}{2}[(\mathbf{U}_c^{\boldsymbol{K}})^n + (\mathbf{U}_c^{\boldsymbol{K}})^{n+1/2} + \Delta t(\mathbf{L}_c^{\boldsymbol{K}})^{n+1/2}] \tag{3.15b}$$

in which Δt is an adaptive time step calculated using Eq. 3.16:

$$\Delta t = min\left\{\frac{CFL \times \Delta x}{|u(x,y,t)| + \sqrt{g \times h(x,y,t)}}, \frac{CFL \times \Delta y}{|v(x,y,t)| + \sqrt{g \times h(x,y,t)}}\right\} \tag{3.16}$$

where CFL is Courant–Friedrichs–Lewy (CFL) number. Each RK stage in Eq. 3.15 should be preceded by slope limiting procedure (described in detail in Chapter 4) to ensure that local DG2 slope coefficients, i.e. $\mathbf{U}_c^{1x}$ and $\mathbf{U}_c^{1y}$, have limited variation relating to slopes differentiated from the means at Q_c and its adjacent neighbours. However, it is worth noting on several key points relating to this DG2 structure.

Cross-dimensional slope dependency. The slope evolution operators $\mathbf{L}_c^{1x}$ and $\mathbf{L}_c^{1y}$ although aimed to update the x- and y-directional slope coefficients, $\mathbf{U}_c^{1x}$ and $\mathbf{U}_c^{1y}$, still depends on both slope coefficients, mainly due to the location of the evaluation points in the stencil (Fig. 3.1). In effect, at any of the relevant evaluation points - namely E_i, W_i, N_i and S_i ($i = 1, 2$) and G$_i$ ($i = 1, 2, 3$ and 4) in Fig. 3.1 - the local planar solution $\mathbf{U_h}|_{Q_c}$ reads:

$$\mathbf{U_h}(E_i,t) = \mathbf{U}_c^0(t) + \mathbf{U}_c^{1x}(t) \pm \frac{\mathbf{U}_c^{1y}(t)}{\sqrt{3}} \quad (i = 1, 2) \tag{3.17a}$$

$$\mathbf{U_h}(W_i,t) = \mathbf{U}_c^0(t) - \mathbf{U}_c^{1x}(t) \pm \frac{\mathbf{U}_c^{1y}(t)}{\sqrt{3}} \quad (i = 1, 2) \tag{3.17b}$$

$$\mathbf{U_h}(N_i, t) = \mathbf{U}_c^0(t) \pm \frac{\mathbf{U}_c^{1x}(t)}{\sqrt{3}} + \mathbf{U}^{1y}(t) \quad (i = 1, 2) \tag{3.17c}$$

$$\mathbf{U_h}(S_i, t) = \mathbf{U}_c^0(t) \pm \frac{\mathbf{U}_c^{1x}(t)}{\sqrt{3}} - \mathbf{U}^{1y}(t) \quad (i = 1, 2) \tag{3.17d}$$

$$\mathbf{U_h}(\mathrm{G}_i, t) = \mathbf{U}_c^0(t) \pm \frac{\mathbf{U}_c^{1x}(t)}{\sqrt{3}} \pm \frac{\mathbf{U}_c^{1y}(t)}{c} \quad (i = 1, ..., 4) \tag{3.18}$$

for which, as in Eqs. 3.17 to 3.18, both x- and y-directional slope coefficients must be present in any of the evaluations.

Impact of the slope limiter. The slope limiter in DG formulation comes in as an FV tool aimed to stabilise the solution around sharp discontinuities (i.e. avoid the development of the Gibbs phenomenon). Nonetheless, it is generally demonstrated that slope limiters may have adverse effects such as distorting the solution around smooth areas (Marras et al. 2016, Krivodonova et al. 2004, Sanders & Bradford 2006, An & Yu 2014, Kesserwani & Liang 2012*c*). To reduce such an impact on DG predictions, the slope limiting process may be localised based on the so-called troubled cell indicator (Qiu & Shu 2005), such as the shock detector in (Krivodonova et al. 2004) used in this study. Further information on the shock detector used in this research is provided in Chapter 4. However, given the cross-dimensional slope dependency issue raised above, any potential impact due to slope limiting would be omnipresent across all the evaluations.

Operational costs. At each RK stage, the DG2 discretisation requires solving 8 different Riemann problems to calculate the flux balance terms, 8 Gaussian point evaluations to calculate the flux volume integrals, and 16 Gaussian point evaluations to calculate the volume integrals of the source terms. Hence, at least 32 spatial operations are needed to enable progressing the state of the solution over one grid element by half a time step, which is computationally expensive.

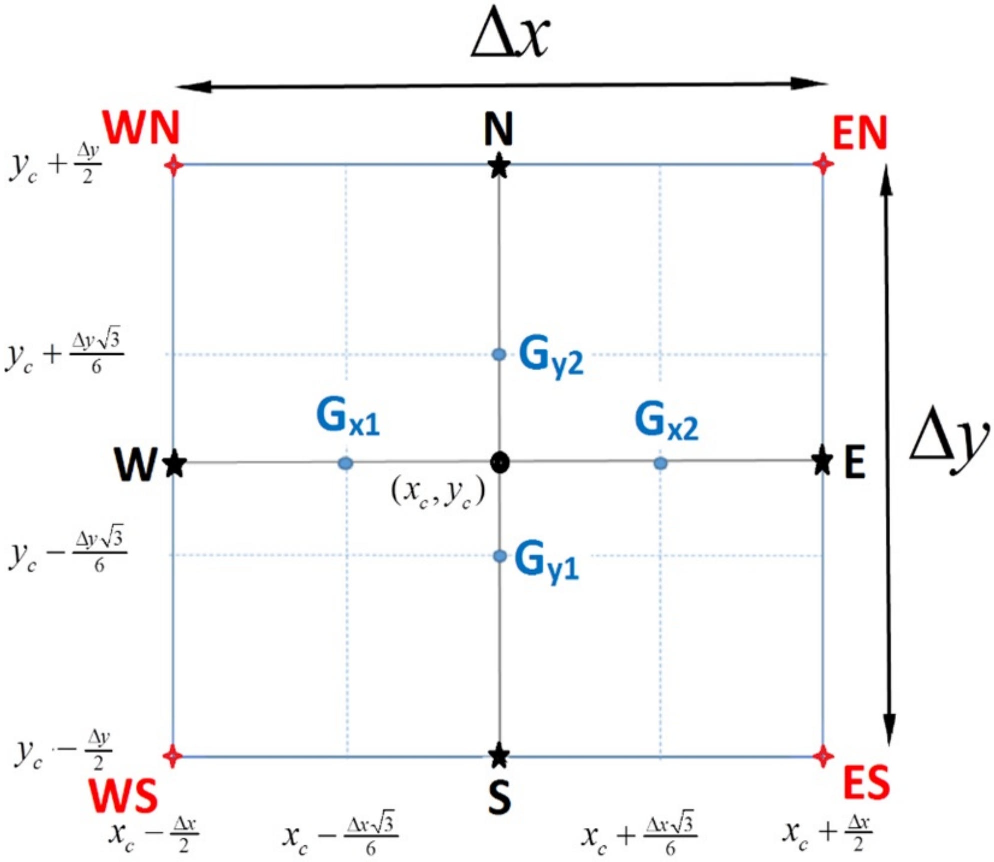

Figure 3.2: *Stencil of a grid element Q_c for the simplified DG2 formulation. Two different sets of Gaussian points $\{G_{xi}\}_{i=1,2}$ and $\{G_{yi}\}_{i=1,2}$ are involved in a fully decoupled manner along the horizontal and vertical centrelines, respectively. Furthermore, only a single evaluation for the Riemann flux at any of the four faces is sought, involving the centres E and W of the eastern and western faces along $[G_{x1}, G_{x2}]$ and N and S of the northern and southern faces along $[G_{y1}, G_{y2}]$. Points EN, ES, WS and WN indicate the corner of Q_c that are named based on the two faces they connect (e.g., WS indicates the corner point at which the western and southern faces intersect).*

3.2.2 Simplified DG2 formulation

A simplified DG2 formulation is presented using the same choice for the local basis functions as in Sec. 3.2.1, but based upon a different local stencil, which is described in Fig. 3.2. As shown in this figure, there are now two different sets of Gaussian points, $\{\mathrm{G}_{xi}\}_{i=1,2}$ and $\{\mathrm{G}_{yi}\}_{i=1,2}$, that are involved in an entirely decoupled manner along the x- and y-directional centrelines, respectively. With this setting, the set $\{\mathrm{G}_{xi}\}_{i=1,2}$ is applied to approximate all the integral terms in the operator $\mathbf{L}_c^{1x}$, considering no variation occur along the y-direction. Similarly, the set $\{\mathrm{G}_{yi}\}_{i=1,2}$ is used to approximate all the integral terms in the operator $\mathbf{L}_c^{1y}$ considering no variation occur along the x-direction. Also, only one evaluation for the flux at any of the four faces is required, namely at points E and W that are located at the centre of the eastern and western faces, and points N and S located at the centre of the northern and southern faces. These points are positioned along the centrelines of the grid element Q_c that intersect at its centre whilst crossing the Gaussian points $[\mathrm{G}_{x1}, \mathrm{G}_{x2}]$ and $[\mathrm{G}_{y1}, \mathrm{G}_{y2}]$ respectively (Fig. 3.2). The main purpose of adopting this stencil is to decouple the slope dependencies in the all evaluations with respect to the Cartesian directions. This can be easily shown, considering the stencil depicted in Fig. 3.2, that any local evaluation at the relevant points only involves one slope coefficient, namely:

$$\mathbf{U_h}(E,t) = \mathbf{U}_c^0(t) + \mathbf{U}_c^{1x}(t) \tag{3.19a}$$

$$\mathbf{U_h}(W,t) = \mathbf{U}_c^0(t) - \mathbf{U}_c^{1x}(t) \tag{3.19b}$$

$$\mathbf{U_h}(N,t) = \mathbf{U}_c^0(t) + \mathbf{U}_c^{1y}(t) \tag{3.19c}$$

$$\mathbf{U_h}(S,t) = \mathbf{U}_c^0(t) - \mathbf{U}_c^{1y}(t) \tag{3.19d}$$

$$\mathbf{U}_{\mathbf{h}}(\mathrm{G}_{xi}, t) = \mathbf{U}_c^0(t) \pm \frac{\mathbf{U}_c^{1x}(t)}{\sqrt{3}} (i = 1, 2) \tag{3.20a}$$

$$\mathbf{U}_{\mathbf{h}}(\mathrm{G}_{yi}, t) = \mathbf{U}_c^0(t) \pm \frac{\mathbf{U}_c^{1y}(t)}{\sqrt{3}} (i = 1, 2) \tag{3.20b}$$

As opposed to Eqs. 3.17 to 3.18, Eqs. 3.19 to 3.20 result in sole involvement of the x-directional (or y-directional) slope coefficient in the evaluation of the Riemann problem and integral terms involving the x-directional flux $\mathbf{F}$ (or y-directional flux $\mathbf{G}$) within the $\mathbf{L}_c^0$, $\mathbf{L}_c^{1x}$ and $\mathbf{L}_c^{1y}$ local spatial operators. Considering also that the x-directional and y-directional variations of the local planar solution are zero along the y-direction and x-direction, the following spatial operators can be obtained for updating the mean and slope coefficients over Q_c over an RK time stage:

$$\mathbf{L}_c^0 = -\frac{1}{\Delta x}\left(\widetilde{\mathbf{F}}_E - \widetilde{\mathbf{F}}_W\right) - \frac{1}{\Delta y}\left(\widetilde{\mathbf{F}}_N - \widetilde{\mathbf{F}}_S\right) + \mathbf{S}(\mathbf{U}_{\mathbf{h}}(x_c, y_c), t)) \tag{3.21a}$$

$$\begin{aligned}\mathbf{L}_c^{1x} = -\frac{3}{\Delta x}\Bigg\{ &(\widetilde{\mathbf{F}}_E + \widetilde{\mathbf{F}}_W) - (\mathbf{F}(\mathbf{U}_{\mathbf{h}}(\mathrm{G}_{x2}, t)) + \mathbf{F}(\mathbf{U}_{\mathbf{h}}(\mathrm{G}_{x1}, t))) \\ &- \frac{\Delta x\sqrt{3}}{6}\left[\mathbf{S}(\mathbf{U}_{\mathbf{h}}(\mathrm{G}_{x2}, t)) - \mathbf{S}(\mathbf{U}_{\mathbf{h}}(\mathrm{G}_{x1}, t))\right]\Bigg\}\end{aligned} \tag{3.21b}$$

$$\begin{aligned}\mathbf{L}_c^{1y} = -\frac{3}{\Delta y}\Bigg\{ &(\widetilde{\mathbf{F}}_N + \widetilde{\mathbf{F}}_S) - (\mathbf{G}(\mathbf{U}_{\mathbf{h}}(\mathrm{G}_{y2}, t)) + \mathbf{G}(\mathbf{U}_{\mathbf{h}}(\mathrm{G}_{y1}, t))) \\ &- \frac{\Delta y\sqrt{3}}{6}\left[\mathbf{S}(\mathbf{U}_{\mathbf{h}}(\mathrm{G}_{y2}, t)) - \mathbf{S}(\mathbf{U}_{\mathbf{h}}(\mathrm{G}_{y1}, t))\right]\Bigg\}\end{aligned} \tag{3.21c}$$

where $\widetilde{\mathbf{F}}_E = \widetilde{\mathbf{F}}(\mathbf{U}_{\mathbf{h}}(E^-, t), \mathbf{U}_{\mathbf{h}}(E^+, t))$, $\widetilde{\mathbf{F}}_W = \widetilde{\mathbf{F}}(\mathbf{U}_{\mathbf{h}}(W^-, t), \mathbf{U}_{\mathbf{h}}(W^+, t))$, $\widetilde{\mathbf{F}}_N = \widetilde{\mathbf{F}}(\mathbf{U}_{\mathbf{h}}(N^-, t)$, $\mathbf{U}_{\mathbf{h}}(N^+, t))$ and $\widetilde{\mathbf{F}}_E = \widetilde{\mathbf{F}}(\mathbf{U}_{\mathbf{h}}(S^-, t), \mathbf{U}_{\mathbf{h}}(S^+, t))$ represent the Riemann flux evaluations across the eastern, western, northern and southern faces of the element Q_c, considering the limited slope coefficients in Eqs. 3.19-3.20 with the same localised slope limiter as in the standard formulation (Sec. 3.2.1). When compared to the standard DG2 formulation, the simplified formulation (Eqs. 3.21) reduces the total number of operations from 32 to 12 (4 Riemann problem solutions and 8 Gaussian point evaluations), leading to a drastic reduction in operational cost. The simplified DG2 formulation is thus expected to offer speed up in runtime relative to the standard DG2 formulation by a factor of 2.6 (see also Sec. 3.3.1). It also has the advantage of being well-balanced for all mean and slope coefficients as discussed in the next subsection.

2D-SWE with bed topography

The conventional form of the 2D-SWE can be expressed by Eq. 3.1, assuming that:

$$\mathbf{U} = \begin{bmatrix} h \\ q_x \\ q_y \end{bmatrix}, \quad \mathbf{F} = \begin{bmatrix} q_x \\ \frac{q_x^2}{h} + \frac{g}{2}h^2 \\ \frac{q_x q_y}{h} \end{bmatrix}, \quad \mathbf{G} = \begin{bmatrix} q_y \\ \frac{q_x q_y}{h} \\ \frac{q_y^2}{h} + \frac{g}{2}h^2 \end{bmatrix} \quad \text{and} \quad \mathbf{S} = \begin{bmatrix} 0 \\ -gh\partial_x z \\ -gh\partial_y z \end{bmatrix} \tag{3.22}$$

where $h(x, y, t)$ represents the water depth, $q_x = hu$ and $q_y = hv$ are volumetric discharges per unit width expressed in terms of the velocities $u(x, y, t)$ and $v(x, y, t)$ along the Cartesian directions, g represents the acceleration due to gravity, and $\partial_x z$ and $\partial_y z$ are the partial derivatives of a topography function $z(x, y)$.

The system of Eqs. 3.1 and 3.22 (which is similar to Eq. 2.1 in Chapter 2 without the friction terms) may be referred to as non-homogeneous hyperbolic conservation laws (Xing & Shu 2014) when $z(x, y) \neq 0$. A known challenge is to find a straightforward discretisation of the source terms that balances the flux gradients when the flow admits steady state solutions, i.e. producing a well-balanced 2D-SWE solver (Xing & Shu 2014). In principle, a well-balanced DG2 solver should preserve the 'lake-at-rest' stationary solution over an uneven topography (Xing & Shu 2014), for which the conditions are:

$$h + z = \text{constant} \quad \text{and} \quad (q_x, q_y) = (0, 0) \tag{3.23}$$

In the context of practical hydrodynamic simulations, the design of a well-balanced DG2 solver that retains the condition in Eq. 3.23 faces numerous challenges, including: (a) the DG2 solver should verify the discrete balance between the gradients of the fluxes and the topography; (b) the DG2 solver should remain stable for a flow over a steep terrain, e.g. a building-like block, where the topography function is not differentiable; (c) all DG2 operators in Eqs. 3.21 should be well-balanced with respect to the mean coefficient, $\mathbf{U}_c^0$, and the slope coefficients, $\mathbf{U}_c^{1x}$ and $\mathbf{U}_c^{1y}$, as well. In the next subsection, we later demonstrate that the simplified DG2 operators can offer a simple approach to effectively address these challenges.

Well-balancedness consideration in the simplified 2D-SWE DG2 solver

The simplified DG2 operators in Eqs. 3.21 are considered to study the well-balancedness for the DG2 planar solution in Eq. 3.12. An appropriate initial projection, considering the stencil in Fig. 3.2, is vital to achieve well-balancedness. The initial conditions for the local coefficients in Eqs. 3.13 can be made valid on this stencil by involving the evaluations at the corner points EN, ES, WS and WN as they are present in both stencils (Figs. 3.1 and 3.2):

$$\mathbf{U}_c^0(0) = \frac{1}{4}\left[\mathbf{U}_0(EN) + \mathbf{U}_0(ES) + \mathbf{U}_0(WS) + \mathbf{U}_0(WN)\right] \tag{3.24a}$$

$$\mathbf{U}_c^{1x}(0) = \frac{1}{4}\left[\mathbf{U}_0(EN) - \mathbf{U}_0(WN) + \mathbf{U}_0(ES) - \mathbf{U}_0(WS)\right] \tag{3.24b}$$

$$\mathbf{U}_c^{1y}(0) = \frac{1}{4}\left[\mathbf{U}_0(EN) - \mathbf{U}_0(ES) + \mathbf{U}_0(WN) - \mathbf{U}_0(WS)\right] \tag{3.24c}$$

In turn, given the slope-decoupled formulation, integrating over a coordinate direction the information at the faces considering the other direction are averaged, which leads to the following relationships:

$$\frac{1}{2}\left(\mathbf{U}_0(EN) + \mathbf{U}_0(ES)\right) = \mathbf{U}_0(E) \tag{3.25a}$$

$$\frac{1}{2}\left(\mathbf{U}_0(WN)+\mathbf{U}_0(WS)\right)=\mathbf{U}_0(W) \tag{3.25b}$$

$$\frac{1}{2}\left(\mathbf{U}_0(EN)+\mathbf{U}_0(WN)\right)=\mathbf{U}_0(N) \tag{3.25c}$$

$$\frac{1}{2}\left(\mathbf{U}_0(WS)+\mathbf{U}_0(ES)\right)=\mathbf{U}_0(S) \tag{3.25d}$$

By substituting Eqs. 3.25 into Eqs. 3.24, the initial conditions for the coefficients can be rewritten so that to involve the nodes E, W, N and S (see Fig. 3.2) where key treatments are performed:

$$\mathbf{U}_c^0(0)=\frac{1}{2}\left[\mathbf{U}_0(E)+\mathbf{U}_0(W)\right]=\frac{1}{2}\left[\mathbf{U}_0(N)+\mathbf{U}_0(S)\right] \tag{3.26a}$$

$$\mathbf{U}_c^{1x}(0)=\frac{1}{2}\left[\mathbf{U}_0(E)-\mathbf{U}_0(W)\right] \tag{3.26b}$$

$$\mathbf{U}_c^{1y}(0)=\frac{1}{2}\left[\mathbf{U}_0(N)-\mathbf{U}_0(S)\right] \tag{3.26c}$$

Eqs. 3.26 becomes relevant when linking the DG2 coefficients to the *inter-elemental nodes* at the grid element faces where flux exchange occurs, hence making them suited to address any change occurring at the nodes due to wetting and drying treatments. Also, Eqs. 3.26 reveal even more clearly that the planar topography projections, denoted by $z_h(x,y)|_{Q_c}$ over Q_c with coefficients z_c^0, z_c^{1x} and z_c^{1y} defined as in Eqs. 3.24, are continuous at all four main nodes, E, W, N and S, considering the stencil in Fig. 3.2. For instance, considering the topography approximation across the inter-elemental node E, which is shared by the grid elements Q_c and Q_{c+1}, yields:

$$z_h(E^-)|_{Q_c}=z_c^0+z_c^{1x}=z_h(E)=z_{c+1}^0-z_{c+1}^{1x}=z_h(E^+)|_{Q_c} \tag{3.27}$$

Another key issue is how to evaluate the derivative of the local topography projection $\partial_x z_h|_{Q_c}$ and $\partial_y z_h|_{Q_c}$ while remaining consistent with the stencil in Fig. 3.2. A straight forward method would be to derive them from the following local planar solution, $z_h|_{Q_c}$:

$$z_h|_{Q_c} = z_c^0 + \frac{(x - x_c)}{\Delta x/2} z_c^{1x} + \frac{(y - y_c)}{\Delta y/2} z_c^{1y} \tag{3.28}$$

which has constant slope coefficients over Q_c and thus leads to the following local bed slope terms:

$$\partial_x z_h|_{Q_c} = \left(\frac{2}{\Delta x} z_c^{1x} \right) \tag{3.29a}$$

$$\partial_y z_h|_{Q_c} = \left(\frac{2}{\Delta y} z_c^{1y} \right) \tag{3.29b}$$

Eqs. 3.29 that are used to discretise the local bed slope terms is sufficient to ensure well-balancedness for the mean coefficients. However, this introduces irrelevant cross-dimensional slope dependencies (e.g. z_c^{1x} within $\mathbf{L}_c^{1y}$ across the DG2 operators responsible for the update of slope coefficients (see the mathematical proof in Appendix A)), leading to mild unbalancedness in the slope coefficients of the discharges, which might eventually impact the well-balancedness of all the coefficients (as shown later in Section 3.3.2). Therefore, an alternative slope-decoupled discretisation for the local bed gradients is here proposed:

$$\partial_x \left[z_h(0, y)|_{x=0} \right] = 0 \quad \text{and} \quad \partial_x z_h|_{y=0} = \partial_x \left[z_h(x, 0)|_{Q_c} \right] = \left(\frac{2}{\Delta x} \right) z_c^{1x} \tag{3.30a}$$

$$\partial_y \left[z_h(x, 0)|_{y=0} \right] = 0 \quad \text{and} \quad \partial_y z_h|_{x=0} = \partial_y \left[z_h(0, y)|_{Q_c} \right] = \left(\frac{2}{\Delta y} \right) z_c^{1y} \tag{3.30b}$$

In addition, the positivity-preserving amendments are applied to retain the well-balanced property in the presence of wetting and drying. By denoting $\mathbf{U}_E^{\pm}$, $\mathbf{U}_W^{\pm}$, $\mathbf{U}_N^{\pm}$, and $\mathbf{U}_S^{\pm}$ as the limits of the DG2 solutions at the nodes E, W, N and S (Fig. 3.2), such that:

$$\mathbf{U}_E^{\pm} = \mathbf{U_h}(E^{\pm}) = \left[h_E^{\pm}, (q_x)_E^{\pm}, (q_y)_E^{\pm}\right]^T \quad \text{and} \quad z_E = z_h(E^{\pm}) \tag{3.31a}$$

$$\mathbf{U}_W^{\pm} = \mathbf{U_h}(W^{\pm}) = \left[h_W^{\pm}, (q_x)_W^{\pm}, (q_y)_W^{\pm}\right]^T \quad \text{and} \quad z_W = z_h(W^{\pm}) \tag{3.31b}$$

$$\mathbf{U}_N^{\pm} = \mathbf{U_h}(N^{\pm}) = \left[h_N^{\pm}, (q_x)_N^{\pm}, (q_y)_N^{\pm}\right]^T \quad \text{and} \quad z_N = z_h(N^{\pm}) \tag{3.31c}$$

$$\mathbf{U}_S^{\pm} = \mathbf{U_h}(S^{\pm}) = \left[h_S^{\pm}, (q_x)_S^{\pm}, (q_y)_S^{\pm}\right]^T \quad \text{and} \quad z_S = z_h(S^{\pm}) \tag{3.31d}$$

their positivity-preserving reconstructions will be denoted by $\left\{\mathbf{U}_E^{\pm,*}, z_E^*\right\}$,$\left\{\mathbf{U}_W^{\pm,*}, z_W^*\right\}$, $\left\{\mathbf{U}_N^{\pm,*}, z_N^*\right\}$ and $\left\{\mathbf{U}_S^{\pm,*}, z_S^*\right\}$. Eqs. 3.26 are then applied to redefine the positivity-preserving coefficients as follows:

$$\overline{\mathbf{U}}_c^{0x}(t) = \frac{1}{2}\left[\mathbf{U}_E^{-,*} + \mathbf{U}_W^{+,*}\right] \tag{3.32a}$$

$$\overline{\mathbf{U}}_c^{0y}(t) = \frac{1}{2}\left[\mathbf{U}_N^{-,*} + \mathbf{U}_S^{+,*}\right] \tag{3.32b}$$

$$\overline{\mathbf{U}}_c^{1x}(t) = \frac{1}{2}\left[\mathbf{U}_E^{-,*} - \mathbf{U}_W^{+,*}\right] \tag{3.32c}$$

$$\overline{\mathbf{U}}_c^{1y}(t) = \frac{1}{2}\left[\mathbf{U}_N^{-,*} - \mathbf{U}_S^{+,*}\right] \tag{3.32d}$$

It is worth noting that Eqs. 3.32a and 3.32b are identical as long as no change occur at any node due to wetting and drying. This decoupled form for the mean coefficients (i.e. Eqs. 3.32a-3.32b) is consistent with slope decoupling, and yet necessary to preserve well-balancedness for the slope coefficients when wetting and drying occur at any of the nodes

E, W, N or S (Fig. 3.2). In addition to Eqs. 3.32, the bed gradient terms need to be re-defined in relation to potential change made by the wetting and drying at any of the nodes, as follows:

$$\overline{z}_c^{1x} = \frac{1}{2}\left[z_E^* - z_W^*\right] \tag{3.33a}$$

$$\overline{z}_c^{1y} = \frac{1}{2}\left[z_N^* - z_S^*\right] \tag{3.33b}$$

3.3 Test results and discussions

In this section, numerical results for selected 2D test cases are presented to compare the simplified DG2 formulation with the standard DG2 formulation, and verify its conservation properties for practical shallow water modelling. Section 3.3.1 contains a comparative investigation on the accuracy of the simplified DG2 formulation against the standard version based on classical benchmark tests (the linear advection and the radial dam-break tests). Section 3.3.2 explores the conservative properties of the simplified DG2 solver (well-balancedness and accuracy) with test cases involving uneven topographies and wetting-drying processes. For both solvers, the selected CFL number is set equal to 0.25, and the limiting of the slope coefficients is applied when the shock detector in Krivodonova et al. (2004) exceed the threshold 100.

3.3.1 Standard *vs.* simplified DG2 formulation

The standard and simplified DG2 formulation are hereby benchmarked and compared against analytical or reference data. Two numerical 2D tests are considered involving bi-directional flows in order to entirely investigate the 2D character of the formulation. Quantitative analyses are conducted to investigate the grid convergence rate of the DG2 formulation in the case of the 2D inviscid linear advection equation. A qualitative assessment of the DG2 ability in reproducing wave non-linearity and discontinuities relevant to a classical radial dam-break flow is also provided.

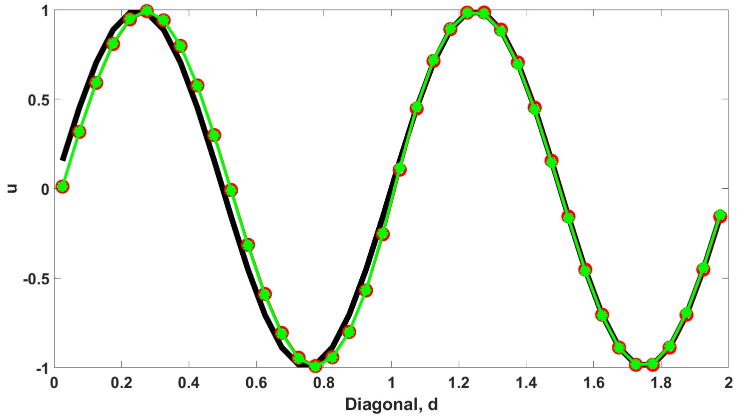

Figure 3.3: *Numerical results of the exact (black line), the standard DG2 form (red-dotted line) and the simplified DG2 form (green-dotted line) along the diagonal (using 40 × 40 grids).*

Quantitative assessment

To compare the performance of the standard and simplified DG2 formulation, a 2D linear advection equation (Toro 1999) is considered, which is usually the model equation on which numerical methods solving hyperbolic conservation laws were initially developed (Toro 1999):

$$\partial_t u + a\partial_x u + b\partial_y u = 0 \tag{3.34}$$

Equation 3.34 is solved over a 2D domain $[0, 2]^2$ with characteristic speed coefficient $a = b = 1$. The initial condition is $u(x, y, 0) = sin(\pi(x + y))$ and boundary conditions are set to be periodic. Simulations are run up to $t = 1$ s on $M_Q \times N_Q = 10 \times 10$, 20×20, 40×40, 80×80 and 160×160 grid elements, respectively.

Fig. 3.3 illustrates the mean coefficients produced by the standard and simplified DG2 formulation extracted diagonally from the grid enclosing 40 × 40 grid elements and at $t = 1$ s. Both DG2 form appear to consistently predict the undulant characteristics observed in the analytical solution. Fig 3.4 displays the local 2D planar solutions (i.e. via Eq. 3.12) associated with both DG2 predictions, showing a similar qualitative behaviour despite the difference in the stencils involved. To compare the formulation based on quantitative metrics, accuracy-order and runtime cost analyses are performed. Table 3.1 contains the relative errors

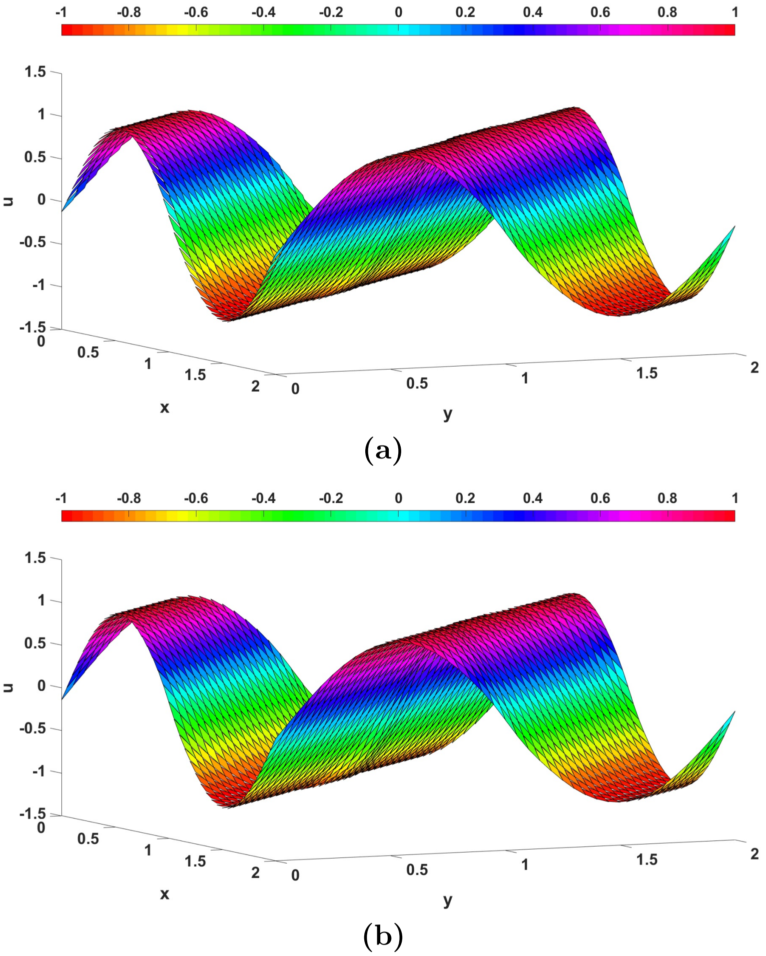

Figure 3.4: *The 2D full planar solutions* ($u_h(x, y, t = 1\,s)|_{Q_c}$) *for the (a) standard DG2 form and (b) simplified DG2 form for the 20 × 20 grid domain.*

Table 3.1: *L^1-norm, L^2-norm and L^∞-norm errors and orders of accuracy of the standard and simplified DG2 formulation and their CPU times (relevant to the test in Sec. 2.4.1).*

DG2 solver	Grid size	L^1- error	L^1- order	L^2- error	L^2- order	L^∞- error	L^∞- order	Runtime (s)
Standard	10×10	$3.86e^{-02}$	-	$4.11e^{-02}$	-	$5.98e^{-02}$	-	4.0
	20×20	$8.70e^{-03}$	2.148	$1.03e^{-02}$	1.993	$1.53e^{-02}$	1.963	15.9
	40×40	$2.00e^{-03}$	2.153	$2.50e^{-03}$	2.020	$3.60e^{-03}$	2.071	62.5
	80×80	$4.68e^{-04}$	2.067	$6.02e^{-04}$	2.081	$8.57e^{-04}$	2.090	243.6
	160×160	$1.17e^{-04}$	2.001	$1.34e^{-04}$	2.167	$1.93e^{-}04$	2.153	960.0
Simplified	10×10	$4.97e^{-02}$	-	$5.22e^{-02}$	-	$7.41e^{-02}$	-	1.8
	20×20	$1.00e^{-02}$	2.311	$1.20e^{-02}$	2.116	$1.74e^{-02}$	2.089	6.5
	40×40	$2.10e^{-03}$	2.268	$2.70e^{-03}$	2.130	$3.90e^{-03}$	2.151	24.5
	80×80	$4.87e^{-04}$	2.095	$6.22e^{-04}$	2.145	$8.92e^{-04}$	2.136	97.0
	160×160	$1.21e^{-04}$	2.003	$1.38e^{-04}$	2.170	$1.97e^{-04}$	2.176	381.8

between the analytical and numerical solutions taken along the diagonal centreline, namely $Error = (1/M_Q \times N_Q)||u_{exact}–u_{DG2}||/||u_{exact}||$, which are evaluated considering L^1–norm (also known as the mean absolute error), L^2–norm (i.e. the root mean square error) and L^∞–norm (i.e. the maximum absolute error). These error metrics, along with their respective rate of convergence, are often used to assess the performance of newly-developed or updated numerical methods (Chartres & Stepleman 1972, Cockburn & Shu 2001, Eskilsson & Sherwin 2004, Bunya et al. 2009, Duran & Marche 2014). The rate of convergence is expressed in Eq. 3.35 as shown below:

$$L^{1,2,\infty}\text{-order} = \frac{log(\frac{e_{finer}}{e_{current}})}{log(\frac{M_Q(current)}{M_Q(finer)})} \tag{3.35}$$

where $e_{current}$ and $M_Q(current)$ are the error value and the grid size of the current grid, whilst e_{finer} and $M_Q(finer)$ are the error value and the grid size of the immediate finer grid. The errors and the rate of convergence are calculated and shown in Table 3.1 for both the standard and the simplified DG2 formulation based on the aforementioned series of grids, together with their CPU runtimes. It can be observed in the table that the L^1–norm, L^2–norm and L^∞-norm errors of the simplified DG2 formulation are consistently slightly larger than those of the standard DG2 formulation. This clearly indicates that the simplified DG2 version is, as expected, slightly less accurate than the standard DG2 formulation. Nonetheless, looking at the rate of convergence in Table 3.1 in terms of L^1–norm, L^2–norm and L^∞-orders, the simplified DG2 formulation can deliver second-order accurate predictions, which are practically as good as the standard DG2 formulation and, in this respect, constitutes a formally second-order accurate alternative. It is worth stating that relatively similar error and accuracy-order results are obtained by considering the full 2D profiles of the analytical and numerical solutions as with those from the 1D diagonal centreline. In terms of speed up ratio between the two DG2 solvers, the CPU runtimes in Table 3.1 indicate a range between 2.25 and 2.55, which is pretty close to the predicted operational cost ratio of 2.6 (Sec. 2.3).

Qualitative assessment

To further compare the performances of the DG2 formulation in shallow water applications, a circular dam-break test (Toro 2001) is here considered. Such test is appropriate for testing the 2D-SWE DG2 solvers' ability to simulate shock propagating and rarefaction waves as it considers the instantaneous collapse of a circular dam on a flat bed. Water in the dam is contained by a thin 2.5 m radius circular wall centred at $x_c = 0$ m, $y_c = 0$ m. The water depth is 2.5 m inside the dam and 0.5 m outside. The model is a 40 m × 40 m square domain made up of 201 × 201 grids. Initial velocities u (along x) and v (along y) are set equal to zero and slip numerical boundary conditions are used. The reference solution (Toro 2001) is obtained using a 1D MUSCL-FV2 solver (Kesserwani 2013) of the 1D radial-symmetric version of the 2D-SWE that is modelled on 1001 grid elements.

Fig. 3.5 shows the free surface elevation and velocity plots in the radial direction for the reference solution, the standard DG2 solver and the simplified DG2 solver. Immediately after the initial collapse of the dam, a primary shock wave began to propagate away from the centre, while a rarefaction wave moves inwardly and reaches the centre at $t = 0.4$ s (Fig. 3.5a) with a well-defined depth gradient developed behind the shock wave. At $t = 0.7$ s (Fig. 3.5b), the rarefaction wave has fully imploded at the centre and reflects radially outward, creating a small dip in the free surface where the velocity is nearing zero. At $t = 1.4$ s (Fig. 3.5c), the primary shock wave continues to move away from the centre and the free surface has dropped below the initial water depth outside of the dam. A secondary shock wave has also formed at this time, as clearly shown by the velocity profile, which exhibits two small and yet sharp fronts behind the primary shocks. At $t = 3.5$ s (Fig. 3.5d), the primary shock is approaching the boundary while the secondary shock is travelling in the opposite direction with the free surface falling very close to the bed. Finally, at $t = 4.7$ s (Fig. 3.5e), the primary shock is about to reach the boundary while the secondary shock has imploded in the centre and reflects outwardly, resulting in another dip in the free surface at the centre.

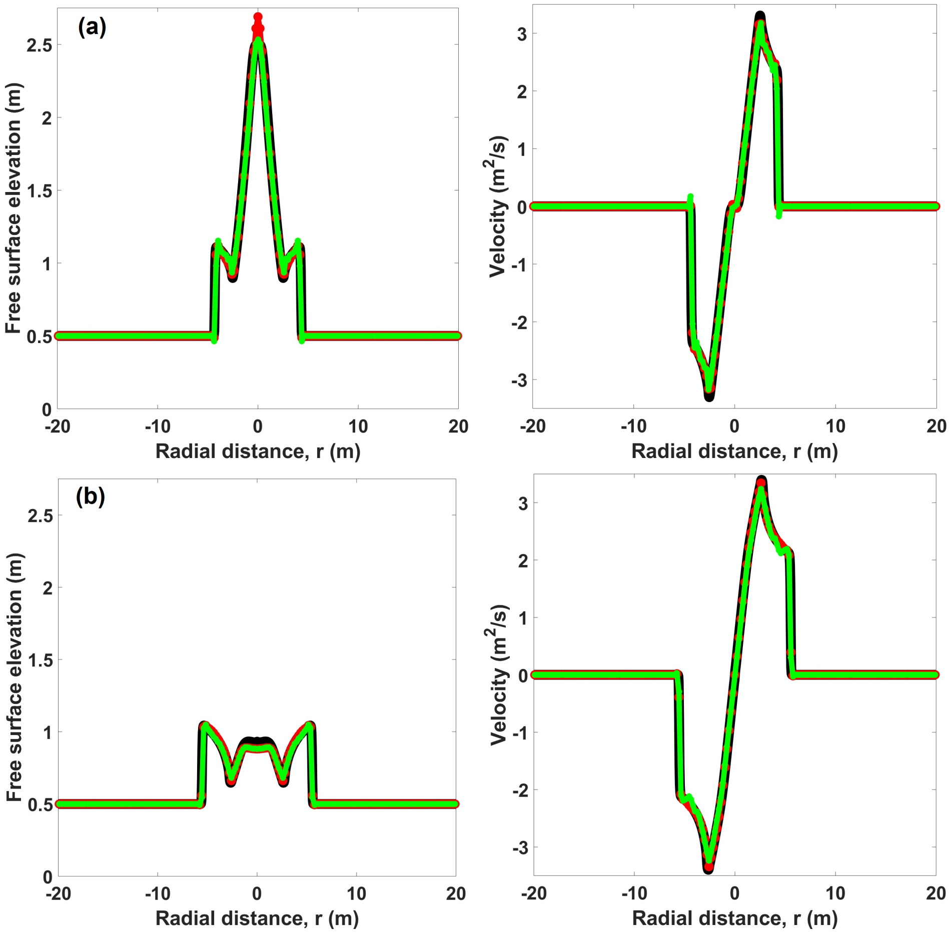

Figure 3.5: *The free surface elevation and velocity plots for the reference solution (black line), standard DG2 solver (red line) and simplified DG2 solver (green line) for (a) t = 0.4 s, (b) t = 0.7 s, (c) t = 1.4 s, (d) t = 3.5 s, and (e) t = 4.7 s.(cont.)*

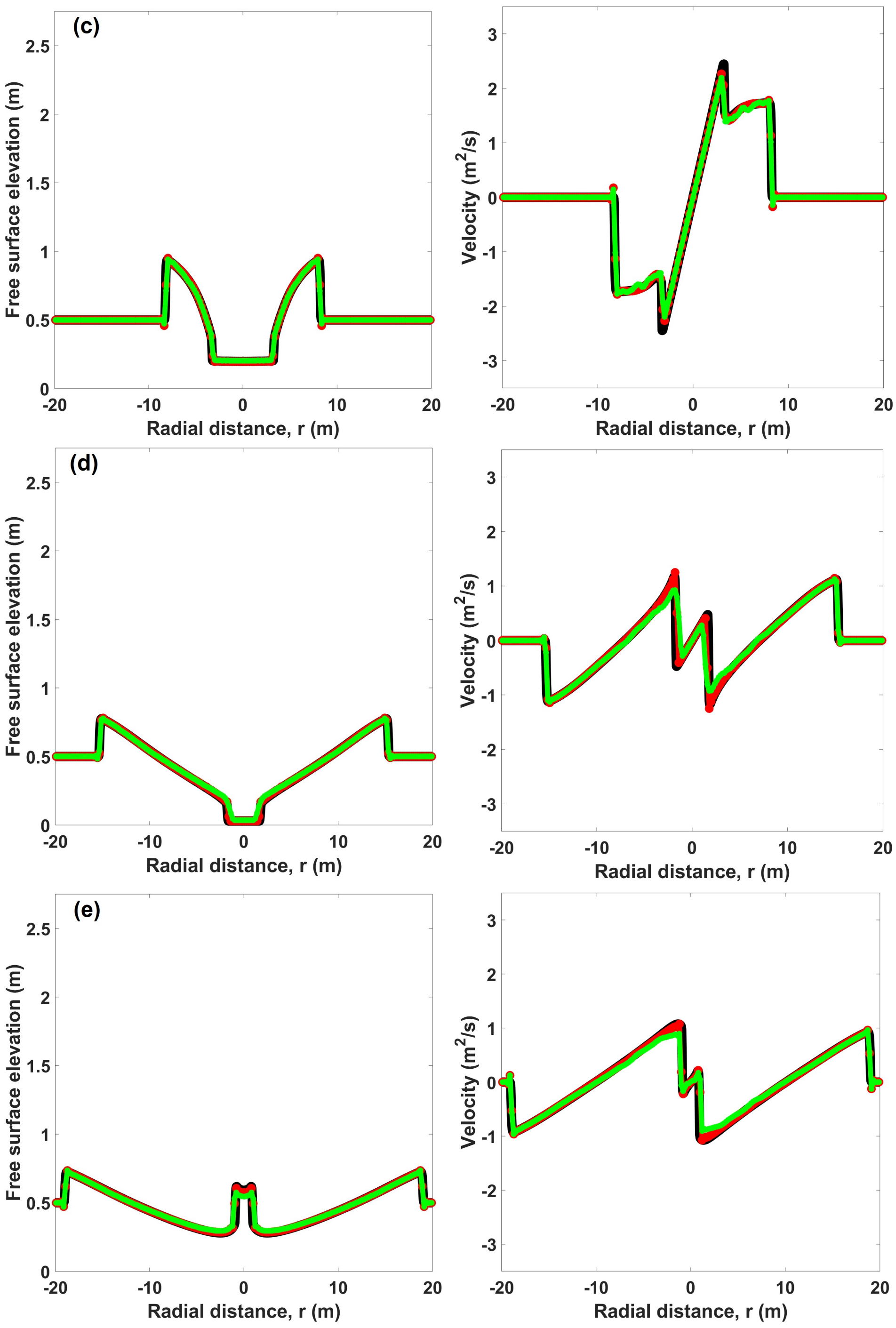

Figure 3.5: *The free surface elevation and velocity plots for the reference solution (black line), standard DG2 solver (red line) and simplified DG2 solver (green line) for (a) t = 0.4 s, (b) t = 0.7 s, (c) t = 1.4 s, (d) t = 3.5 s, and (e) t = 4.7 s.*

As seen in Fig. 3.5a, at $t = 0.4$ s, the standard DG2 solver satisfactorily corresponds with the reference solution, except at the peak free surface elevation associated with local zero velocities. There, it shows a slight overestimation as compared to the simplified DG2 version. This seems to indicate that the standard DG2 solver is much more sensitive to slope variations around points of critical flow. The discrepancy between the two DG2 solvers is also due to the convoluted involvement of both directional slope coefficients combined with the over-allowing character of the shock detector adopted for local limiting. In other words, its overlooking effects (to reduce the applicability of the slope limiter) are expected to double when applied with the standard DG2 solver. However, such discrepancy does not affect the overall performance of the solver, as one may observe in the predictions at $t = 0.7$ s and $t = 1.4$ s (Fig. 3.5b and Fig. 3.5c). At these times, the flow only entails primary waves and both DG2 solvers provide predictions very similar to the reference solutions. When the secondary waves emerge at $t = 3.5$ s and $t = 4.7$ s (Fig. 3.5d and Fig. 3.5e), the predictive capability of the standard DG2 and the simplified DG2 solvers becomes more distinct in the results, especially around the flow features defined by the secondary shock fronts and associated pattern where the standard version clearly outperforms. However, the simplified DG2 solver still delivers 2D predictions that are close to those achieved by the standard DG2 solver, and can satisfactory follow the sequence and form of the shock and rarefaction waves produced by the reference solutions.

3.3.2 Verification of simplified DG2 properties

The previous tests have shown that the simplified 2D-SWE DG2 solver is formally second-order accurate and is able to capture complex wave propagation with predictive accuracy quite similar to the standard DG2 solver. Here, the ability of the simplified DG2 solver in preserving numerical conservation properties is further assessed. This involves 2D numerical tests aimed to assess the well-balanced property of the solver for various scenarios involving smooth and sharp-edged terrain shapes with presence of wet-dry zones in the domain, and to preserve accuracy-order when the flow is subjected to constantly moving of wet-dry fronts

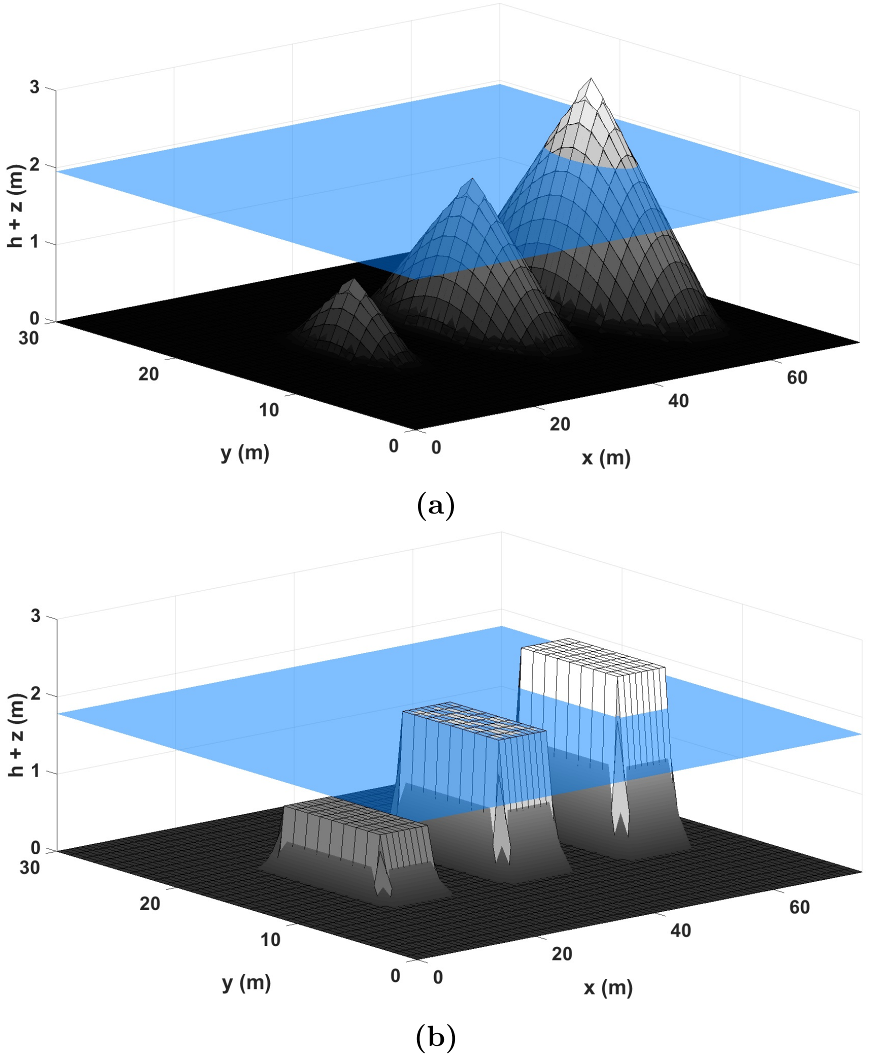

(a)

(b)

Figure 3.6: *The initial water surface and full planar DG2 topography projections* ($z_h(x,y)|_{Q_c}$)*, via Eq. 3.29a, of: (a) differential topography (Eq. 3.36) and (b) non-differential topography (Eq. 3.37).*

over non-flat topography.

Well-balanced property

The first numerical test intends to diagnostically investigate the effects of the different DG2 based bed slope terms discretisation, i.e. Eqs. 3.29 *vs.* Eqs. 3.30, on the reliability of the simplified DG2 solver in numerically preserving the well-balanced property over uneven terrain with wetting and/or drying. The test assumes a motionless flow in a 75 m × 30 m domain. Two cases are investigated to distinguish between differential and non-differential topography shapes, which resemble real-world natural and artificial terrain features. The differential topography represents a hilly terrain and consists of three mounds with different peak heights. In such case, the topography function is:

$$z(x,y) = max\left[0, 1-\frac{1}{5}\sqrt{(x-20)^2+(y-15)^2}, 2-\frac{1}{2}\sqrt{(x-40)^2+(y-15)^2}, 3-\frac{3}{10}\sqrt{(x-60)^2+(y-15)^2}\right] \tag{3.36}$$

Alternatively, the non-differential topography resembles buildings of varying heights and consists of three rectangular blocks. In this other case, the topography function is:

$$z(x,y) = \begin{cases} 0.86, & \text{if} \quad 16 \le x \le 24, 11 \le y \le 19 \\ 1.78, & \text{if} \quad 36 \le x \le 44, 11 \le y \le 19 \\ 2.30, & \text{if} \quad 56 \le x \le 64, 11 \le y \le 19 \\ 0, & \text{otherwise} \end{cases} \tag{3.37}$$

Figs. 3.6a and 3.6b provide a view on the 2D local planar DG2 projections, via Eq. 3.29a, for the topography functions Eq. 3.36 and Eq. 3.37, respectively. In both cases, the choice for the initial free-surface elevation is taken according to three scenarios: fully submerged ($h > 0$ m at one peak), critically wet ($h = 0$ m at another peak) and partially wet involving wet-dry fronts ($h \le 0$ m, in the sense where the local planar DG2 solutions cut through the highest peak). This leads to set a free-surface elevation value of 1.78 m and 1.95 m for the first and second cases, respectively (see also Fig. 3.6) together with zero discharge values for q_x and q_y. These initial states should be maintained as there is no external force exerted on the flow at any of the boundaries. To study the numerical well-balancedness of the simplified DG2 solver, the domain is discretised using 1 m^2 grids, and simulations are run for relatively long time evolution ($t = 100$ s) considering transmissive numerical boundary conditions. To conduct a thorough analysis of the well-balanced property, the time histories of the maximum errors are calculated (for each simulation) for all the discharge coefficients spanning the local DG2 solutions (namely the mean coefficients q_x^0 and q_y^0, the x-directional slope coefficients q_x^{1x} and q_y^{1x}, and the y-directional slope coefficients q_x^{1y} and q_y^{1y}). These errors are plotted and analysed to explore the well-balanced property at the level of both the mean and the slope coefficients.

Simulation results relative to the first case are summarised in Fig. 3.7, which shows the time histories of the errors for the mean and slope (discharge) coefficients up to $t = 100$ s, with a time step, Δt, of approximately 0.08 s. In particular, Fig. 3.7a shows the results considering the bed slope discretisation in Eqs. 3.29. At the start of the simulation ($t < 7$ s), the mean coefficients q_x^0 and q_y^0 are within the round off error even in the presence of wet-dry fronts. This finding reinforces the well-balancedness validation statement in Appendix A, according to which the solver should be well-balanced for the mean coefficients with both bed slope term discretisations Eqs. 3.29 and Eqs. 3.30. In Fig. 3.7a, similar behaviour can also be observed for the discharge slope coefficients relative to the mainstream directions, q_x^{1x} and q_y^{1y}. However, the discharge slope coefficients across the opposite direction, q_x^{1y} and q_y^{1x}, display a different behaviour, showing a drastic rise in error magnitudes from the very start of the simulation. Although this rise seems to settle quite soon ($t > 17$ s), it appears to produce numerical artefacts, which gradually (for $t > 7$s) affect the other discharge coefficients that were initially well-balanced (for $t < 7$s). From $t = 17$ s onward, relatively mild perturbations are observed for all discharge coefficients, which seems to suggest that Eqs. 3.29 do not provide a fully well-balanced simplified DG2 solver. In contrast, by re-running the simulation

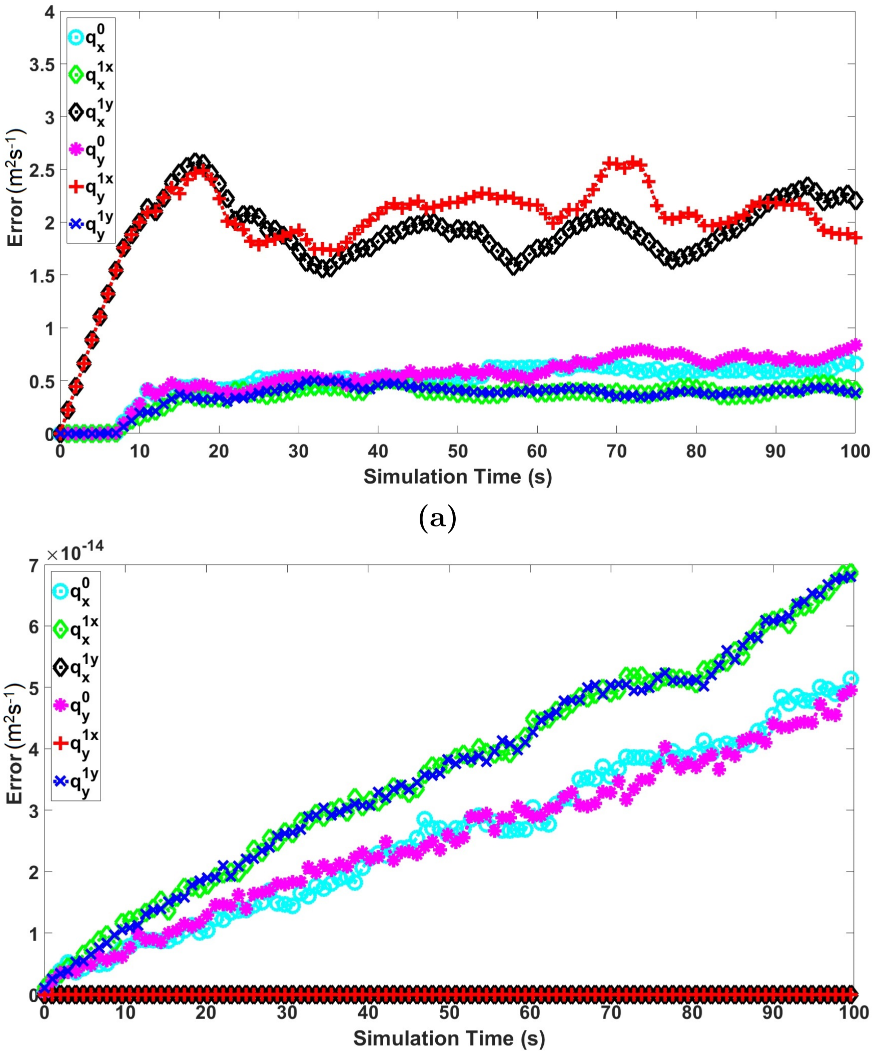

(a)

(b)

Figure 3.7: *Time histories of the resulting maximum errors for the mean and slope discharge coefficients over a differential topography (case 1) using the (a) original discretisation Eqs. 3.29 and (b) alternative discretisation Eqs. 3.30.*

using the proposed alternative topography discretisation, via Eqs. 3.30, more consistent error magnitudes are obtained as shown in Fig. 3.7b. In this setting, it can be noticed that the variation of all discharge coefficient errors remains substantially bounded within the range of the round-off throughout the simulation.

In the second case, where the topography function is not differentiable, the adverse effects of the choice of the bed slope discretisation of Eqs. 3.29 are observed to augment as seen in Fig. 3.8a. The resulting time histories for the discharge coefficient (maximum) errors again imply a partially well-balanced behaviour up to certain time around $t = 13$ s, i.e. for the mean coefficients, q_x^0 and q_y^0, and the slope coefficients relative to the mainstream directions, q_x^{1x} and q_y^{1y}. However, the errors produced for the cross-directional slope coefficients, q_x^{1y} and q_y^{1x}, are now seen to exhibit a much higher increase up to eight times larger than those observed in the first case (compare Fig. 3.7a to Fig. 3.8a). These errors continue to rise until $t = 13$ s when they reduce and become relatively stable. They also show a behaviour similar to the first case, in that they eventually (13 s $< t <$ 100 s) affect the errors of the other discharge coefficients, which were initially well-balanced (0 s $< t <$ 13 s). These findings seem to suggest that any unbalance in a slope coefficient, if overlooked, can gradually affect the well-balanced property for all other coefficients, and hence eventually that of the full DG2 planar solutions. In contrast, by using the proposed choice for the bed slope term discretisation, via Eqs. 3.30, in combination with the simplified DG2 solver all error magnitudes remain bounded near the range of machine precision, as shown in Fig. 3.8b, irrespective of the discontinuous character of the topographies involved in this case. These results imply that all mean and slope coefficients for the discharge remain numerically well-balanced in this setting. Hence, one can conclude that the simplified DG2 solver complemented with Eqs. 3.30 for the bed slope discretisations is fully well-balanced for both mean and slope coefficients in all three scenarios.

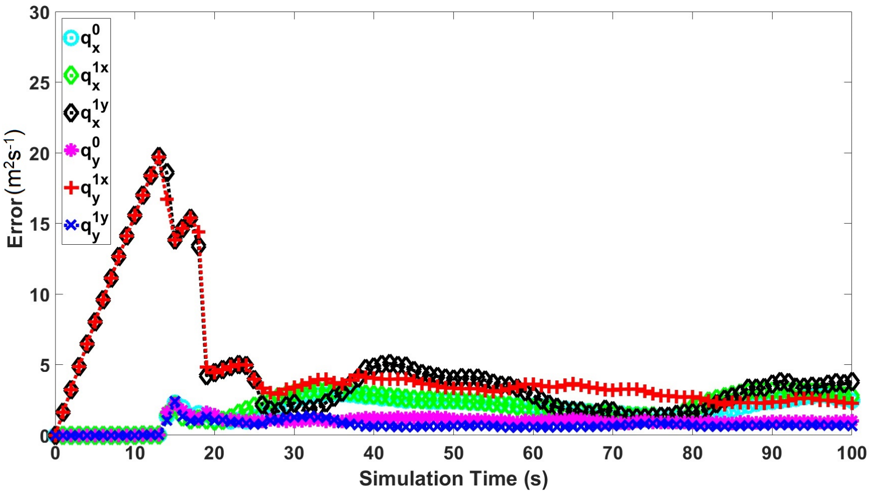

(a)

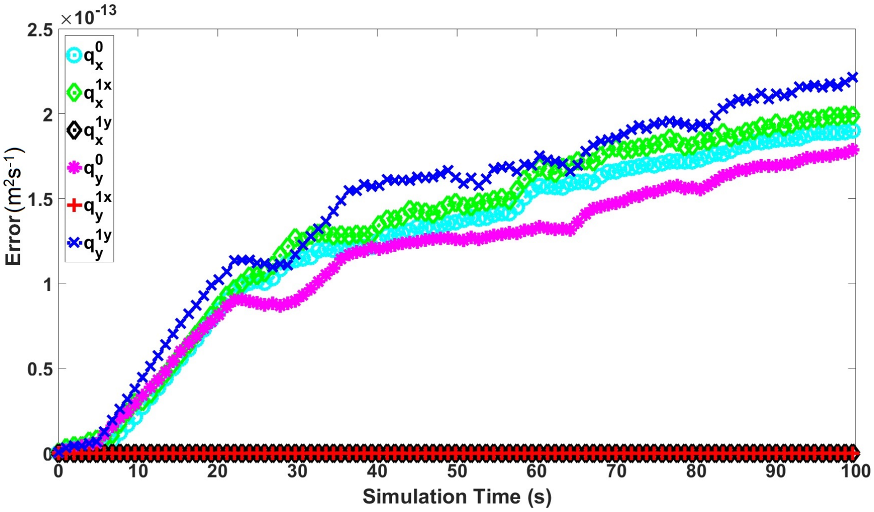

(b)

Figure 3.8: *Time histories of the resulting maximum errors for the mean and slope discharge coefficients over a non-differential topography (case 2) using the (a) original discretisation Eqs. 3.29 and (b) alternative discretisation Eqs. 3.30.*

Accuracy order

Having verified that the simplified DG2 solver with Eqs. 3.30 is well-balanced, further assessments are made to test the conservative features of this solver. In particular, the numerical accuracy of the solver is verified for a transient flow case involving moving 2D wet-dry fronts over a non-flat topography. This numerical test relies upon the well-known 2D oscillatory flow in a parabolic bowl problem (Bunya et al. 2009), in which a set of parametric values are used following Ern et al. (2008). The model is set in a 2D domain of square length $[-4000\text{m}, +4000\text{m}]^2$. The topography is defined as $z(x,y) = \alpha r^2$, where α is a constant equal to 1.610^{-7} m^{-1} and r is the radial distance with $r^2 = \sqrt{x^2+y^2}$. The initial velocities, $u(x,y,0)$ and $v(x,y,0)$, are set to zero, and the initial free surface elevation is $h(r,0) = (1+a(Y-X)r^2)/(X+Y)$, where X and Y are equal to 1 m^{-1} and -0.41884 m^{-1}, respectively. The wet domain is defined such that $h(r,t) > 0$ for $r < \sqrt{(X+Ycos\omega t)/\alpha(X^2-Y^2)}$, which can be used to identify the interface between the wet and dry regions. This numerical test assumes a period of $\tau = 2\pi/\omega$ equivalent to 1,756.2 s with $\omega^2 = 8g\alpha$. There is no specific boundary condition to be prescribed, as the free surface does not reach the domain boundary. The analytical solution is given in Thacker (1981):

$$h(r,t) = \frac{1}{X+Ycos\omega t} + \alpha(Y^2-X^2)\frac{r^2}{(X+Ycos\omega t)^2} \tag{3.38}$$

$$(u(x,y,t), v(x,y,t)) = -\frac{Y\omega sin\omega t}{(X+Ycos\omega t)}\left(\frac{x}{2},\frac{y}{2}\right) \tag{3.39}$$

Figs. 3.9 and 3.10 contain the plots of the computed free surface elevation and discharges, respectively, using similar grid resolutions and display patterns as in Bunya et al. (2009). These figures allow to compare the mean coefficients (or average values) calculated by the simplified DG2 solver (across the centreline $x = 0$) with the exact solution for two grid resolutions (i.e. $\Delta x = 100$ and 200, with $\Delta x = \Delta y$) at the six output times $t = 0$, $\tau/6$, $2\tau/6$, $3\tau/6$, $4\tau/6$, $5\tau/6$ and τ. In the prediction of the free surface elevation, as shown in Fig. 3.9, the simplified DG2 solver is observed to perform very well, yielding calculations that are in

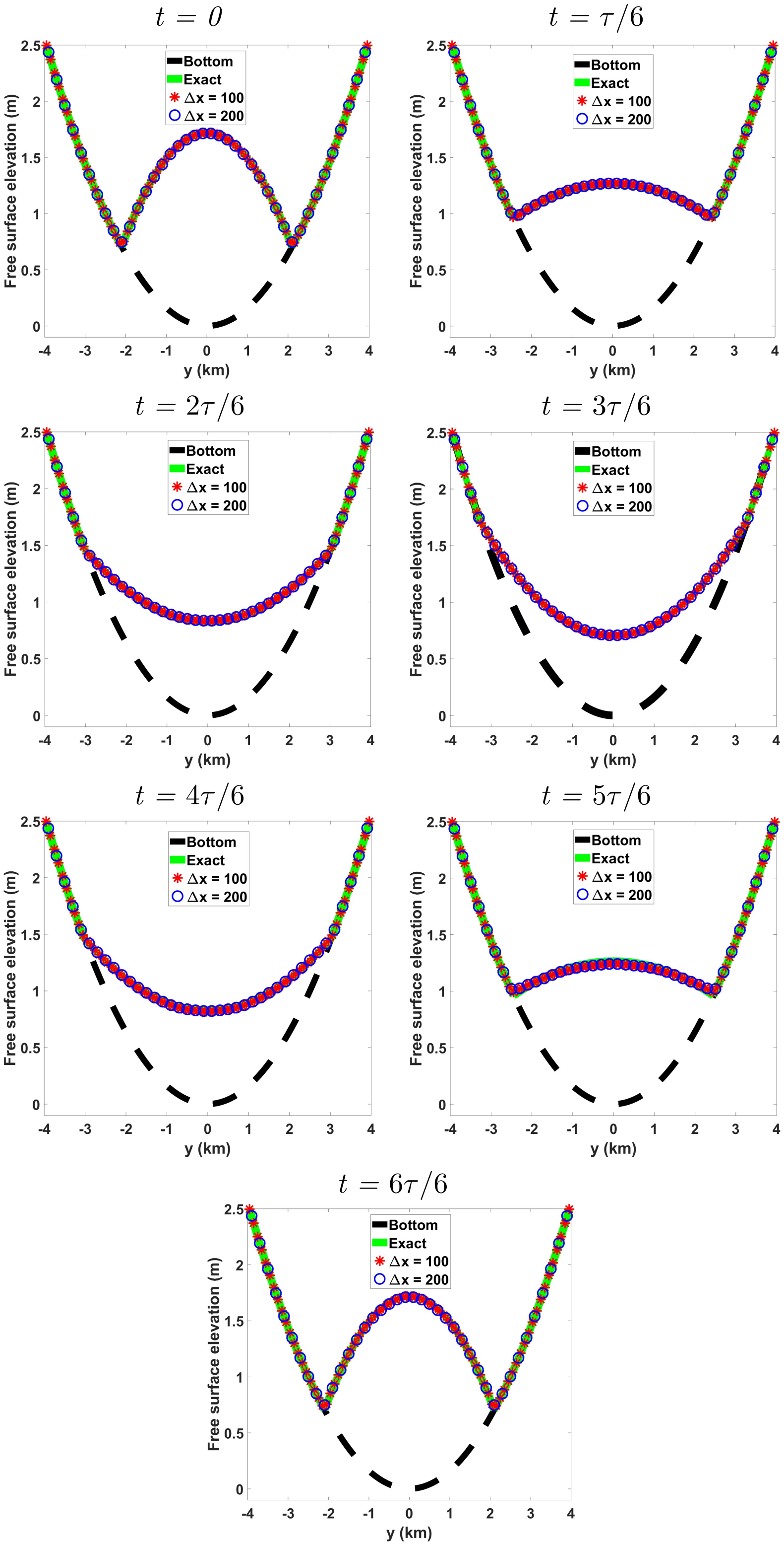

Figure 3.9: *Free surface elevation sliced along x = 0 km at six output times considering two grid resolutions with size Δx = 100 m and 200 m.*

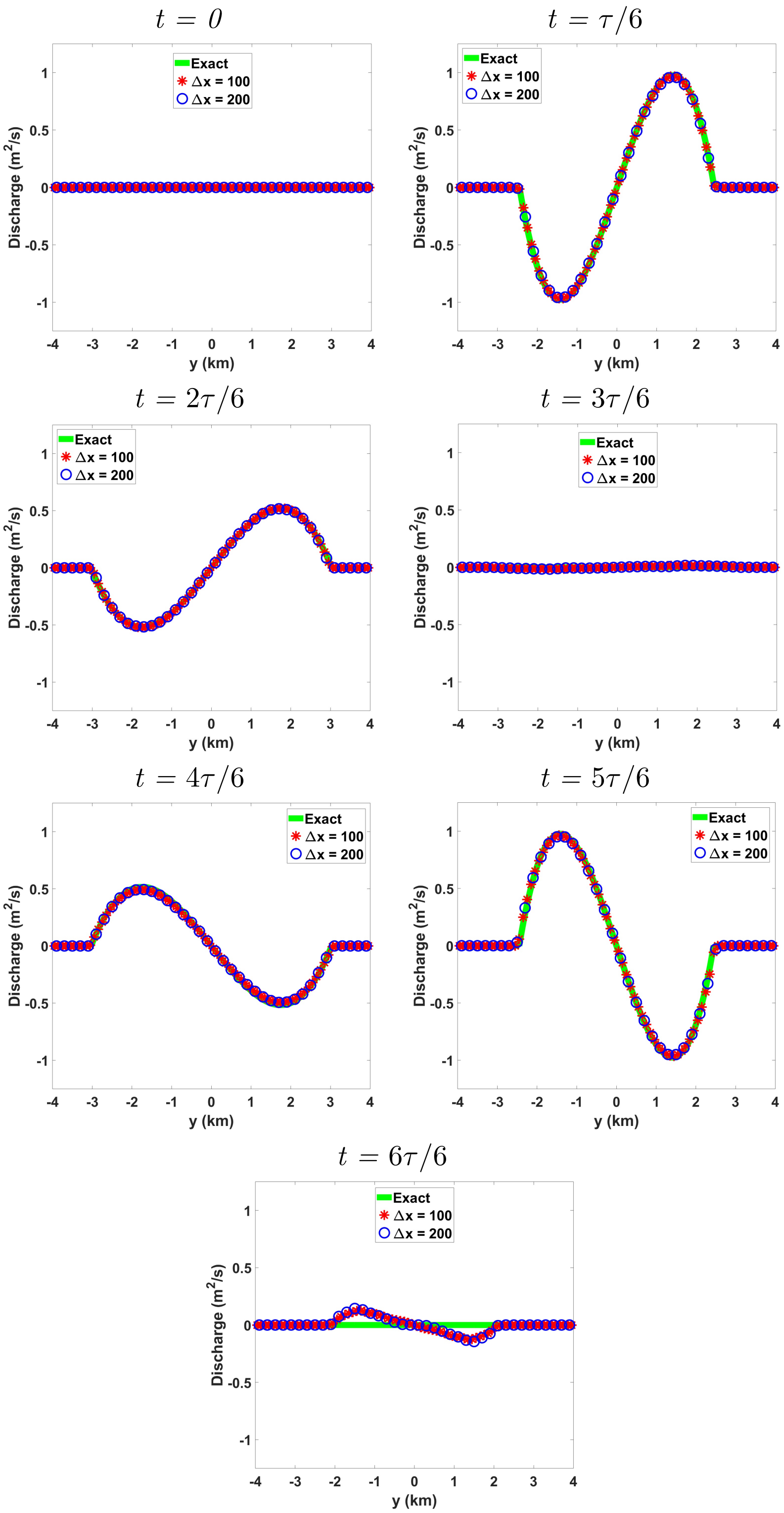

$t = 0$

$t = \tau/6$

$t = 2\tau/6$

$t = 3\tau/6$

$t = 4\tau/6$

$t = 5\tau/6$

$t = 6\tau/6$

Figure 3.10: *Discharges sliced along* $x = 0$ *km at six output times considering two grid resolutions with size* $\Delta x = 100$ *m and 200 m.*

Table 3.2: *L^1-norm, L^2-norm and L^∞-norm errors and orders of accuracy for the 2D parabolic bowl test: analysis for the water depth, h, at $t = \tau/2$ (wetting stage).*

Δx	L^1-error	L^1-order	L^2-error	L^2-order	L^∞-error	L^∞-order
400.0	$4.60e^{-03}$	-	$4.70e^{-03}$	-	$5.80e^{-03}$	-
200.0	$1.10e^{-}03$	2.031	$1.20e^{-03}$	2.000	$1.40e - 03$	2.014
100.0	$2.77e^{-04}$	2.021	$2.92e^{-04}$	2.011	$4.33e^{-04}$	1.740
50.0	$6.70e^{-05}$	2.048	$7.08e^{-05}$	2.044	$1.02e^{-04}$	2.085
25.0	$1.56e^{-05}$	2.100	$1.67e^{-}05$	2.085	$3.80e^{-05}$	1.426
12.5	$3.39e^{-06}$	2.207	$3.82e^{-06}$	2.129	$1.32e^{-05}$	1.522

Table 3.3: *L^1-norm, L^2-norm and L^∞-norm errors and orders of accuracy for the 2D parabolic bowl test: analysis for y-direction discharge, q_y, at $t = \tau/2$ (wetting stage).*

Δx	L^1-error	L^1-order	L^2-error	L^2-order	L^∞-error	L^∞-order
400.0	$3.76e^{-02}$	-	$4.58e^{-02}$	-	$7.42e^{-02}$	-
200.0	$7.30e^{-03}$	2.372	$8.20e^{-03}$	2.484	$1.36e^{-02}$	2.447
100.0	$1.60e^{-03}$	2.215	$1.70e^{-03}$	2.266	$3.10e^{-03}$	2.138
50.0	$1.89e^{-04}$	3.052	$2.25e^{-04}$	2.919	$4.70e^{-04}$	2.718
25.0	$7.47e^{-05}$	1.338	$8.97e^{-05}$	1.326	$2.37e^{-04}$	0.986
12.5	$4.18e^{-05}$	0.837	$5.06e^{-05}$	0.827	$1.11e^{-04}$	1.096

good agreement with the exact solutions for all the output times considered, and irrespective of the grid resolutions. Fig. 3.10 shows that, in terms of discharge predictability, the solver is also observed to closely follow the exact profiles for both grids and at almost all output times, except at $t = \tau$ when the numerical solutions do not fully capture the zero discharge, which is a common deficiency for this test (Kesserwani & Wang 2014, Ern et al. 2008, Bunya et al. 2009). Generally, these results reveal that the simplified DG2 solver can capture very well the flow features with curvature and persistent wetting and drying.

To gain further insights on the grid convergence (as in Sec. 3.3.1), analyses considering L^1-, L^2- and L^∞-norm errors and their relative orders were performed using the sliced profiles of the depth and discharge (in Figs. 3.9 and 3.10) on six grid resolutions (i.e. with $\Delta x =$ 12.5, 25, 50, 100, 200 and 400, respectively). The analyses are done at the times $t = \tau/2$ and τ, which represent a wetting stage and a drying stage, respectively. Results of the analyses are presented in Tables 3.2 to 3.5.

Table 3.4: *L^1-norm, L^2-norm and L^∞-norm errors and orders of accuracy for the 2D parabolic bowl test: analysis for the water depth, h, at $t = \tau$ (drying stage).*

Δx	L^1-error	L^1-order	L^2-error	L^2-order	L^∞-error	L^∞-order
400.0	$7.30e^{-03}$	-	$7.03e^{-03}$	-	$9.40e^{-03}$	-
200.0	$1.80e^{-03}$	2.022	$1.80e^{-03}$	2.009	$2.30e^{-03}$	2.009
100.0	$4.39e^{-04}$	2.029	$4.59e^{-04}$	1.982	$5.93e^{-04}$	1.978
50.0	$1.07e^{-}04$	2.035	$1.12e^{-04}$	2.039	$1.50e^{-04}$	1.988
25.0	$2.69e^{-05}$	1.995	$2.70e^{-05}$	2.048	$3.68e^{-05}$	2.024
12.5	$7.69e^{-06}$	1.806	$7.00e^{-06}$	1.947	$9.51e^{-06}$	1.951

For the water depth, as shown in Tables 3.2 and 3.4, the acquired order-of-accuracy are consistently very close to second-order for all the grid resolutions considering L^1- and L^2-orders. Although a drop in the L^∞-orders (to around 1.5) is noted at $t = \tau/2$ (Table 3.2) on the finer grids, L^∞-orders at $t = \tau$ (Table 3.4) remain consistently second-order. For the y-direction discharges, the results in Tables 3.3 and 3.5 show alternating order-of-accuracy in the range of 0.8–3.0 at $t = \tau/2$ (Table 3.3), and of 1.2–2.0 at $t = \tau$ (Table 3.5). Excluding the results associated with two finer grids in Tables 3.3 and 3.5, all L^1-, L^2- and L^∞-orders indicate second-order accurate predictions for the discharges. In contrast, for the two finer grids, the drop in L^1-, L^2- and L^∞-orders to less than 1.5 are most likely caused by the aforementioned deficiency in predicting the zero discharges occurring at $t = \tau/2$ and $t = \tau$ (see Fig. 3.10). Nonetheless, these results reveal that the simplified DG2 solver has a good tendency to deliver second-order accurate simulations of fully 2D nonlinear shallow water flows over uneven topography with constant wetting and drying, in addition to being formally a second-order accurate solver as shown in the previous analysis in Table 3.1 (Sec. 3.3.1).

3.4 Concluding remarks

In this chapter, the conceptual formulation of a DG2 numerical solver to the 2D-SWE on grid elements have been presented. The derivation of the proposed 2D-SWE DG2 solver considered the standard formulation (i.e. based on the stencil in Fig. 3.1) as a starting point, which was then simplified to produce the so-called slope-decoupled formulation (i.e. based

Table 3.5: *L^1-norm, L^2-norm and L^∞-norm errors and orders of accuracy for the 2D parabolic bowl test: analysis for y-direction discharge, q_y, at $t = \tau$ (drying stage).*

Δx	L^1-error	L^1-order	L^2-error	L^2-order	L^∞-error	L^∞-order
400.0	$3.44e^{-02}$	-	$3.60e^{-02}$	-	$4.58e^{-02}$	-
200.0	$8.90e^{-03}$	1.951	$9.40e^{-03}$	1.929	$1.27e^{-02}$	1.855
100.0	$2.40e^{-03}$	1.901	$2.60e^{-03}$	1.860	$3.80e^{-03}$	1.717
50.0	$6.90e^{-04}$	1.787	$8.00e^{-04}$	1.702	$1.30e^{-03}$	1.621
25.0	$2.65e^{-04}$	1.382	$3.24e^{-04}$	1.302	$4.67e^{-04}$	1.424
12.5	$1.03e^{-04}$	1.366	$1.34e^{-04}$	1.276	$2.04e^{-04}$	1.191

on the stencil in Fig. 3.2). In the simplified DG2 formulation, theoretical complexity was deliberately compromised to acquire a setting whereby key challenges relevant to the practical modelling of hydrodynamics are conveniently addressable (i.e. well-balancing between spatial flux and steep topography gradients, robust incorporation of wetting and drying processes, and reduction of operational costs). The well-balanced property of the simplified DG2 solver was extensively studied for two possible approaches to discretise the bed slope terms, following a consistent manner based on the local DG2 discrete planar projection to the topography. The first approach, via Eqs. 3.29, involves both x- and y-directional bed slope coefficients as full contribution for the planar topography projections. In the second approach, via Eqs. 3.30, any possible cross-dimensional bed slope dependency was zeroed to keep consistent with the slope-decoupled formulation adopted for the simplified 2D-SWE DG2 solver. It was theoretically demonstrated that the simplified DG2 solver can only be partially well-balanced (i.e. for the means and some slope coefficients) with the first approach for integrating DG2 topography projections. In contrast, when complemented with the second approach, the simplified DG2 solver is fully well-balanced (i.e. for all the coefficients spanning the DG2 solutions). Selected numerical tests were employed to verify the applicability of the simplified DG2 solver, considering the comparison in the performance to the standard DG2 solver, and the verification of its conservative abilities relating to the 2D shallow water modelling.

When comparing the performance of the two DG2 solvers, the simplified DG2 solver is able to achieve second-order grid convergence and close predictive capability as the standard DG2 solver. Further numerical verifications revealed a fully well-balanced behaviour of the simplified DG2 solver with the combination of the second DG2 bed slope projection approach, even when the topography admits non-differentiable shapes (e.g. building like) and/or when the domain is partially dry (e.g. when the local planar DG2 flow solution cut through the local planar topography projection). Moreover, the solver could preserve its second-order grid convergence when the flow involves cyclic movement of wet-dry fronts over an uneven topography, and show a remarkable capability in simulating realistic features associated with 2D modelling of hydrodynamics (i.e. wetting and drying processes, flow over irregular terrain and flow curvatures). It can therefore be concluded that the simplified 2D-SWE DG2 solver is a valid option to develop a flood model with desirable robustness properties to simulate real-world practical applications.

Chapter 4

Performance against industry-standard FV-based flood models

Contents used to prepare for this chapter have been published in the following publication:

Ayog, J. L., Kesserwani, G., Shaw, J., Sharifian, M. K., Bau, D. 2021. Second-order discontinuous Galerkin flood model: Comparison with industry-standard finite volume models, J. Hydrol. 593 125924. https://doi.org/10.1016/j.jhydrol.2020.125924

4.1 Chapter overview

This chapter, which seeks to address Objective 2 and part of Objective 3, centred around a new flood model that has been developed using the simplified 2D-SWE DG2 solver described in Chapter 3. This DG2 flood model is analysed considering two possible variants of this DG2 solver: with (DG2-LL) and without local slope limiting (DG2-NL), to uncover its potential and identify its best possible setting in modelling flow features relevant to flood inundation (Objective 3). The analyses are made through comparative benchmarking against industry-standard FV1- and FV2-based flood models (Objective 2). Sec. 4.2. discusses the methodological similarities and differences between the DG2 and FV-based solvers, and then the mass and energy conservation properties of the solvers over time are numerically assessed. The performance of the DG2 model considering the two variants are further assessed in Sec. 4.3 against the outputs of four industry-standard FV-based flood models at similar resolution, as well as the outputs of the best performer DG2 variant and the MUSCL-FV2 solver at twice-coarser resolution. The comparisons include qualitative and quantitative analyses on the water level and/or velocity histories (Sec. 4.3) along with their respective computational runtimes (Sec. 4.4). Finally, Sec. 4.5 concludes by identifying when a DG2-based flood model could add value to support industrial-scale flood modelling, and which DG2 variant is the most appropriate in relation to the intended modelling study.

4.2 Grid-based flood models

The simplified DG2 solver, which is developed based on the slope-decoupled formulation, has been designed to provide well-balanced piecewise-planar solutions on a simplified stencil compatible with that of existing grid-based FV flood models. This DG2 solver has been demonstrated, earlier in Chapter 2, to reduce the runtime cost per element by 2.6 times compared to a standard DG2 solver while preserving second-order accuracy. In this study, the simplified DG2 solver is further optimised to make it suitable for practical 2D flood inundation modelling. A MUSCL-FV2 alternative is also presented and its main differences and similarities to the DG2 solver are discussed. Later, the conservation properties of both DG2 and MUSCL-FV2 solvers are then analysed through a synthetic test case involving nonlinear flow with periodic wetting and drying cycles over an uneven topography.

4.2.1 DG2 solver

Local piecewise-planar solutions

As shown in Chapter 2, the simplified DG2 solver uses local piecewise-planar approximate solutions, $\mathbf{U_h}$, to the flow vector $\mathbf{U}$. Over each grid element Q_c, $\mathbf{U_h}$ is expanded by coefficients representing a mean, $\mathbf{U}_c^0$, and two slopes on the Cartesian directions, $\mathbf{U}_c^{1x}$ and $\mathbf{U}_c^{1y}$, as follows:

$$\mathbf{U_h}(x,y,t)|_{Q_c} = \mathbf{U}_c^0(t) + \frac{(x-x_c)}{\Delta x/2}\mathbf{U}_c^{1x}(t) + \frac{(y-y_c)}{\Delta y/2}\mathbf{U}_c^{1y}(t) \tag{4.1}$$

The mean and slope coefficients are initialised from a given initial condition, $\mathbf{U}_0(x,y,t)$, such that:

$$\mathbf{U}_c^0(0) = \frac{1}{2}[\mathbf{U}_0(E) + \mathbf{U}_0(W)] = \frac{1}{2}[\mathbf{U}_0(N) + \mathbf{U}_0(S)] \tag{4.2a}$$

$$\mathbf{U}_c^{1x}(0) = \frac{1}{2}[\mathbf{U}_0(E) - \mathbf{U}_0(W)] \tag{4.2b}$$

$$\mathbf{U}_c^{1y}(0) = \frac{1}{2}[\mathbf{U}_0(N) - \mathbf{U}_0(S)] \tag{4.2c}$$

where $\mathbf{U}_0(p)$, with $p = E$, W, N and S, are the initial condition values at the face-centred nodes (see Fig. 3.2, Chapter 2), which are averaged earlier from the values at the grid element corner nodes (Eqs. 3.24 - 3.26, Chapter 2). The time-invariant topography coefficients, z_c^0, z_c^{1x} and z_c^{1y}, which represent the piecewise-planar topography approximations, $z_h(x,y)$, are initialised in a similar approach to Eq. 4.2 with the values at the corner nodes representing the data points extracted from a Digital Elevation Model (DEM).

Well-balanced and depth-positivity preserving DG2 operators

In an explicit second-order Runge-Kutta (RK2) time integration (Eq. 3.15, Chapter 2), with a maximum CFL = 0.3 (Cockburn & Shu 2001), the DG2 coefficients considering the flow vector, $\mathbf{U}_c^K(t)$, are updated using the spatial operators $\mathbf{L}_c^K$ $(K = 0, 1x, 1y)$. These spatial DG2 operators (see Eqs. 3.21, Chapter 2) – after algebraic manipulations and zeroing cross-dimensional bed-slope dependencies (see Appendix A) – can be reduced to read:

$$\mathbf{L}_c^0 = -\frac{1}{\Delta x}(\widetilde{\mathbf{F}}_E - \widetilde{\mathbf{F}}_W) - \frac{1}{\Delta y}(\widetilde{\mathbf{G}}_N - \widetilde{\mathbf{G}}_S) + 2g\begin{bmatrix} 0 \\ \frac{\bar{h}_c^0 \bar{z}_c^{1x}}{\Delta x} \\ \frac{\bar{h}_c^0 \bar{z}_c^{1y}}{\Delta y} \end{bmatrix} \tag{4.3a}$$

$$\mathbf{L}_c^{1x} = -\frac{3}{\Delta x}\left\{ \left(\widetilde{\mathbf{F}}_E + \widetilde{\mathbf{F}}_W\right) - \left(\mathbf{F}\left(\mathbf{U}_c^0(t) + \frac{1}{\sqrt{3}}\mathbf{U}_c^{1x}(t)\right) + \mathbf{F}\left(\mathbf{U}_c^0(t) - \frac{1}{\sqrt{3}}\mathbf{U}_c^{1x}(t)\right)\right) + \frac{2g}{\sqrt{3}}\begin{bmatrix} 0 \\ \bar{h}_c^{1x}\bar{z}_c^{1x} \\ 0 \end{bmatrix} \right\} \tag{4.3b}$$

$$\mathbf{L}_c^{1y} = -\frac{3}{\Delta y}\left\{ \left(\widetilde{\mathbf{G}}_N + \widetilde{\mathbf{G}}_S\right) - \left(\mathbf{G}\left(\mathbf{U}_c^0(t) + \frac{1}{\sqrt{3}}\mathbf{U}_c^{1y}(t)\right) + \mathbf{G}\left(\mathbf{U}_c^0(t) - \frac{1}{\sqrt{3}}\mathbf{U}_c^{1y}(t)\right)\right) + \frac{2g}{\sqrt{3}}\begin{bmatrix} 0 \\ 0 \\ \bar{h}_c^{1y}\bar{z}_c^{1y} \end{bmatrix} \right\} \tag{4.3c}$$

Note that the friction effects are excluded from the spatial operators in Eq. 4.3 as they are added separately. The terms $\tilde{\mathbf{F}}_E$, $\tilde{\mathbf{F}}_W$, $\tilde{\mathbf{G}}_N$ and $\tilde{\mathbf{G}}_S$ are the inter-elemental fluxes evaluated from the limits of the piecewise-planar approximate solutions at either side of the face-centred nodes $p = E, W, N$ and S (Fig. 3.2) after applying appropriate revisions to preserve well-balancedness and depth-positivity (Liang & Marche 2009). For example, the limits at the eastern face-centred node, E, are expressed as: $\mathbf{U}_E^- = \mathbf{U}_c^0(t) + \mathbf{U}_c^{1x}(t)$ and $\mathbf{U}_E^+ = \mathbf{U}_{nei_E}^0(t) - \mathbf{U}_{nei_E}^{1x}(t)$, where $'nei_E'$ is the index of the direct neighbour from the eastern side. Both limits at E for z_h are equal, $z_E = z_h(E^{\pm})$, as Eq. 4.2 ensures the continuity property (see also Eq. 3.27, Chapter 2). Dummy limits that are depth-positivity preserving, denoted with the '*' symbol, are reconstructed for the components of the flow vector, as: $h_E^{\pm} = max(0, h_E^{\pm})$, $(hu)_E^{\pm,*} = h_E^{\pm,*}u_E^{\pm}$ and $(hv)_E^{\pm,*} = h_E^{\pm,*}v_E^{\pm}$, where $u_E^{\pm} = (hu)_E^{\pm}/h_E^{\pm}$ and $v_E^{\pm} = (hv)_E^{\pm}/h_E^{\pm}$ when $h_E^{\pm}$ is above a drying tolerance, tol_{dry}, and zeroed when $h_E^{\pm} < tol_{dry}$. A dummy revision of the continuous topography limit z_E is also applied to preserve well-balancedness when a motionless body of water is blocked by a high wall, i.e. $z_E^* = z_E - max(0, -h_E^-)$. The revised limits $\mathbf{U}_E^{\pm,*}$ are then used to evaluate $\widetilde{\mathbf{F}}_E = \widetilde{\mathbf{F}}(\mathbf{U}_E^{-,*}, \mathbf{U}_E^{+,*})$ via two-argument numerical flux function, $\widetilde{\mathbf{F}}$, based on an approximate Riemann solver. The Riemann solver of Roe is applied as it forms the basis of the flood models explored in Sec. 4.3 and it is arguably the best choice with a DG2 solver for the SWE with source terms (Kesserwani et al. 2008). The fluxes $\widetilde{\mathbf{F}}_W$, $\widetilde{\mathbf{G}}_N$ and $\widetilde{\mathbf{G}}_S$ are evaluated similarly as $\widetilde{\mathbf{F}}_E$, after reconstructing dummy flow limits ($\mathbf{U}_W^{\pm,*}$, $\mathbf{U}_N^{\pm,*}$ and $\mathbf{U}_S^{\pm,*}$) and topography limits (z_W^*, z_N^* and z_S^*). Dummy DG2 modes are then formed, appended with a 'bar', by reapplying Eq. 4.2 to the dummy nodal limits of the flow and topography, as:

$$\overline{\mathbf{U}}_c^{0x} = \frac{1}{2}(\mathbf{U}_E^{-,*} + \mathbf{U}_W^{+,*}) \tag{4.4a}$$

$$\overline{\mathbf{U}}_c^{0y} = \frac{1}{2}(\mathbf{U}_N^{-,*} + \mathbf{U}_S^{+,*}) \tag{4.4b}$$

$$\overline{\mathbf{U}}_c^{1x} = \frac{1}{2}(\mathbf{U}_E^{-,*} - \mathbf{U}_W^{+,*}) \quad \text{and} \quad \bar{z}_c^{1x} = \frac{1}{2}(z_E^* - z_W^*) \tag{4.4c}$$

$$\overline{\mathbf{U}}_c^{1y} = \frac{1}{2}(\mathbf{U}_N^{-,*} - \mathbf{U}_S^{+,*}) \quad \text{and} \quad \bar{z}_c^{1x} = \frac{1}{2}(z_N^* - z_S^*) \tag{4.4d}$$

Replacing the evaluated fluxes $\widetilde{\mathbf{F}}_E$, $\widetilde{\mathbf{F}}_W$, $\widetilde{\mathbf{G}}_N$ and $\widetilde{\mathbf{G}}_S$ alongside the positivity-preserving modes in Eq. 4.4, altogether in Eq. 4.3, lead to a well-balanced evaluations for the DG2 operators without spurious errors across wet-dry fronts located at very steep bed-slopes, as verified in Sec. 3.3.2.

Friction source term and local limiting treatments

Piecewise-planar approximate friction term integration is applied, involving the mean, $(\mathbf{S}_f)_c^0$, and the two slope coefficients, $(\mathbf{S}_f)_c^{1x}$ and $(\mathbf{S}_f)_c^{1y}$. The contribution of the friction term coefficients is added to their respective discharge coefficients prior to each RK2 step, based on a standard implicit splitting integration (Kesserwani & Liang 2010). The integration procedure is performed at the element centre (x_c, y_c) to increment the discharges in $\mathbf{U}_c^0$, whereas the evaluation at Gaussian points G_{xi} and G_{yi} (Fig. 3.2), followed by appropriate differentiation, are made to increment the discharges in $\mathbf{U}_c^{1x}$ and $\mathbf{U}_c^{1y}$.

Local limiting (LL) is applied as a separate step before each RK2 time stage, but after applying friction effects and boundary conditions. Slope limiting to coefficients $\mathbf{U}_c^{1x}$ and $\mathbf{U}_c^{1y}$ over a grid element Q_c comes into play as an FV tool in order to limit the variations of these slopes with respect to the slopes differentiated of the mean coefficients, based on a Total Variation Diminishing (TVD) slope limiter (Sweby 1984, Toro 1999). It is well known that TVD slope limiting with DG methods is only useful at the elements where the solution is about to develop shock-like gradients, otherwise, it can greatly destroy the solution or even affect overall robustness (see examples in Kesserwani & Liang (2012*b*, 2011)). With DG2 numerical solvers, LL is commonly used for which the main challenge has been to deploy a localisation procedure to identify where slope limiting is needed (Fu & Shu 2017). The *shock detector* proposed by Krivodonova et al. (2004) is selected, as it is recognised to be one of the best options available to achieve the localisation procedure (Qiu & Shu 2005). The shock detector is applied component-wise, per slope coefficient and physical component. For example, to detect if the x-directional slope component $\mathbf{U}_c^{1x}(t)$ at a grid element Q_c needs limiting, the normalised magnitude of solution discontinuities at the face-centred eastern and western nodes, $\mathbf{DS}_p$ $(p = E, W)$, need first to be calculated as:

$$\mathbf{DS}_p = \frac{|\mathbf{U}_p^+ - \mathbf{U}_p^-|}{\frac{\Delta x}{2} max(|\mathbf{U}_c^0(t) - \frac{1}{\sqrt{3}}\mathbf{U}_c^{1x}(t)|, |\mathbf{U}_c^0(t) + \frac{1}{\sqrt{3}}\mathbf{U}_c^{1x}(t)|)} \tag{4.5}$$

Then, slope limiting will only be needed for $\mathbf{U}_c^{1x}(t)$ when at least one inter-elemental discontinuity is detected, namely when $max(\mathbf{DS}_E, \mathbf{DS}_W) > 10$ (Krivodonova et al. 2004), to ensure that Eq. 4.5 will only detect strong discontinuities, i.e. of shock types. If LL is needed, the *Generalised minmod limiter* (Cockburn & Shu 2001) is then applied to limit the slope coefficient $\hat{\mathbf{U}}_c^{1x}(t)$:

$$\hat{\mathbf{U}}_c^{1x}(t) = minmod(\mathbf{U}_c^{1x}(t), \mathbf{U}_{nei_E}^{0}(t) - \mathbf{U}_c^{0}(t), \mathbf{U}_c^{0}(t) - \mathbf{U}_{nei_W}^{0}(t)) \tag{4.6}$$

Note that the limiter in Eq. 4.6 is commonly used with DG methods for LL, and that the choice of the slope limiter function is insignificant here as the limiting operation is restricted to the locality of a shock. Worth also noting that shock detection and limiting for the water depth slope component, $h_c^{1x}(t)$, is avoided, but Eqs. 4.5-4.6 are applied instead for the free surface elevation $(h_c^{1x}(t)+z_c^{1x})$ to get $(h_c^{1x}\widehat{(t) + z}_c^{1x})$ and then deduce $\hat{h}_c^{1x}(t) = (h_c^{1x}\widehat{(t) + z}_c^{1x}) - z_c^{1x}$. This ensures that the presence of topographical steps does not falsely trigger slope limiting. In a similar way, shock detection and limiting are applied to analyse the y-directional slope component $\mathbf{U}_c^{1y}$ in grid element Q_c and potentially limit it to become $\hat{\mathbf{U}}_c^{1y}$.

Regardless of slope limiting, the localisation procedure entails an overhead cost, since Eq. 4.5 needs to be applied twice for each element Q_c, and since the presence of at least one wet-dry front needs to be checked for deactivating the limiter. Otherwise Eq. 4.6 may unnecessarily replace $\mathbf{U}_c^{1x}(t)$ by a falsely amplified slope that can trigger instabilities. In this version of the DG2 flood model, dry elements are flagged only by analysing the mean coefficient of the water depth component, h_c^0, relative to a $tol_{dry} = 10^{-5}$ instead of analysing all local evaluations at the four Gaussian points (see Fig. 3.2) spanning the full piecewise-planar solution. This approach for dry element detection is consistent with the way dry elements are detected in FV-based flood models.

4.2.2 MUSCL-FV2 solver

MUSCL-FV2 and FV1 model counterparts are described for the same computational stencil used to describe the simplified DG2 flood model (Fig. 3.2), whilst adopting similar notations to map the fundamental similarities and differences among the DG2 and FV-based flood models.

Local piecewise-constant solutions

The FV-based flood models only involve piecewise-constant averaged data, $\mathbf{U}_c^0$ and z_c^0, per grid element Q_c, namely $\mathbf{U_h}(x, y, t)|_{Q_c} = \mathbf{U}_c^0(t)$ and $z_h(x, y)|_{Q_c} = z_c^0$, which is carried out with an RK2 scheme with MUSCL-FV2, and with a forward Euler scheme with FV1, with $\mathbf{L}_c^0$ expressed as:

$$\mathbf{L}_c^0 = -\frac{1}{\Delta x}(\widetilde{\mathbf{F}}_E - \widetilde{\mathbf{F}}_W) - \frac{1}{\Delta y}(\widetilde{\mathbf{G}}_N - \widetilde{\mathbf{G}}_S) - g \begin{bmatrix} 0 \\ \bar{h}_c^{0x} \bar{z}_c^{1x} \\ \bar{h}_c^{0y} \bar{z}_c^{1y} \end{bmatrix} \tag{4.7}$$

The fluxes $\widetilde{\mathbf{F}}_E$, $\widetilde{\mathbf{F}}_W$, $\widetilde{\mathbf{G}}_N$ and $\widetilde{\mathbf{G}}_S$ are evaluated after applying the MUSCL approach (Van Leer 1979) to form the solution limits at either side of the face-centred nodes p ($p = E, W, N$ and S), with a different approach to produce revised limits in order to accomodate the discontinuous nature of z_h in the FV-based flood models.

Well-balancedness and depth-positivity preserving operations

Applying the MUSCL linear reconstructions, solution limits can be evaluated at the eastern face-centred node E as:

$$\mathbf{U}_E^- = \mathbf{U}_c^0 + 0.5\nabla_c^{1x} \quad \text{and} \quad \mathbf{U}_E^+ = \mathbf{U}_{nei_E}^0 - 0.5\nabla_{nei_E}^{1x} \tag{4.8}$$

where ∇_c^{1x} is an x-directional gradient term defined as:

$$\nabla_c^{1x} = \phi\left(\frac{\mathbf{U}_c^0 - \mathbf{U}_{nei_W}^0}{\mathbf{U}_{nei_E}^0 - \mathbf{U}_c^0}\right)\left(\mathbf{U}_c^0 - \mathbf{U}_{nei_W}^0\right) \tag{4.9}$$

The symbol ϕ is a *slope limiter function* that is applied component-wise, and by setting $\phi(r) = 0$ will lead to an FV1 solver. The choice of ϕ is discussed and justified later in the next subsection. In a similar manner, the limits $\mathbf{U}_p^{\pm}$ at the other three face-centred nodes p ($p = W, N, S$) can be reconstructed. Achieving these MUSCL reconstructions for all four limits $\mathbf{U}_p^{\pm}$ in an element Q_c requires a wider calculation stencil that needs further access to

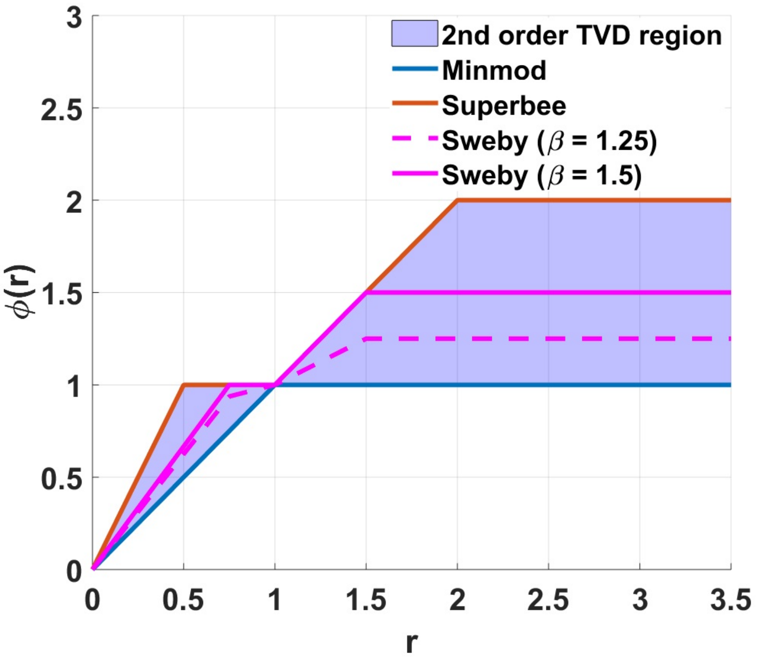

Figure 4.1: *Second-order TVD region proposed in Sweby (1984) for the choice of a valid slope limiter within a MUSCL-FV2 solver.*

the neighbour's neighbour piecewise-constant data.

In contrast to the DG2 solver, a different approach is applied to form the dummy limits $\mathbf{U}_p^{\pm,*}$ and z_p^* ($p = E, W, N$ and S), based on an intermediate involvement of the free surface elevation $h + z$. This involvement is necessary to ensure well-balancedness given the inherent involvement of the slope limiter in the FV2 solver (Liang & Marche 2009). For example, at E, the starting point is to construct two dummy topography limits $z_E^{\pm}$, via Eq. 4.8, as $z_E^{\pm} = (h + z)_E^{\pm} - h_E^{\pm}$, from which $z_E^* = max(z_E^-, z_E^+)$ is computed to ensure the continuity property. Next, dummy water depth limits $h_E^{\pm,*}$ are reconstructed as $h_E^{\pm,*} = max(0, (h + z)_E^{\pm} - z_E^*)$, through which the discharge limits become $(hu)_E^{\pm,*} = h_E^{\pm,*} u_E^{\pm}$ and $(hv)_E^{\pm,*} = h_E^{\pm,*} v_E^{\pm}$ on wet elements. The adjustment $z_E^* = z_E^* - max(0, -[(h + z)_E^- - z_E^*])$ is also applied to preserve well-balancedness when a motionless body of water is blocked by a high wall. The dummy revisions for $\overline{h}_c^{0x}, \overline{z}_c^{1x}, \overline{h}_c^{0y}$ and $\overline{z}_c^{1y}$ remain the same as in Eq. 4.4. These positivity preserving revisions are valid with Eq. 4.7 as long as the CFL number does not exceed 0.5, in order to preserve water depth-positivity over an update of each time step.

Friction source term and choice for the limiter

The friction effects are integrated by following the same procedure as the DG2 solver. It suffices to reapply the same treatment to update discharges within the FV averaged data. However, the slope limiting process is substantially different from the MUSCL-FV2 solver where the limiter function $\phi(r)$ becomes a core component to both prevent spurious oscillations near sharp solution gradients and establish second-order accuracy. The choice for $\phi(r)$ is usually made such that it is within the 2^{nd} order TVD region proposed in Sweby (1984) which is bounded by two limiters, *minmod* and *superbee*, that form the lower and upper limit respectively, as shown in Fig. 4.1. These two limiters are not practically recommended (Sanders & Bradford 2006): the *minmod* limiter does not use slope amplification and thus yields the most solution smearing, but this pays off with more stability in particular at wet-dry fronts, as the two-argument *minmod* limiter zeroes the signs of two opposite slopes. In contrast, the *superbee* limiter involves maximum slope amplifications, but it can over-amplify the slopes and cause severe instabilities at wet-dry fronts. A sensible choice for a limiter function in flood modelling is one that is strictly below the *superbee* limiter bound and is fairly higher than the *minmod* limiter bound as well. Such a choice includes the generalised *Sweby symmetric limiter* with the β parameter ranging $1 < \beta < 2$ (An & Yu 2014) and the *Barth-Jespersen limiter* (Berger et al. 2005) among many others. In this research, the *Sweby limiter* is selected subject to using $\beta = 1.25$ instead of the commonly reported value of 1.5, in order to make this limiter lower than the upper bound (Fig. 4.1). It is worth to also note that the sensitivity analysis made on the choice for β over the synthetic test case in Sec. 4.2.3 (results not shown here) indicates that the condition $\beta < 1.3$ is necessary to preserve the stability of the MUSCL-FV2 solver around wet-dry fronts.

4.2.3 Analytical assessments of solver conservation properties

The synthetic test of curved oscillatory flow in a parabolic bowl presented in Kesserwani & Wang (2014) is reconsidered, for which both MUSCL-FV2 and DG2 solvers could equally reproduce the analytical solution at grid resolutions of 2 m × 2 m and 10 m × 10 m, respec-

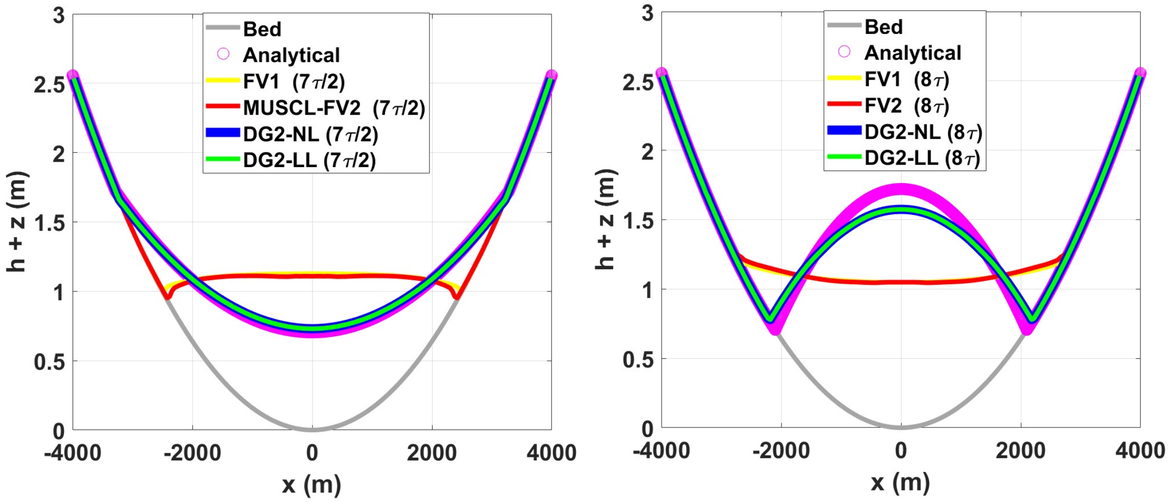

Figure 4.2: *Water level predicted by the DG2, FV2 and FV1 solvers extracted along the x-directional centreline after 7-period cycles, when the domain is: (a) maximally wet at $t = 7\tau/2$, and (b) maximally dry at $t = 8\tau$.*

tively. Both solvers have also been demonstrated to deliver second-order grid convergence when simulating only one cycle of wetting and drying, with DG2 producing better quality velocity outputs. The aforementioned test is revisited in order to explore the numerical mass and energy conservation properties of the DG2 solver compared to the FV-based solvers over much longer time evolution and for relatively coarse grid modelling. In this test and also later in Sec. 4.3, all models are run on their maximum allowable CFL number (i.e. 0.3 for DG2 and 0.5 for MUSCL-FV2).

The curved oscillatory flow test case (Thacker 1981) is applied with the same test setup used by other investigators (Bunya et al. 2009, Ern et al. 2008, Kesserwani & Wang 2014). Initially ($t = 0$ s), the discharges are zero and the water level follows a concave profile, for which the wet-dry frontline is at its narrowest extent (see analytical profile in Fig. 4.2b). This state of the flow is termed maximally dry profile and should be retrieved after a period cycle τ =1756.2 s, as the oscillatory flow runs on a frictionless domain. The opposite situation is expected to occur after half-a-period cycle, at t = $\tau/2$, leading to the maximally wet profile characterised by a convex profile for which the wet-dry frontline is at its widest extent (see analytical profile in Fig. 4.2a). A grid with a resolution of 40 m × 40 m is applied to discretise the 2D spatial domain where the DG2, MUSCL-FV2 and FV1 solvers are run up to 30-period cycles (t = 30τ). Simulation results are presented for two DG2 variants with LL (DG2-LL) and with no limiting (DG2-NL), in terms of water level predictions to the maximally dry and maximally wet profiles after 7-period cycles, as shown in Fig. 4.2.

The results in Fig. 4.2, after $t = 7\tau$, are particularly useful to examine the extent to which the DG2-LL, DG2-NL, MUSCL-FV2 and FV1 solvers are impacted by the growth of numerical diffusion, and how this impact eventually manifests within the model predictions. Both DG2-NL and DG2-LL predictions are found identical (to a numerical precision of 1×10^{-12} m) for this test, remaining close to the analytical profiles, whereas MUSCL-FV2 and FV1 solvers' predictions are relatively poorer. FV1 and MUSCL-FV2 solvers lead to a narrower wetting extent and an over-prediction of the water level in the wet zone for the maximally wet profile (Fig. 4.2a). For the maximally dry profile (Fig. 4.2b), the FV1 and MUSCL-FV2 solvers lead to a wider wetting extent and an under-prediction of water level in the wet zone.

To quantify the impact of the accumulated numerical diffusion on the conservation properties of the DG2-LL, DG2-NL, MUSCL-FV2 and FV1 solvers over the 30-period cycle ($t = 30\tau$), mass error and total energy are measured. This impact is also quantified by considering twice-finer grids (i.e. resolution of 20 m) to gain further insight into the different model response to resolution coarsening. As the flow oscillates in an enclosed system, there is an exchange between kinetic and potential energy, but the total energy should be conserved as there is no friction. The 2D domain-integrated total mass M is calculated as:

$$M(t) = \int_{+4000}^{-4000} \int_{+4000}^{-4000} h(x, y, t)\, dx dy \tag{4.10}$$

The mass error (i.e. the difference between the initial and current total mass) is calculated over time and normalised to the initial mass $M_0 = M(0)$. Also, the 2D domain-integrated

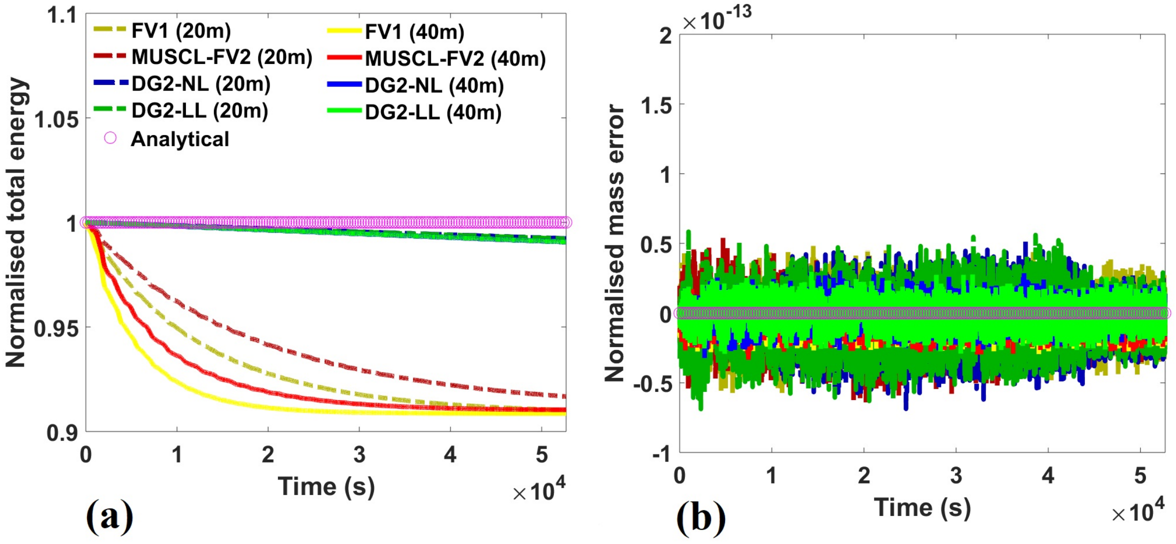

Figure 4.3: *Time histories of the 2D domain-integrated: (a) normalised total energy and (b) mass error, for the grids with a resolution of 20 m and 40 m, respectively, and over a simulation time of $t = 30\tau$.*

total energy E is calculated using the following relationship (McRae 2015):

$$M(t) = \int_{+4000}^{-4000} \int_{+4000}^{-4000} h(x,y,t) \left(\frac{1}{2} h(x,y,t)(u(x,y,t)^2 + v(x,y,t)^2) \right) + \frac{1}{2} g \left((h(x,y,t) + z(x,y))^2 - z(x,y)^2 \right) dxdy \tag{4.11}$$

and is then normalised to the initial energy $E_0 = E(0)$. While a perfectly energy-conservative solver yields 1 for the normalised total energy, a value below 1 is indicative of the impact of accumulated numerical diffusion as time evolves.

Fig. 4.3 shows the time histories of the normalised total energy and the mass errors recorded from the DG2-LL, DG2-NL, MUSCL-FV2 and FV1 outputs for two investigated grid resolutions (20 m and 40 m). As expected, the net effect of numerical diffusion in the DG2 variants, MUSCL-FV2 and FV1 solvers induces a gradual decay in the total energy (Fig. 4a). Even on the finer grid, the FV-based solvers are observed to dissipate energy quite rapidly, around 9% of the initial energy after 30 period cycles. This dissipation of initial energy is observed earlier with the coarser grid, which indicates that FV-based solvers are

Table 4.1: *List of the industrial models considered for the comparison against the DG2 models.*

Model name	Supplier	Numerical scheme	Mesh type
TUFLOW FV1	BMT-WBM	FV1 with 1st order time integration	Flexible mesh
TUFLOW FV2	BMT-WBM	MUSCL-FV2 with 2nd order time integration	Flexible mesh
TUFLOW HPC	BMT-WBM	MUSCL-FV2 with 4th order time integration	Square grid
Infoworks ICM	Innovyze	FV1 with 1st order time integration	Flexible mesh

more prone to losing energy as grid resolution is coarsened. In contrast, both DG2-LL and DG2-NL variants exhibit better energy conservation properties, with around 1% loss of the initial total energy despite grid resolution coarsening. This is because the DG2 solver evolves its local slope coefficients based on a discrete translation of the conservative model equations (Eqs. 4.3b and 4.3c) involving inter-elemental Riemann fluxes. Apart from the discrepancies observed in terms of numerical energy conservation, all models yield a zero relative mass error (Fig. 4.3b), suggesting that they are perfectly mass-conservative.

Overall, this test suggests that the DG2-NL variant can be as good as the DG2-LL when modelling (shockless) shallow water flows with wetting and drying. The DG2 solver is equally mass conservative as the FV-based solvers, but is more energy conservative due to its superior resistance to numerical dissipation. This property seems to make a DG2-based model better suited for flood inundation modelling over a long timescale and/or on coarser grids.

4.3 Comparative analyses against flood model outputs

The assessment of a flood model based on the simplified DG2 solver is made over six industrially-relevant test cases recommended by the UK Environment Agency (Neelz & Pender 2010, 2013), which have already been studied using various industrial flood models. Comparative analyses are made with respect to available outputs from four, well-established industrial FV-based flood models (Table 4.1), all adopting the Roe Riemann solver within an FV1 solver or an FV2 solver based on MUSCL linear reconstructions with TVD slope limiting (BMT-WBM 2018, Huxley et al. 2017, Innovyze 2011, Jamieson et al. 2012, Lhomme et al. 2010, Neelz & Pender 2009). The test cases have been broadly categorised as to whether the

Table 4.2: *Selected benchmark test cases with their specific parameters (Neelz & Pender 2010, 2013)*

Benchmark test cases	Finest DEM resolution (m)	Reported resolution (m)	n_M	Output time T
Gradual flood propagation				
Flooding and drying cycle over a sloping topography (Sec. 4.3.1)	2	10	0.03	20 hrs
Symmetrical flood flow propagation over a flat bed (Sec. 4.3.2)	Not available	5	0.05	300 min
Slow filling of multiple ponds (Sec. 4.3.3)	2	20	0.03	48 hrs
Rapid flood propagation				
Momentum conservation over an obstruction (Sec. 4.3.4)	2	5	0.01	900 s
Torrential flooding over a rural catchment (Sec. 4.3.5)	10	50	0.04	30 hrs
Dam break over an oblique building (Sec. 4.3.6)	0.05	0.1	0.01	120 s

flood flow propagation is gradual (Froude number < 1): covering test cases in Secs. 4.3.1 - 4.3.3, or rapid (Froude number ≤ 1): covering test cases in Secs. 4.3.4 - 4.3.6. These test cases are listed in Table 4.2 with their specific description parameters.

For each test case, DG2 model simulations are run on the same grid resolution as reported for the industrial model outputs (Table 4.2). DG2-NL and DG2-LL simulations are performed with a dual purpose: (a) to further diagnose the utility of the DG2-NL alternative for simulating flood-like flows; and (b) to uncover trade-offs related to the standard DG2-LL alternative. Between these two DG2 variants, the best performing DG2 (DG2-BP) will be selected to be rerun alongside an in-house built MUSCL-FV2 model, both on a twice-coarser grid, to also assess the different model responses to doubling the resolution. If both DG2 variants perform equally well, then DG2-NL will be selected as the DG2-BP by default.

MUSCL-FV2 simulations are also performed on the finest DEM resolution available (Table 4.2) for the first five test cases to form a reference solution, to which all flood model outputs are compared qualitatively and measured quantitatively by two statistic indices: the R-squared (R^2) coefficient, or coefficient of determination, and the L^1-norm error. These indices are evaluated for the **water level and/or velocity time histories** recorded at the sampling points specified for each test case. Their expressions are:

$$\mathrm{R}^2 = \left[\frac{\sum_{t=1}^{T} (V_t^R - \bar{V}^R)(V_t^M - \bar{V}^M)}{\sqrt{\sum_{t=1}^{T} (V_t^R - \bar{V}^R)^2 \sum_{t=1}^{T} (V_t^M - \bar{V}^M)^2}} \right]^2 \tag{4.12}$$

$$L^1\text{-norm error} = \frac{1}{N_s} \left(\sum_{t=1}^{T} \left| V_t^R - V_t^M \right| \right) \tag{4.13}$$

where t denotes the current time, T the simulation output time (Table 4.2). The values V_t^R and V_t^M refer to an entry from the reference and modelled time histories at time t, respectively; $\bar{V}^M$ and $\bar{V}^R$ represent time-averaged mean values; and N_s is the size of the time histories. The R^2 coefficient takes values between 0 and 1, indicating stronger correlation to the reference solution as it gets closer to 1. The R^2 coefficient is useful to quantify the resemblance between the predicted solution and the reference solution (e.g. similarity in hydrograph shapes), whereas the L^1-norm error provides an estimate of the average deviation of a model prediction from a reference solution (e.g. closeness of the predicted data to the reference data). Runtime costs are also analysed between MUSCL-FV2 and the DG2 variants for the same resolution of the industrial model outputs and for the grid with twice-coarser resolution (Table 4.2).

4.3.1 Flooding and drying cycle over a sloping topography

This test is often used to assess the ability of a flood model to reproduce a slow flooding and drying cycle occurring over a long duration. It involves a unidirectional flow moving over a 2D sloping topography ($n_M = 0.03$). The topography is initially dry except for a small water volume ponding near the west boundary with water level of 9.7 m (Fig. 4.4a, lower panel). The water inflow (Fig. 4.4b) at the west boundary pushes the surface flow upslope and then downslope to accumulate in the pond (Fig. 4.4a, from $x = 300$ m to $x = 700$ m). Over time, the accumulated water reaches the level 10.35 m, at which the whole topography becomes fully inundated. The water remains at this level until $t = 11$ hrs and then starts to recede

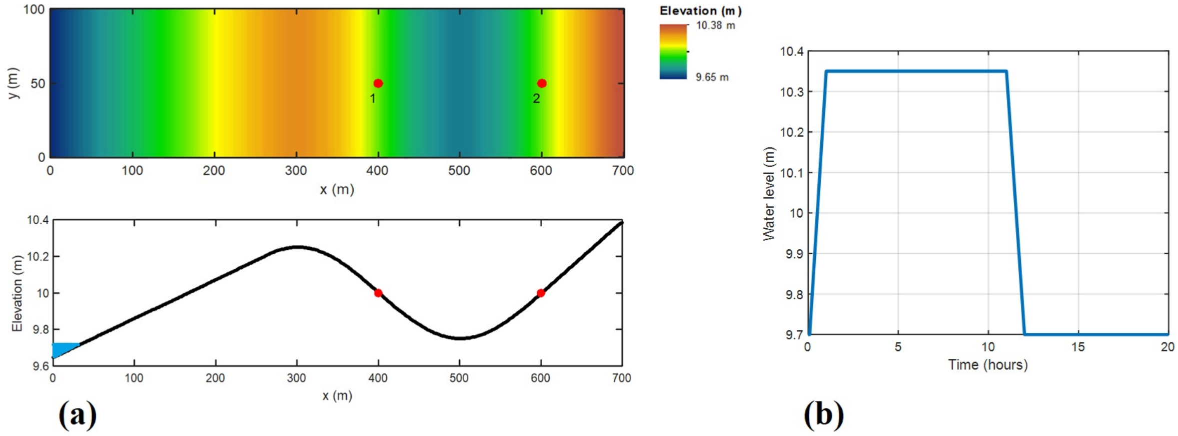

Figure 4.4: *Flooding and drying cycle over a sloping topography: (a) plan view (upper panel) and longitudinal profile (lower panel) of the topography including the location of the sampling points (red dots). Blue shaded area in the lower panel indicates initial water volume in the domain; and, (b) inflow water level hydrograph imposed at the west boundary.*

towards the west boundary. Eventually, the topography dries out except in the pond, where the water level reduces to about 10.25 m. The time histories of the water level were recorded at the two sampling points shown in Fig. 4.4, and are presented in Fig. 4.5.

In the water level time histories (Fig. 4.5), there are slight differences in all the models' predictions of the ground level at each sampling point, between $t = 0$ s to when the water level starts to rise. These differences may be attributed to the mesh types used by the models, topography discretisation approaches, and also the effects of DEM data coarsening for the 20 m grid resolution models. Nevertheless, on the grid with 10 m resolution, DG2-LL provides water level predictions that are outside the range of the water levels predicted by the industrial models. This suggests that local limiting with DG2 could still impact the DG2 flood model predictions, in particular during the flooding stage when the inflow is still feeding into the domain. In contrast, DG2-NL produces predictions that are in the range of the industrial model predictions and in closer agreement with the reference solution (at a 2 m resolution), even on a grid at 20 m resolution. The plots of the R^2 coefficient and the L^1-norm error in Fig. 4.6 confirm that DG2-NL excels in producing the most similar and the closest water level histories in relation to the reference solutions, even at 20 m resolution. DG2-LL at 10 m resolution, although providing similar shape as the reference solution, leads

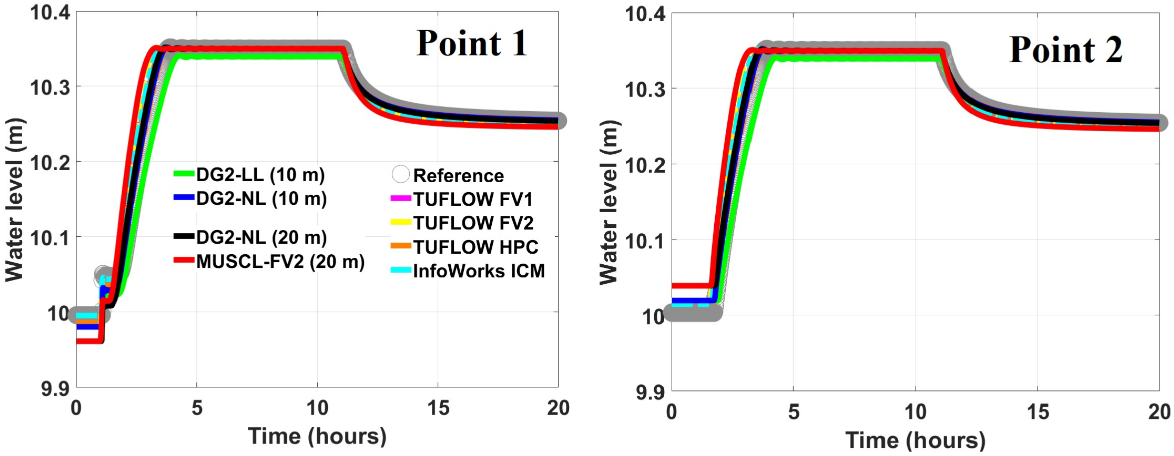

Figure 4.5: *Flooding and drying cycle over a sloping topography. Water level histories predicted by DG2-LL and DG2-NL at 10 m resolution, DG2-NL and MUSCL-FV2 models at 20 m resolution, the industrial models at 10 m resolution and the reference solution at 2 m resolution.*

to predictions that are relatively more deviated than DG2-NL at 20 m resolution. This test points out the potential of using the DG2-NL variant to model gradual flooding and drying over a long period, and reproduce the industrial model predictions at twice-as-coarse grid resolution.

4.3.2 Symmetrical flow propagation over a flat bed

This test involves a short-duration flow that gradually breaches a wall and propagates symmetrically across a rough and flat bed ($n_M = 0.05$). An inflow discharge with a peak of 20 m^3 s^{-1} (Fig. 4.7) enters the dry bed through a 20 m opening located in the middle of the west boundary. Over time, this inflow forms a fan-like 2D spread illustrated in Fig. 4.7. The history of the water level and velocity is recorded at four sampling points (Fig. 4.7), and is compared in Fig. 4.8 to those predicted by the industrial models and to the reference solution (at 2 m resolution).

The time histories in Fig. 4.8 reveal identical performance for DG2-NL and DG2-LL at 5 m resolution, and almost similar performance is observed with DG2-NL at 10 m resolution. The time histories predicted by all DG2 variants fall within the range of those made by the industrial models and show a close agreement with the reference solution. Fig. 4.9 shows

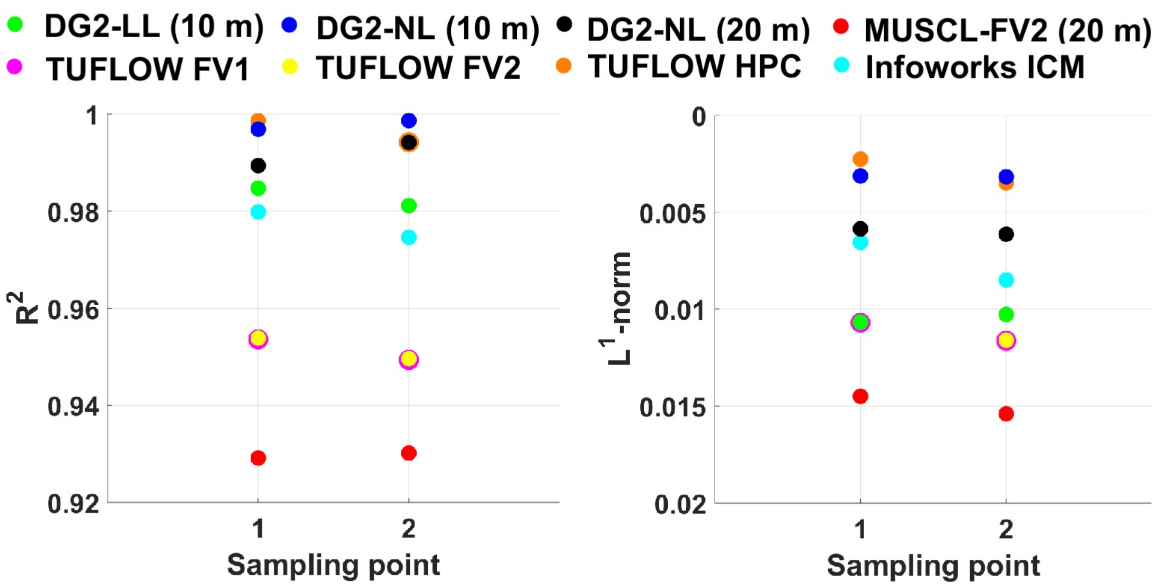

Figure 4.6: *Flooding and drying cycle over a sloping topography. Difference among the flood model predictions relative to the reference solution: R^2 coefficients (left) and L^1-norm errors (right).*

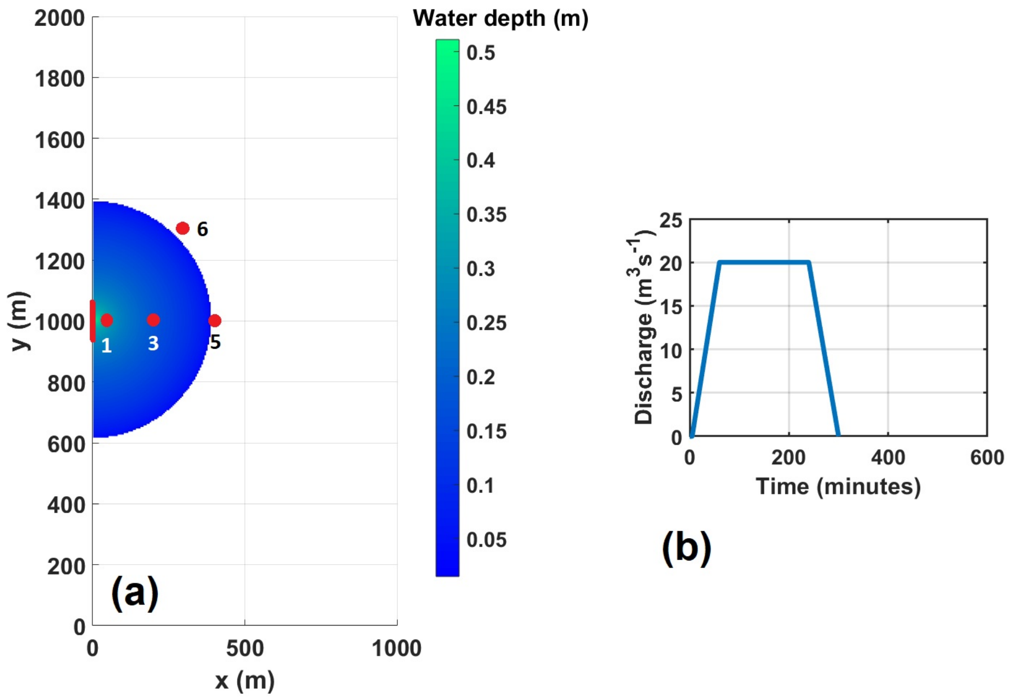

Figure 4.7: *Symmetrical flow propagation over a flat bed. Left panel shows the flood distribution at $t = 60$ min with the breach location (red line, middle of west boundary) and 4 sampling points (red dots); and, right panel shows the inflow imposed at the breach.*

that in all cases the R^2 coefficient is at least 0.93, and the L^1-norm error does not exceed 0.08, which confirms that all models in this test closely reproduce the reference solution, and with a very good overall fit. Most notably, the DG2 variants produce the least deviation at 5 m resolution, while DG2-NL at 10 m resolution can still capture the wave-front arrival more accurately than the industrial models at a 5 m resolution.

4.3.3 Slow filling of multiple ponds

This test involves a long-duration flooding over a down-sloping topography ($n_M = 0.03$) with 16 smooth ponds (Fig. 4.10). The surface slope in the y-direction is about twice of that in the x-direction. The highest elevation of the topography is at (0 m, 2000 m), whereas the lowest one is at (2000 m, 0 m). An inflow discharge with a peak of 20 m^3 s^{-1} (Fig. 4.10) flows from a 100 m breach opening (red line, Fig. 4.10) over the initially dry terrain. When the inflow is active, the propagating flood gradually fills seven ponds near the breach (covering the points 4, 3, 2 and 1, and the points 8, 7 and 6 shown in Fig. 4.10) until the inflow empties at $t =$ 1.5 hrs. Then, driven by gravity, the flow slowly propagates into farther ponds covering the points 5, 10, 11 and 12, until the simulation terminates at t = 48 hrs. As the ponds at points 9, 13, 14, 15 and 16 remain dry during the simulation, the time histories of water level are recorded only at the remaining eleven points.

Fig. 4.11 contains the time histories of the water levels in which no difference is identified (to a precision of 1×10^{-5} m) between the predictions made by DG2-NL and DG2-LL at 20 m resolution, both delivering the best agreement with the reference solution (at a 2 m resolution). Near the breach (i.e. at points 4, 3, 2 and 1, and points 8, 7 and 6), all DG2 model predictions are found to be closer to the range of predictions made by the industrial models, as opposed to the MUSCL-FV2 predictions at 40 m resolution, which are slightly out of the range for $t > 1.5$ hrs. Further away from the breach (i.e. at points 5, 10, 11 and 12), discrepancies start to emerge, and the MUSCL-FV2 at 40 m resolution predicts the highest water levels amongst all models, whereas the DG2 variants at 20 m resolution predict the lowest. The DG2-NL at 40 m resolution is seen to deliver water levels and arrival times that

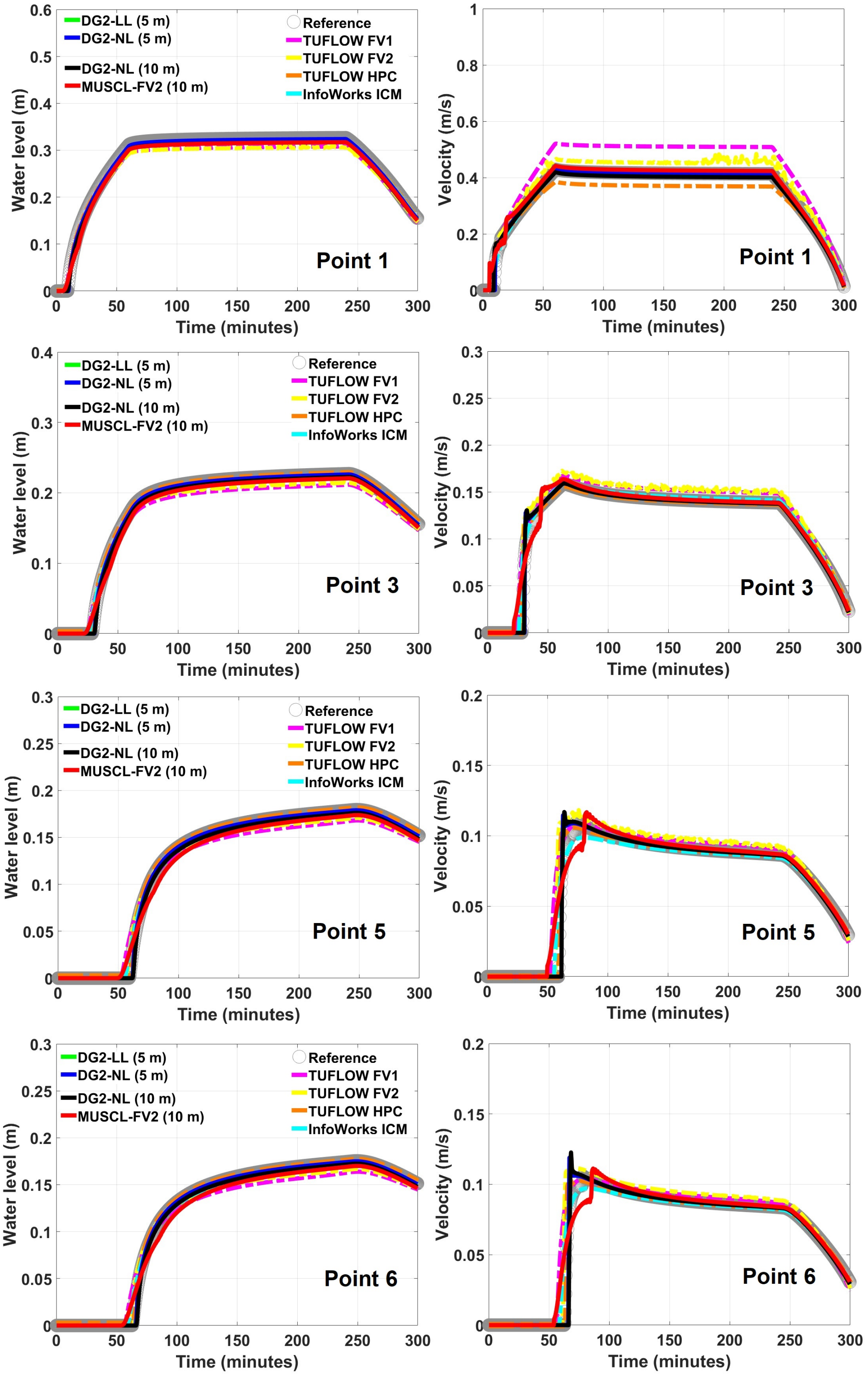

Figure 4.8: *Symmetrical flow propagation over a flat bed. Histories of the water level (left) and velocity (right) predicted by DG2-LL and DG2-NL at 5 m resolution, DG2-NL and MUSCL-FV2 at 10 m resolution, the industrial models at 5 m resolution and the reference solution at 2 m resolution.*

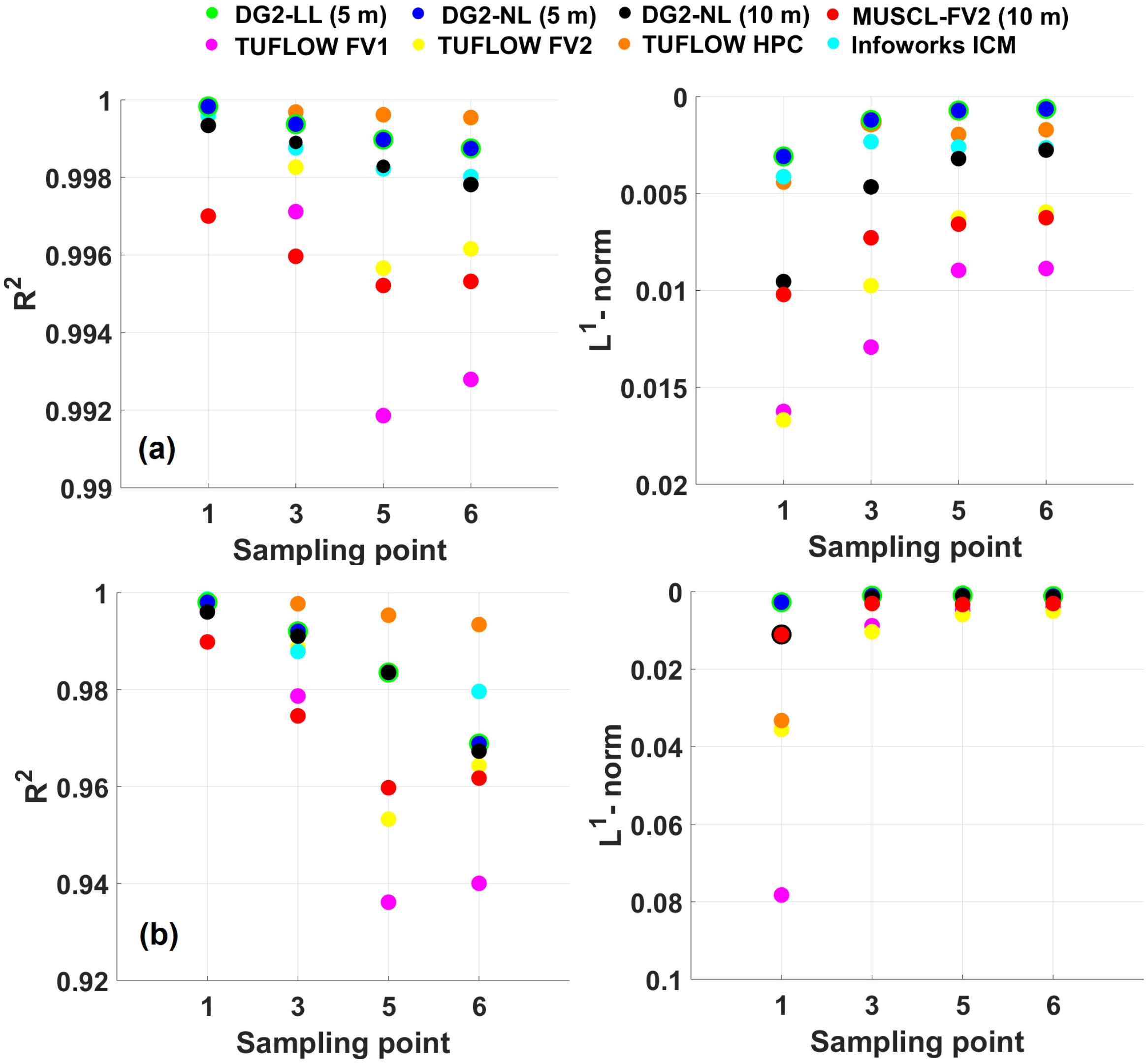

Figure 4.9: *Symmetrical flow propagation over a flat bed. Difference among the flood model predictions relative to the reference solution* R^2 *coefficients: (left) and* L^1*-norm errors (right); (a) water level and (b) velocity.*

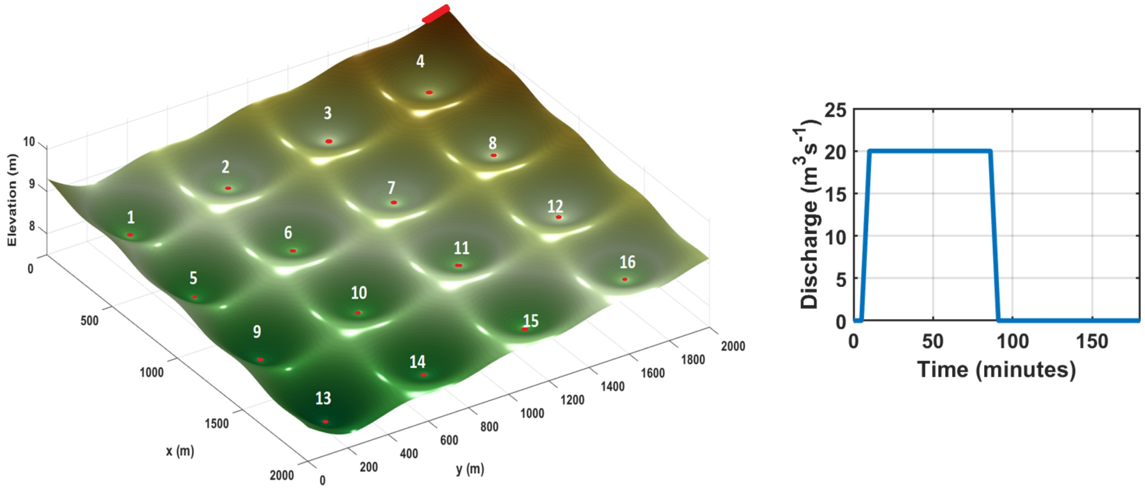

Figure 4.10: *Slow filling of multiple ponds: the left panel shows the 2D terrain including 16 ponds, the location of the breach (red line, top corner) and the sampling points (red dots) at the middle of each pond; the right panel illustrates the inflow hydrograph imposed at the breach.*

are relatively closer to the range of predictions made by the industrial models than those obtained with MUSCL-FV2.

By analysing the R^2 coefficient plots in Fig. 4.12, the largest difference in the water histories patterns is identified at the points 5, 11 and 12, where the DG2 variants at 20 m resolution offer the best agreement. Notably, DG2-NL at 40 m resolution reproduces a shape that is compatible with the reference solution ($R^2 > 0.9$) despite leading to relatively higher deviations via the L^1-norm errors. At the points located close to the breach (i.e. 4, 3, 2, 1, 8, 7 and 6), DG2-NL at 40 m resolution leads to R^2 coefficients and L^1-norm errors that are very close to those of the industrial models and DG2 variants at 20 m resolution, which is in line with the findings in Sec. 4.3.1.

Overall, this test shows that a DG2 alternative allows more accurate capturing of hydrographs over long time evolution even when taken at the same resolution as the industrial models. With a twice-as-coarse resolution, the DG2 alternative tends to produce deviated hydrographs as the location of the gauges become far away from the breach (i.e. sufficiently away from the flooding source for the flood flow propagation to be solely driven by topographic connectivities and decelerated by frictional forces). Still, compared to MUSCL-FV2,

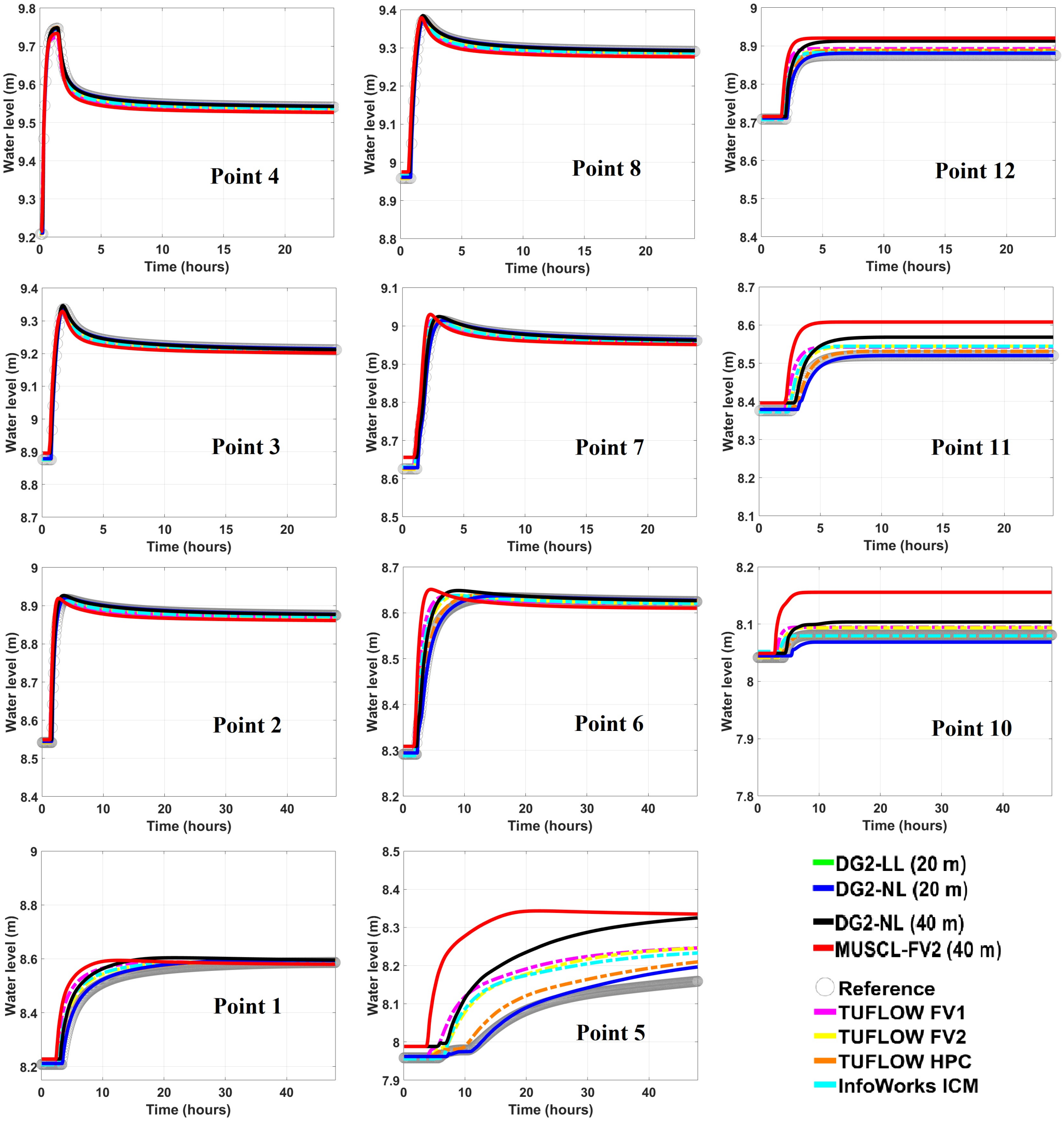

Figure 4.11: *Slow filling of multiple ponds. Water level histories recorded from the DG2-LL and DG2-NL simulations at 20 m resolution, DG2-NL and MUSCL-FV2 models at 40 m resolution, the industrial models at 20 m resolution and the reference solution at 2 m resolution.*

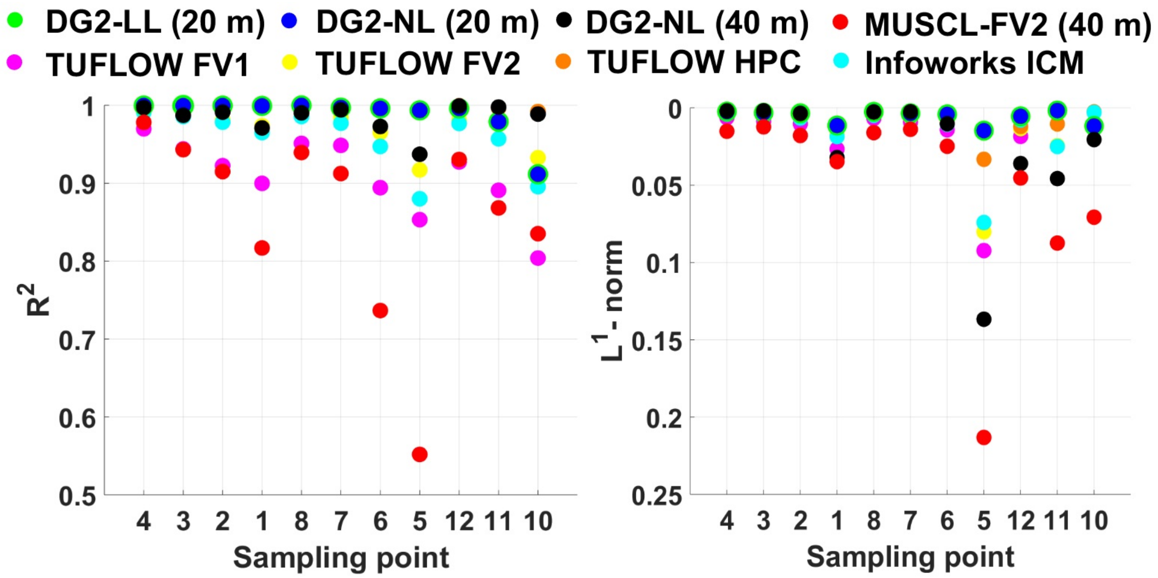

Figure 4.12: *Slow filling of multiple ponds. Difference among the flood model predictions relative to the reference solution:* R^2 *coefficients (left) and* L^1*-norm errors (right).*

the DG2 model at a twice-as-coarse resolution can produce hydrographs that better correlate with those produced by the industrial models.

4.3.4 Momentum conservation over an obstruction

This test involves a rapid unidirectional flow, filling two initially dry ponds separated by a hump at $x = 200$ m over a short duration. The 2D topography (Fig. 4.13) has a smooth surface allowing fast flow acceleration ($n_M = 0.01$). The inflow has a peak discharge of 65.5 m^3 s^{-1} (Fig. 4.13) and accelerates downslope from the west boundary to fill the first pond (Fig. 4.13, from $x = 100$ m to $x = 200$ m). While the first pond is large enough to hold the total inflow volume, models solving the full SWE tend to predict a small volume of water over-topping the hump to fill the second pond (Fig. 4.13, from $x = 200$ m to $x = 300$ m). Once all ponds are filled, the water within each pond oscillates until it completely settles. At sampling points 1 and 2 (marked in Fig. 4.13), the time histories of the water level and velocity (at point 1 only) are recorded and compared in Fig. 4.14 against those of the industrial models and the reference solution (at a 2 m resolution).

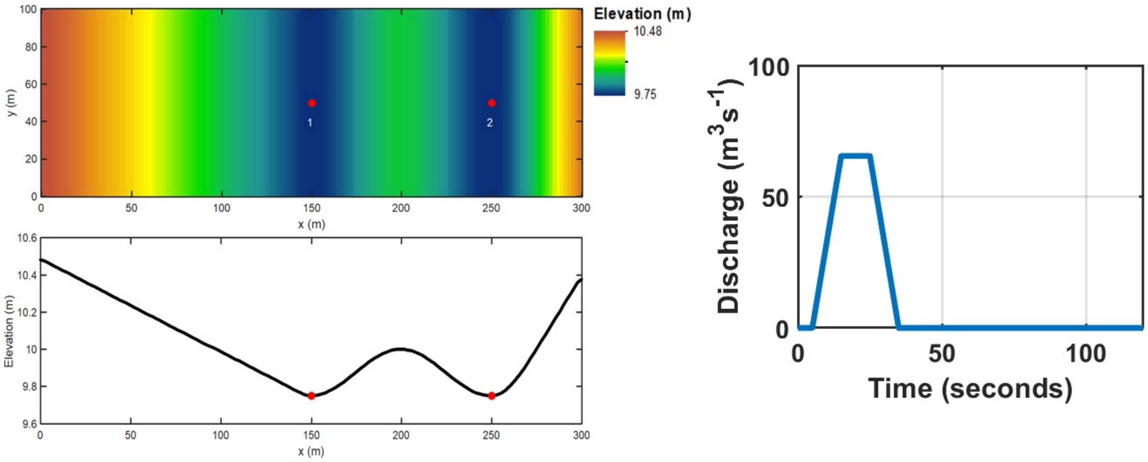

Figure 4.13: *Momentum conservation over an obstruction. Plan view and longitudinal profile of the topography with location of sampling points marked by red dots (left panel); inflow discharge hydrograph imposed at the west boundary (right panel).*

For the water level histories at point 1, the DG2 variants at 5 m resolution predicted slightly earlier wave arrival and faster flow-rising rate compared to the industrial models. These DG2 variants are also the only models that are able to capture the undulating profile visible in the reference solution (Fig. 4.14, left part in the upper panel). In terms of velocity histories, all DG2 variants at 5 and 10 m resolution exhibit a sharper peak alongside a faster rate of recession, vanishing and occurrence than the industrial models, and result in a more consistent agreement with the reference solution. The velocity histories at point 1 therefore suggests that the DG2 variants at 5 and 10 m resolution induce faster water filling patterns compared to the FV-based industrial models and the reference solution. This observation is confirmed by the water level histories of the DG2 variants at point 2. Their predicted arrival times are earlier (compare with those of point 1), which leads to faster filling, better momentum capturing, and a more defined oscillatory flow pattern that manifests as distinct undulating shapes in DG2-related water level histories (Fig. 4.14, left part in the lower panel). These shapes are not seen in the water level histories made by the FV-based industrial models, although this is barely observable in the reference solution. No major differences are noted between the DG2-NL and DG2-LL predictions, but DG2-NL is in a slightly better agreement with the reference solution for this test (Fig. 4.14, left part in the lower panel; see also

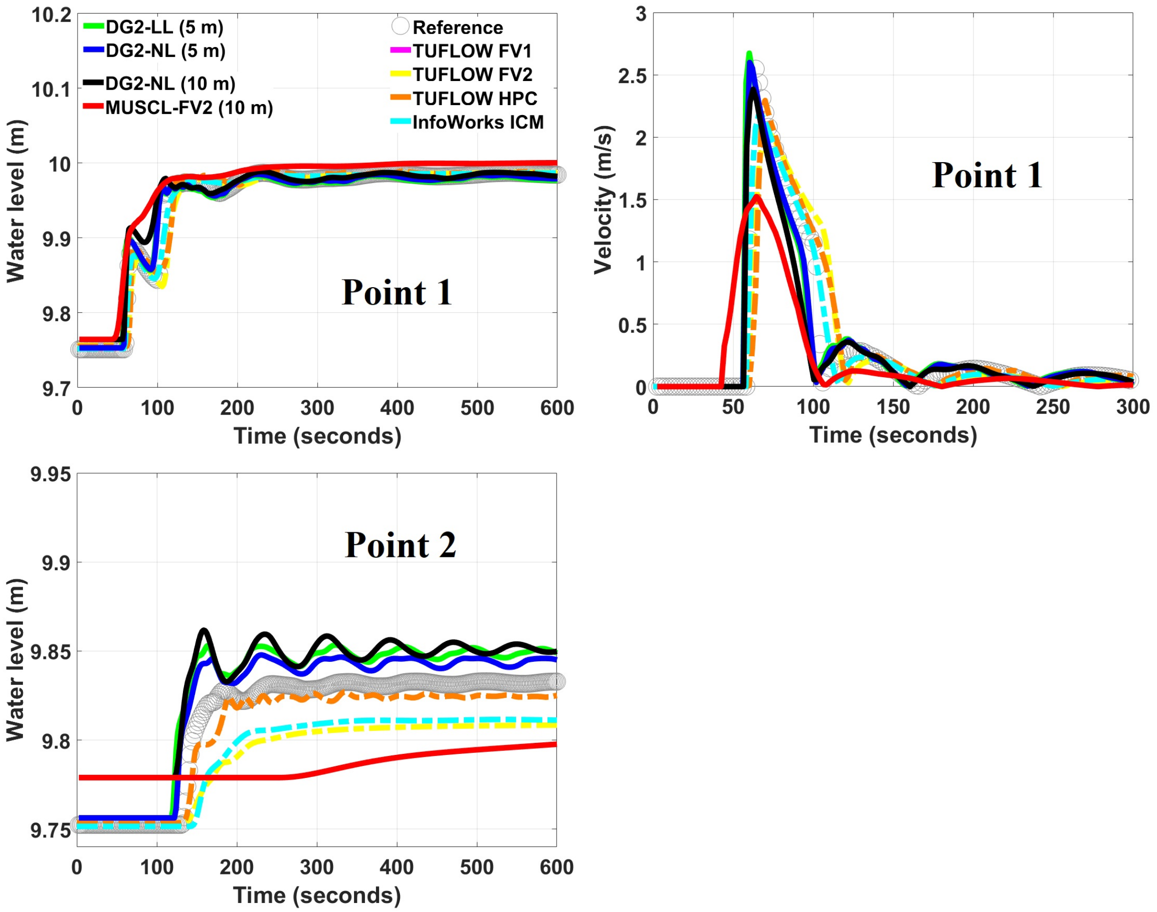

Figure 4.14: *Momentum conservation over an obstruction. Time histories of water level (at points 1 and 2) and velocity (at point 1), recorded for DG2-LL and DG2-NL at 5 m resolution, DG2-NL and MUSCL-FV2 at 10 m resolution, the industrial models at 5 m resolution and the reference solution at 2 m resolution.*

Fig. 4.15).

The analysis of the R^2 coefficient and L^1-norm error plots reinforces the DG2 variants' ability to predict profiles that are closer to the shape of the reference solution and within the range of deviation of the industrial model outputs. These metrics also allow to clearly distinguish the performance between the DG2 variants, suggesting that DG2-NL at 5 m resolution delivers better agreement with the reference solution, while still leading to competitive results at 10 m resolution. This test confirms (recall Sec. 4.3.3) the benefits of the DG2-NL alternative to also improve capturing of fast (shockless) flow, for example in flash flooding, where its better response to resolution coarsening is found to capture velocity variations better.

4.3.5 Torrential flooding over a rural catchment

This test considers a long-duration torrential flooding occurring over a down-sloping valley (Fig. 4.16) within a 17.0 km × 0.8 km rural catchment, with a naturally rugged ($n_M = 0.04$) and initially dry topography. Flooding inflow occurs from a hydrograph casting a dam breach located southwest of the valley with a peak of 3,000 m^3 s^{-1} (Fig. 4.16). The breach has a 260-m wide opening, through which the flood rapidly advances to accumulate downstream on the east side of the valley (i.e. within the area located at sampling point 5, shown in Fig. 4.16). As the flood advances, it is expected to fill shallow ground depressions along the valley. This flooding is simulated until $t = 30$ hrs. The time histories of the water level and velocity, recorded at the sampling points (marked in Fig. 4.16), are shown in Fig. 4.17, along with the histories of the industrial models and the reference solution (at 10 m resolution).

Fig. 4.17 (right side) contains the velocity histories at point 1 and point 3 (during 2 hrs), located within the mainstream flow direction (point 1 close to the breach and point 3 by the middle of the valley), and point 4 (during 3.5 hrs) located at the downstream end of the valley. At point 1, results are analysed during the first 1.5 hrs when there is still momentum forcing from the inflow: DG2 and MUSCL-FV2 at 100 m resolution yield velocities that are deviated higher (thus faster flow) from those predicted by the other models at 50 m resolution and the reference solution, although still producing the same velocity patterns. At point 3, the

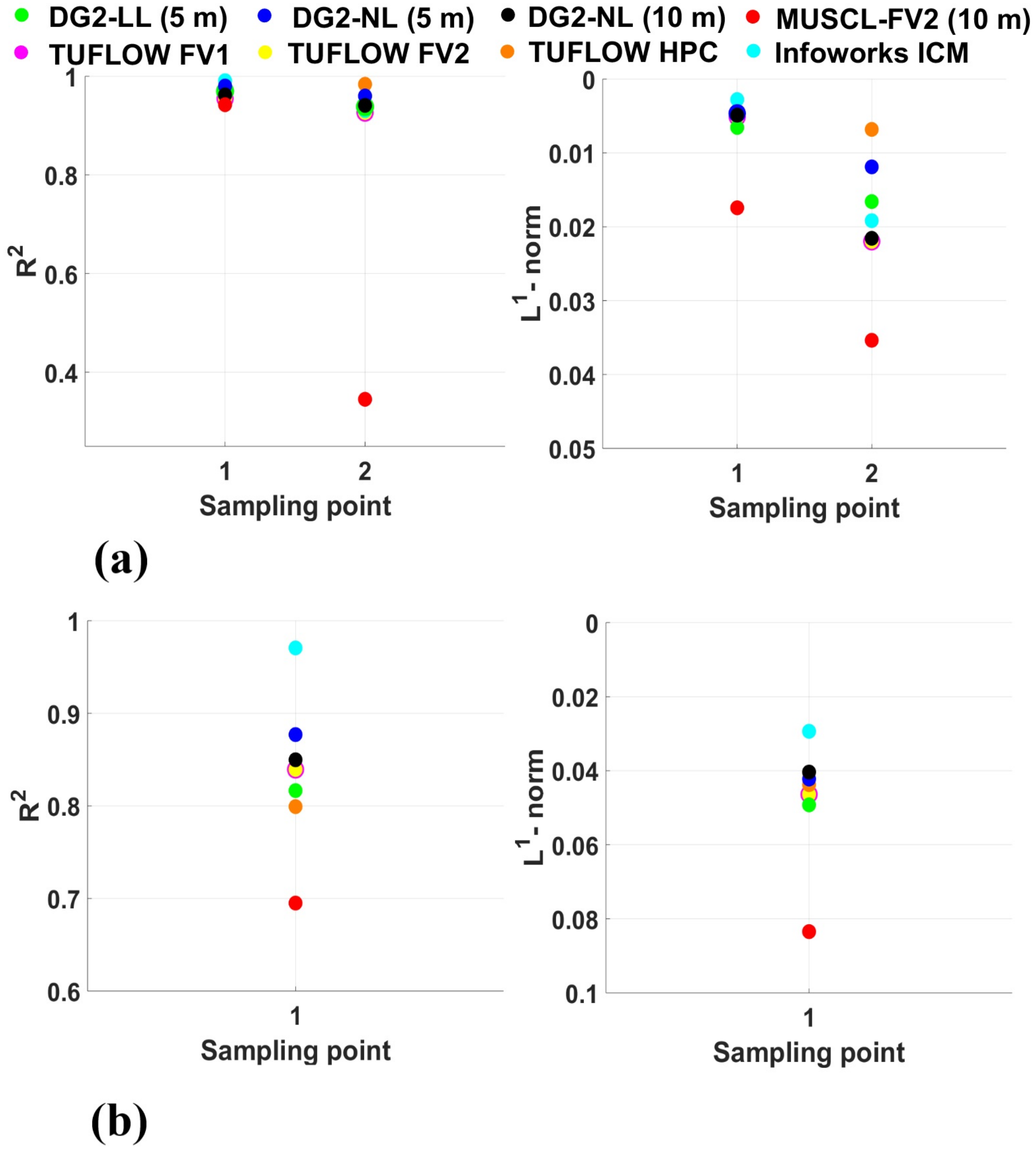

Figure 4.15: *Momentum conservation over an obstruction. Difference among the flood model predictions relative to the reference solution:* R^2 *coefficients (left) and* L^1*-norm errors (right); (a) water level and (b) velocity.*

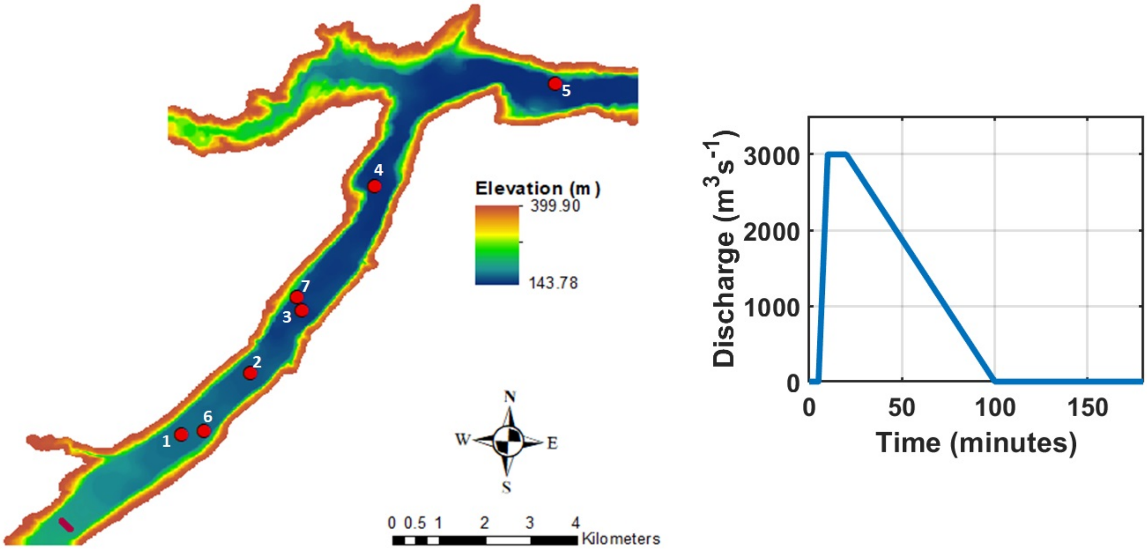

Figure 4.16: *Torrential flooding over a rural catchment. Left panel shows the 2D topography with the breach location (red line, southwest of the catchment) and the sampling points (red dots). The right panel shows inflow hydrograph imposed at the breach.*

DG2 variants at 50 m resolution capture the transient curving observed within the reference solution (∼1-1.3 hrs), which is not reproduced by any of the industrial models. At point 4, the velocities predicted by DG2 and MUSCL-FV2 at 100 m resolution are less deviated from the predictions made at 50 m resolution by the DG2 variants and the industrial models. This convergence in performance seems to arise from the fact that the flow that passes point 4 after 1.5 hrs is relatively slower (i.e. entirely driven by gravity when inflow-forcing is no longer in place and decelerated by high friction effects). However, at point 4, none of the 100 m resolution models is able to capture the undulating velocity patterns observed around 2-2.8 hrs in the 10 m reference solution generated using MUSCL-FV2, as small topographic details particularly the sharp channel bend (Fig. 4.16) have been made smoother as an effect of the DEM coarsening. Thus, a grid resolution $\leq$ 50 m is required for the DG2 variants to observe these velocity transients.

Fig. 4.17 (left side) shows the water level histories at the same points 1 and 3, and then at point 5 located farthest from the flooding source. At points 1 and 3, no major discrepancies are observed between the model predictions at both 50 m and 100 m resolution. All models

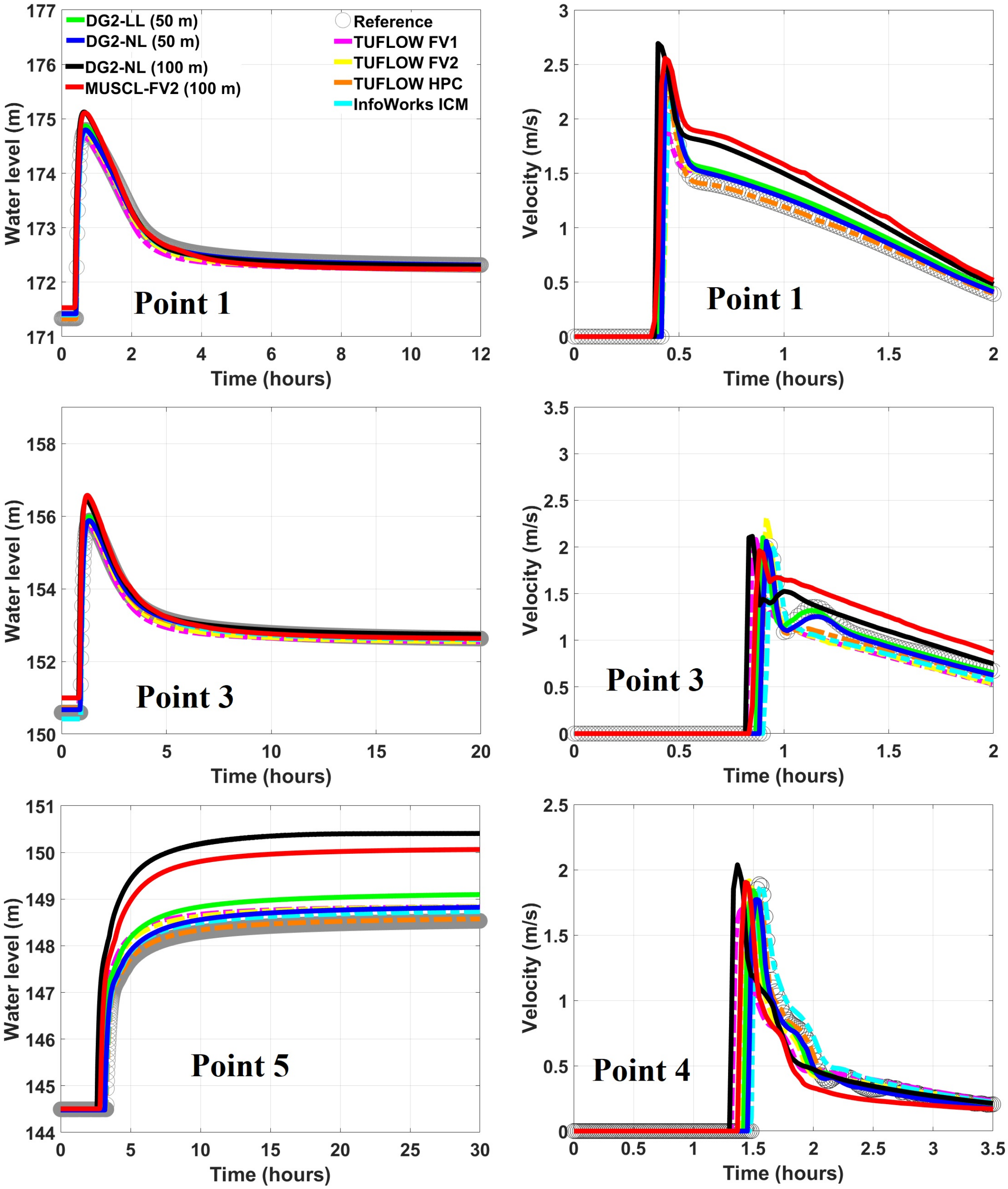

Figure 4.17: *Torrential flooding over a rural catchment. Time histories of the water level (left side) at point 1, point 3 and point 5, and of the velocity (right side) at point 1, point 3 and point 4, produced by the DG2-LL and DG2-NL at 50 m resolution, by the DG2-NL and MUSCL-FV2 models at 100 m resolution, against those produced by the industrial models at 50 m resolution and the reference solution at 10 m resolution.*

exhibit very similar water level profiles and closely match the reference solution. At point 5 where the flow arrives around 4.5 hrs of flooding, DG2 and MUSCL-FV2 at 100 m resolution predict patterns for the water level histories that are entirely consistent with those of the industrial models and DG2 variants at 50 m resolution. However, at 100 m resolution, DG2 and MUSCL-FV2 clearly present the most deviated histories from the reference solution and from the predictions made by the DG2 variants and the industrial models at 50 m resolution. Notably, the 100 m resolution models predicted faster flow arrival, particularly when the flooding duration has exceeded 24 hrs. This finding reinforces the observation in Sec. 4.3.3 that a DG2 alternative at twice-coarser resolution would yield more deviated water level hydrographs as the gauging point becomes increasingly far from the flooding source.

The observations discussed previously can be further supported by analysing the plots of the R^2 coefficients and L^1-norm errors in Fig. 4.18 at the respective sampling points. The R^2 coefficients for the water level and velocity are greater than 0.88, which indicates strong similarities with the hydrograph patterns of the reference solution. The L^1-norm error for water level predictions (Fig. 4.18a), is relatively bigger at point 5 for the models run at 100 m resolution. This indicates that resolution coarsening produces hydrographs that are fairly different than those obtained with the models run at 50 m resolution. In terms of velocity predictions (Fig. 4.18b), L^1-norm errors indicate that all model predictions at 50 and 100 m resolution yield a relatively good fit to the reference solution, and that the DG2 variants are among the best performers. Overall, for a flooding case with rapid flows over a naturally rugged terrain, a DG2-NL alternative pays off with a more accurate capturing of the velocity transients for coarse resolution modelling ($\leq$ 50 m resolution).

4.3.6 Dam-break over an oblique building

This test case considers an abrupt wave propagation involving the reflection of multiple shock waves, the formation of a hydraulic jump, and the occurrence of small-scale eddies near wake zones. These phenomena are induced by the release of a dam-break wave over an initially wet floodplain to interact with an oblique building structure and solid walls enclosing the

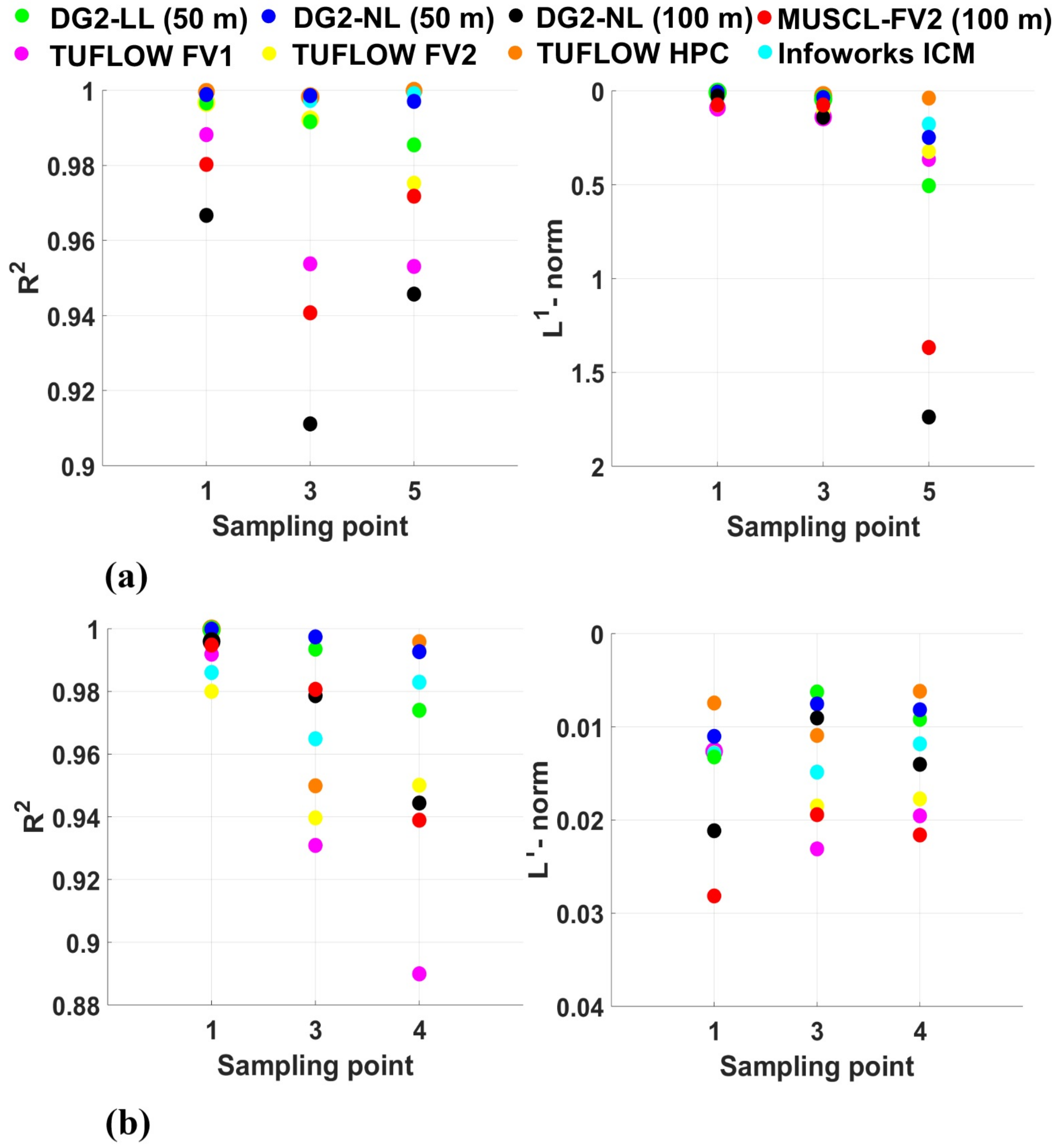

Figure 4.18: *Torrential flooding over a rural catchment. Difference among the flood model predictions relative to the reference solution:* R^2 *coefficients (left) and* L^1*-norm errors (right); (a) water level and (b) velocity.*

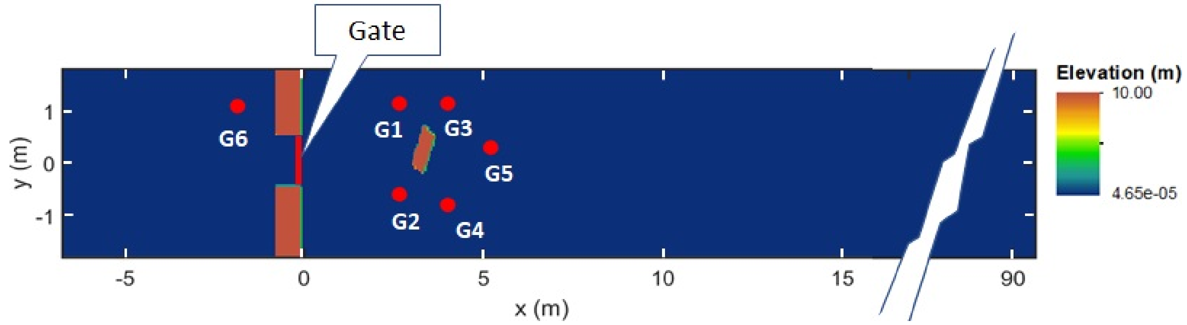

Figure 4.19: *Dam-break over an oblique building. Plan view of the spatial domain and the location of 6 sampling points (red dots).*

floodplain. The test case domain, shown in Fig. 4.19, is made of a long flume with a smooth bed ($n_M = 0.01$), and upstream walls with a gate separating two water bodies that are 0.4 m deep at the upstream and 0.02 m deep downstream. As the gate is swiftly opened, a shock wave rapidly propagates and collides with the building to form a reflected hydraulic jump (i.e. within the neighbourhood of G2, Fig. 4.19) and later splits into two shock waves that move in different directions (i.e. one towards G3 and one towards G4, Fig. 4.19). Downstream of the building, a wake zone emerges and surrounded by wave crossings, whilst producing small-scale wake eddies (i.e. within the neighbourhood of G5, Fig. 4.19). The general flow patterns in this test can be observed in the plan view of the 2D depth snapshots in Fig. 4.20.

A grid with a cell size of 0.1 m is used to discretise the whole flume, including the oblique building and the dam structure as a part of the side walls, all incorporated as bed-slope source terms within the DG2 model discretisation. Simulations are run up to $t = 30$ s, during which the time histories of the water level and the velocity are computed at sampling points G2, G4 and G5 located around the building, where highly energetic flow features occur, and at point G6 behind the dam wall, where water flow is relatively slower. The time histories of the water level produced by DG2-LL and DG2-NL and the industrial models at resolution 0.1 m, and by DG2-LL and MUSCL-FV2 at resolution 0.2 m, are compared in Fig. 4.21 against the measured data from Soares-Frazão & Zech (2007).

The water level and velocity histories at points G2 and G4 reveal that none of the models can fully reproduce the experimental profiles. At point G2, only the first wave arrival is well

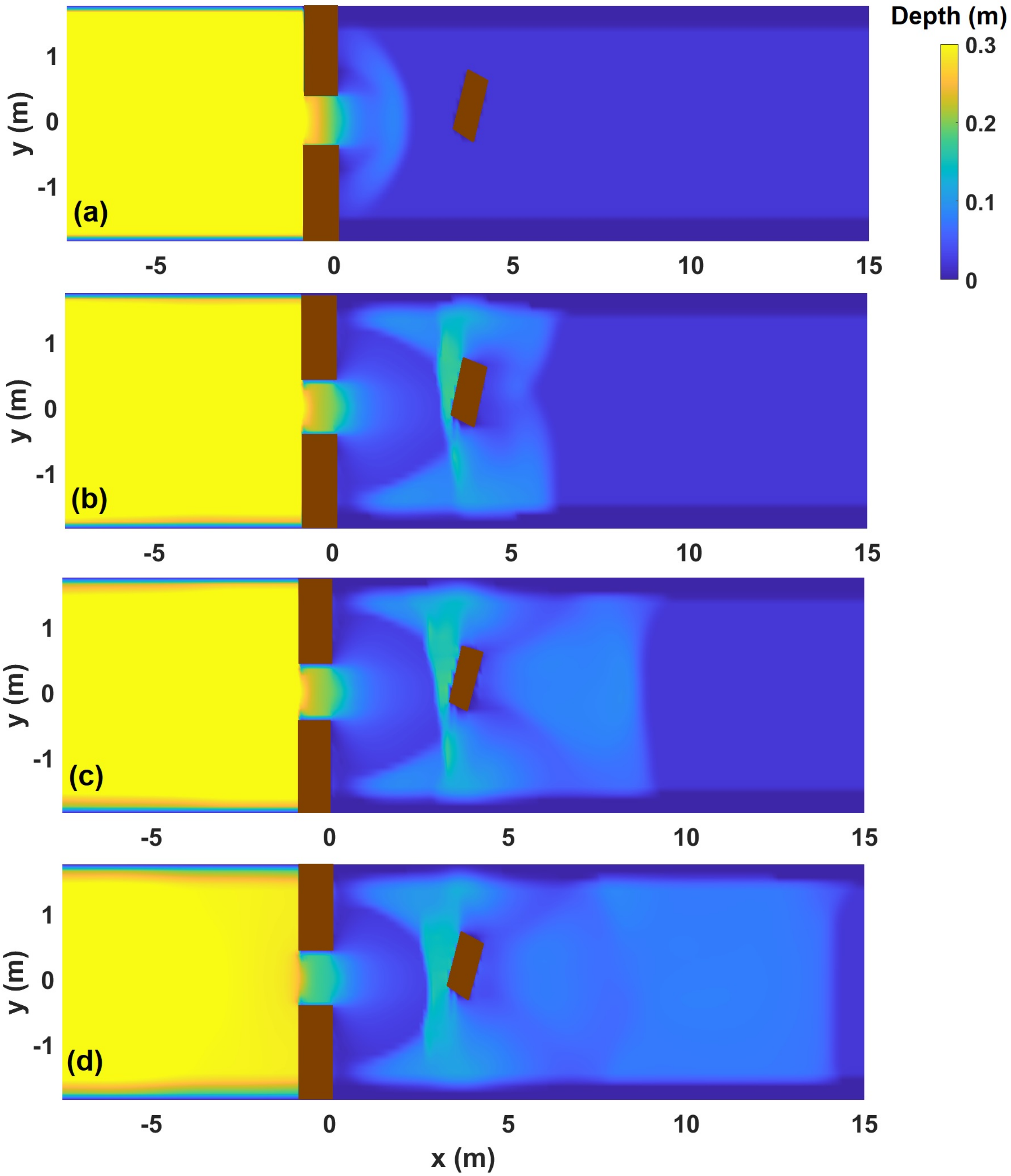

Figure 4.20: *Dam-break over an oblique building. The plan view of the 2D depth snapshot at (a) 1 s, (b) 4 s, (c) 6 s and (d) 10 s.*

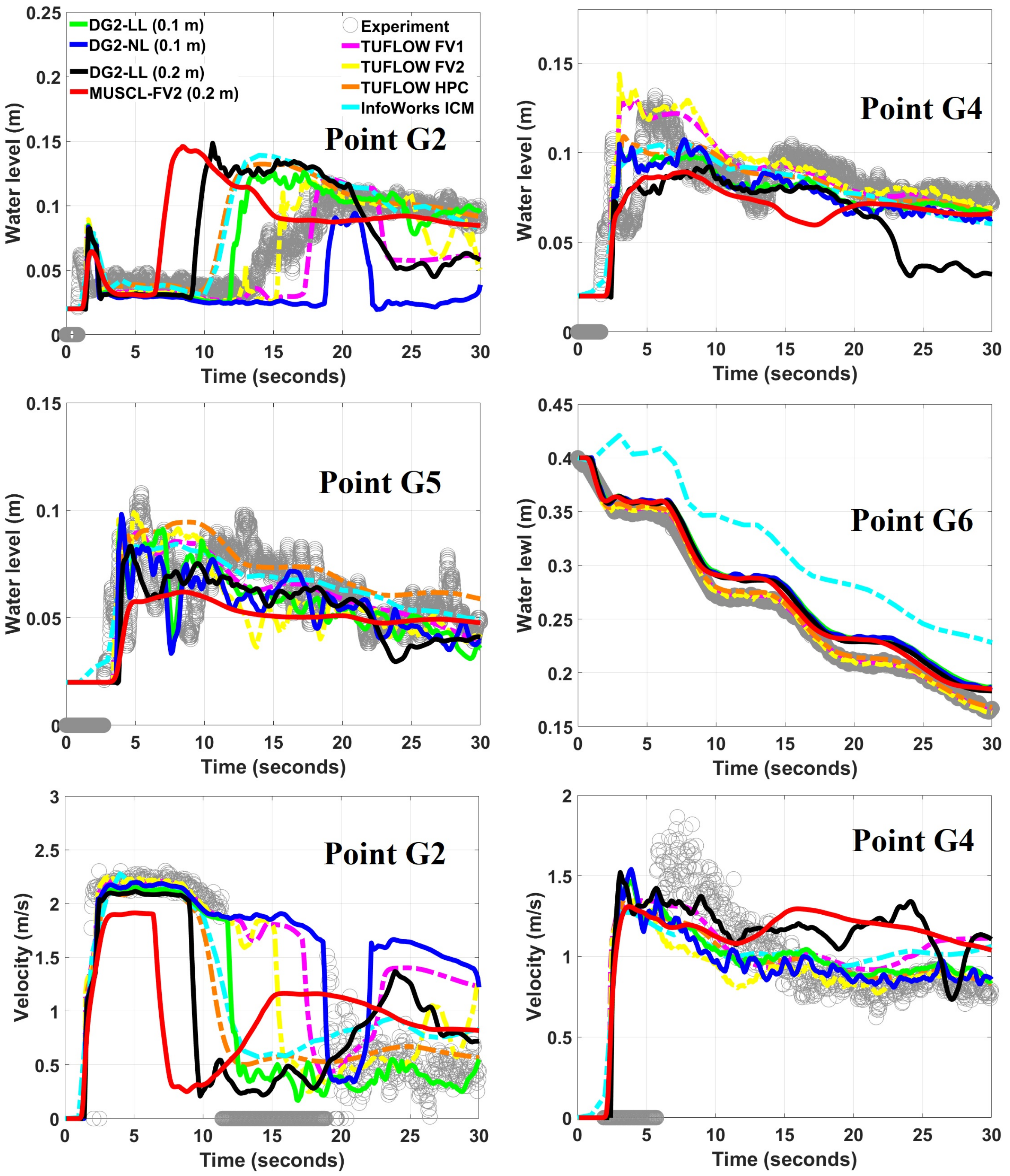

Figure 4.21: *Dam break over an oblique building. Time histories of the water level (top and middle parts) at points G2, G4, G5 and G6, and the velocity (bottom part) at points G2 and G4 relative to DG2-LL and DG2-NL at 0.1 m resolution, DG2-LL and MUSCL-FV2 models at 0.2 m resolution, the industrial models at 0.1 m resolution and the experimental data.*

captured (around 1 s) by the models, as it is clearer in the velocity predictions (Fig. 4.21, bottom panel, left part). Within the first 10-20 s, the models fail to capture the rapidly increasing water jump transition (Fig. 4.21, top panel, left part), although the velocity histories (Fig. 4.21, bottom panel, left part) indicates that DG2-LL at 0.1 m resolution is the best performer, particularly in capturing the vanishing velocity at $t \sim 11$ s. In contrast, DG2-NL at a 0.1 m resolution fails to predict meaningful results in both water level and velocity histories (Fig. 4.21, top and bottom panels, left part), which is rather an expected shortcoming when swiching-off the slope limiter within a shock-dominated flow simulations. At point G4, the predicted depth and velocity histories indicate more clearly that none of the models can appropriately reproduce the experimental wave arrival times, which are smeared out (Fig. 4.21, top panel, right part) and predicted with a significant lag (Fig. 4.21, bottom panel, right part). These shortcomings in model predictions are not surprising as the wave patterns around points G2 and G4 become complex and highly unstable to be captured by 2D-SWE models under the hydrostatic assumption and without a turbulence closure. Nonetheless, the time histories at G2 and G4 still show benefits in applying DG2-LL to sufficiently reproduce small-scale transient features occurring in a highly dynamic flow type.

The DG2-LL capability is clearly discernible in the water level histories recorded at point G5 (Fig. 4.21, middle panel, left part). There, DG2-LL at a 0.1 m resolution excels in capturing the varying disturbances observed in the experimental histories with greater accuracy as compared to the industrial models, even at 0.2 m resolution where MUSCL-FV2 yields a relatively flat histories without disturbances. At point G6, where the flow is very much flood-like, the DG2 variants at 0.2 m resolution perform equally well as other models at 0.1 m resolution, thus demonstrating that the DG2 model can be a viable option to predict flows away from the shock-dominated area at twice-coarser resolution than those of the FV-based models. The better fit of the TUFLOW model predictions with the measured data are likely due to the addition and ad-hoc calibration of eddy viscosity parameters. These parameters are used as counterbalancing measure to the so-called “resolution-to-depth” ratio effect as it becomes significant in line with the increase of modelling resolution and water depth (Syme

2008).

Fig. 4.22 contains the plots of the R^2 coefficients and L^1-norm errors at the respective sampling points. Except for point G6, the R^2 coefficients for the water level are at best around 0.6. This suggests that all models reproduce history patterns that are more than 60% distorted from the experimental patterns, although without a significant deviation since the L^1-norm errors do not exceed 0.06 m. On the other hand, the R^2 coefficients for the velocities are more illustrative of the DG2-LL's potential in capturing the transient patterns in a fast and abrupt flow ($\mathrm{R}^2 > 0.6$), leading to the least deviated results (smallest L^1-norm error). Overall, this test recommends DG2-LL model to simulate complex flow hydrodynamics with shocks and to be particularly useful in the capturing of small-scale transients around eddy wakes.

4.4 Computational runtimes and discussions

For each test case in Secs. 4.3.1 - 4.3.6, the runtimes generated by DG2-NL, DG2-LL and MUSCL-FV2 are recorded at output time T as reported for the industrial models (Table 4.1) and for the best performer DG2 variant (DG2-BP) on a twice-coarser resolution. The selected DG2-BP is the DG2 variant that produced the highest R^2 and lowest L^1-norm errors in the flow predictions at all (or most) gauging points. If the values produced by both DG2 variants are similar, then the DG2-BP is selected based on the fastest recorded runtimes. The models' runtimes, listed in Table 4.3, are recorded on the same desktop computer using a single-core CPU. Note that these runtimes are not compared with those reported for the industrial models, as these models were run some time ago by their respective software packages suppliers, either a CPU with 12 cores or a GPU card with thousands of CUDA cores. The mass balance errors for the MUSCL-FV2 and the DG2 variants in the UK EA test cases are considered minimal, with errors less than 1%.

As shown in Table 4.3, the runtimes of DG2-NL are found to be 1.8 to 2.2 times faster than those of DG2-LL in the first five test cases involving flood-like flows (Secs. 4.3.1 to 4.3.5). Compared to the runtimes of MUSCL-FV2 on the same resolution as the industrial

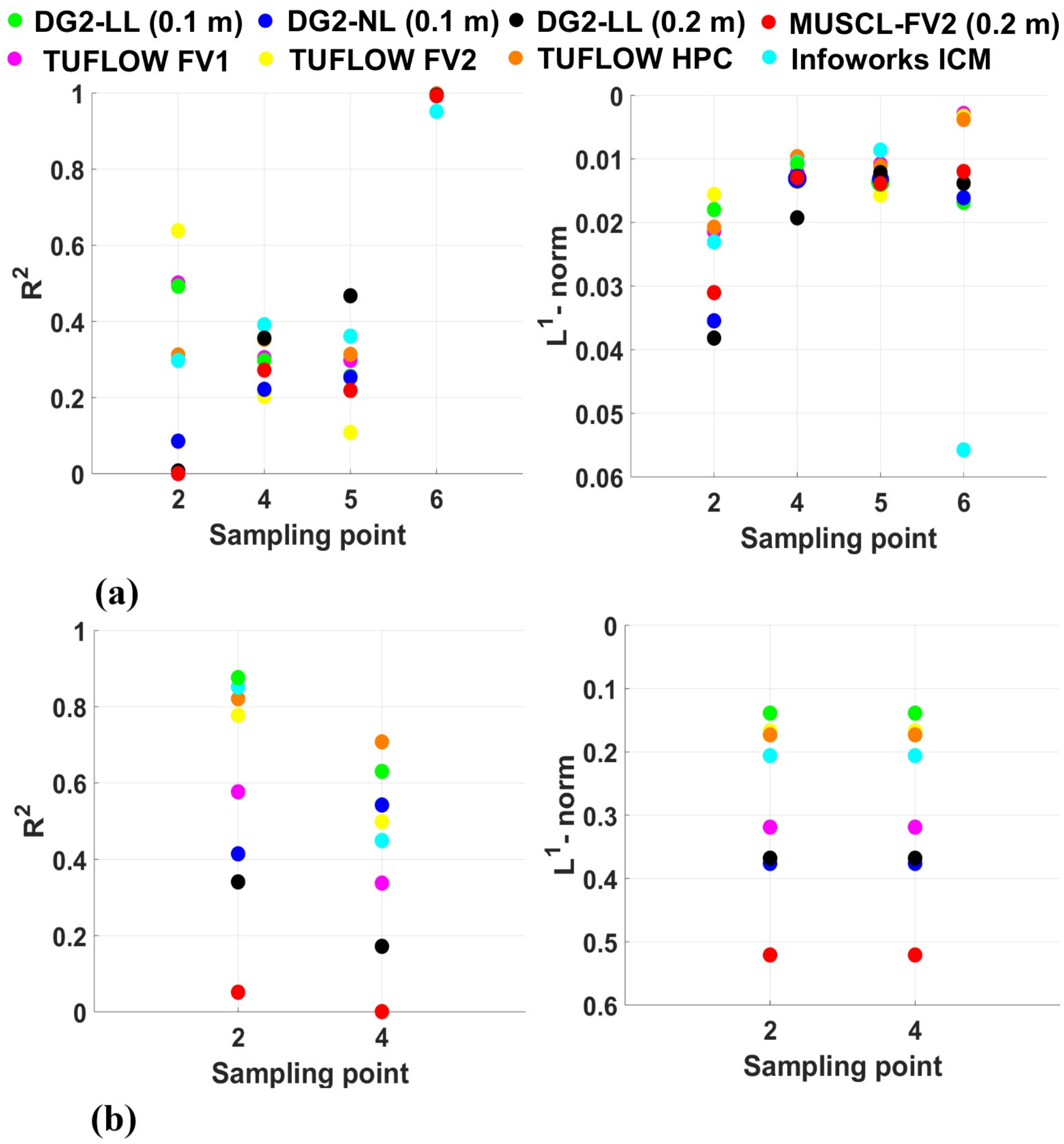

Figure 4.22: *Dam break over an oblique building. Difference among the flood model predictions relative to the experimental data:* R^2 *coefficients (left) and* L^1*-norm errors (right); (a) water level and (b) velocity.*

Table 4.3: *Runtime costs for DG2-NL, DG2-LL and MUSCL-FV2 based on the same grid resolution reported for the industrial models (Table 4.1), and considering the best performer DG2 variant (DG2-BP) on twice-coarser resolution. All simulation runtimes are generated from the same desktop computer using a single-core CPU.*

Test cases	Output time T	Runtimes (sec): same resolution reported for the industrial models			Runtimes (s): twice-coarser resolution
		DG2-LL	DG2-NL	MUSCL-FV2	DG2-BP
Flooding and drying cycle over a sloping topography (Sec. 4.3.1)	20 hrs	166	75	69	21
Symmetrical flow propagation over a flat bed (Sec. 4.3.2)	5 hrs	9,350	4,373	3,416	515
Slow filling of multiple ponds (Sec. 4.3.3)	48 hrs	1,734	833	307	222
Momentum conservation over an obstruction (Sec. 4.3.4)	15 min	12	5.5	3.4	1.5
Torrential flooding over a rural catchment (Sec. 4.3.5)	30 hrs	22,260	12,297	3,822	2,320
Dam break over an oblique building (Sec. 4.3.6)	2 min	15,337	10,363	1,205	497

models, DG2-NL is found to be 1.4 to 6.6 times faster on twice-coarser resolution. Hence, DG2-NL is undoubtedly the best performer to support realistic flood modelling over large spatial areas and long timescales. DG2-NL partly falls short around the zone of shock-dominance (Sec. 4.3.6) and has the least speed up compared to DG2-LL (i.e. 1.4 times). For the simulation of flooding scenarios with shocks and wave reflection, e.g. a tsunami or dam-break wave propagation over across obstacles, DG2-LL should still be favoured as the best performer.

4.5 Concluding remarks

The potential of a DG2 model for practical flood modelling has been studied in comparison to industry-standard flood models, which are based on second-order finite volume (FV2) or first-order finite volume (FV1) numerical solvers. A simplified form of the DG2 flood model that is devised for robust flood modelling was presented, while drawing on its key similarities and differences to the standard MUSCL-FV2 approach. Results from a synthetic test revealed notable momentum conservation property of the DG2 model due to its greater ability to withstand numerical dissipation, despite the grid resolution coarsening and long duration of simulation. This analysis also shows that the DG2 model with no slope limiting (DG2-NL) is as valid as the expensive variant with local slope limiting (DG2-LL) in simulating flood-like flows with wetting and drying movement that are often present in flood inundation modelling.

The performance of the DG2-LL and DG2-NL models was then explored for six test cases published by the UK Environment Agency, which are well-accepted by both industrial and academic hydraulic modelling communities for benchmarking the capabilities of 2D flood inundation models. The outputs of DG2-LL and DG2-NL were analysed and compared to the outputs of four prominent FV-based industrial models (i.e. TUFLOW-FV1, TUFLOW-FV2, TUFLOW-HPC and Infoworks ICM) for the same resolution reported for the industrial models. Outputs of the best performing DG2 variant (DG2-BP) were then analysed at twice-coarser resolution compared to the outputs of an in-house MUSCL-FV2 model. All analyses are quantified using R^2 coefficient and L^1-norm errors, representing the correlation and deviation of the model outputs with respect to a reference solution, either produced by running MUSCL-FV2 on the finest DEM available or via available measurement data. CPU runtimes were also scrutinised to contrast the runtime cost of DG2-LL *vs.* DG2-NL on the same resolution as the industrial models, and also DG2-BP *vs.* MUSCL-FV2 on a twice-coarser resolution.

The performance comparison between DG2 and FV-based model outputs offered a deeper insight into the practical requirements and the potential for deploying a grid-based DG2 flood model for industry-scale simulations. Local limiting was found to be unnecessary for a DG2 model to reliably support the modelling of a wide range of flooding flows (i.e. not dominated by strong flow discontinuities) such as in pluvial, fluvial and coastal flooding. The DG2-LL costs twice as much to run (Sec. 4.4) and can still produce misleading results, for example when a gradually-propagating inflow is still loading onto a small wet domain (Sec. 4.3.1). The DG2-NL yields closer predictions to the industrial model outputs, even at twice-coarser resolution such as seen in a symmetrical flow over a floodplain (Sec. 4.3.2). The DG2-NL at twice-coarser resolution could maintain a good correlation to the industrial models in simulating a flood flow driven by topographic- and friction-effects over a larger area (Sec. 4.3.3) and sample more accurately the water level hydrographs far away from the flood source.

For rapidly propagating flood waves on downslope channel with ponding (Sec. 4.3.4) and over a real-world natural valley (Sec. 4.3.5), DG2-NL, including at twice-coarser resolution, has shown ability to capture more detailed flow hydrographs incorporating small-scale transients. In particular, DG2-NL displayed sharper velocity peak and distinct oscillatory patterns of a sloshing flow settling in the ponds (Sec. 4.3.4) and managed to capture small transient curving in the velocity predictions (Sec. 4.3.5). In contrast, for a case with a strong dam-break wave interacting with a building-like obstacle (Sec. 4.3.6), deploying DG2-LL may still be useful for detailed capturing of small-scale flow variations caused by highly dynamic wave interactions with obstacles. Nonetheless, away from the shock-dominated region e.g. behind the dam wall (Sec. 4.3.6), DG2-NL can still produce competitive results relative to the industrial model outcomes. Overall, these findings lead to the conclusion that DG2-NL can offer a more efficient and accurate alternative for the industrial modelling communities to improve long-range and coarse-resolution flood flow simulations.

Chapter 5

Velocity fields predictions with small-scale eddies

Contents used to prepare for this chapter have been published in the following publication:

Ayog, J. L., Kesserwani, G, Bau, D. 2021. Well-resolved velocity fields using discontinuous Galerkin shallow water solutions, J. Hydraul. Eng. in review. The preprint is available in http://arxiv.org/abs/2104.11308.

5.1 Chapter overview

This chapter, which relates to Objective 3, extends the investigation made on the performance of the simplified 2D-SWE DG2 solver in Chapter 4, particularly in predicting detailed spatial velocity fields at sub-metre resolutions. The capabilities of this DG2 solver are further studied relative to the commonly-used MUSCL-FV2 solver through a series of selected test cases in which spatial velocity field experiments are available. In Sec. 5.2, the selected test cases that are used to assess the capabilities of the DG2 solver relative to MUSCL-FV2 solver are presented. These test cases involve small-scale flow interaction with steep topographic structures, for a wide range of flow regimes and transitions and considering a real-world flooding scenario in a residential area. The performance of the DG2 solver is then analysed for two configurations, with and without activating local slope limiting (i.e. DG-NL and DG-LL), jointly with that of the MUSCL-FV2 solver. Sec. 5.3 presents the analyses of performances include a qualitative comparison of predicted velocity streamlines in the areas with recirculation flows, and an evaluation based on a range of quantitative indices (described in Sec. 5.2). Finally, Sec. 5.4 presents the conclusions drawn from the analyses to come up with a most suitable configuration for the DG2 solver for more efficient and accurate 2D velocity field predictions, which are detailed enough to capture the small-scale features in and around the zones of wave-structure interactions in realistic flooding conditions.

5.2 Selection of test cases and quantitative indices

Test cases with experimental velocity fields are selected to study the predictive capability of the DG2 solver in the reproduction of spatial 2D velocity fields, at the sub-metre resolution, for hydraulic simulation problems that are characterised by wave-structure interactions. The features of the selected test cases, along with the experiment data sources, are summarised in Table 5.1. In the first two tests, the DG2-LL and DG2-NL variants are compared to identify and adopt a DG2 configuration that is most suited for the intended hydraulic simulation problems. The adopted DG2 variant is analysed further in the other test cases, all of which involve alternative simulation outcomes from the MUSCL-FV2 predictions to investigate the transferability of the DG2 solver to practical-scale velocity fields.

As in Chapter 4, the quantitative analyses are performed using the R^2 coefficient of determination and the L^1-norm error, but involving only the **2D velocity vectors and spatial profiles** produced by DG2 and MUSCL-FV2 solvers. Hence, these quantitative indices are now expressed as:

$$\mathrm{R}^2 = \left[\frac{\sum_{k=1}^{N_s} (V_k^{EXP} - \bar{V}^{EXP})(V_k^{NUM} - \bar{V}^{NUM})}{\sqrt{\sum_{k=1}^{N_s} (V_k^{EXP} - \bar{V}^{EXP})^2 \sum_{k=1}^{N_s} (V_k^{NUM} - \bar{V}^{NUM})^2}} \right] \tag{5.1}$$

$$L^1\text{-norm error} = \frac{1}{N_s} \left(\sum_{k=1}^{N_s} \left| V_k^{EXP} - V_k^{NUM} \right| \right) \tag{5.2}$$

Table 5.1: *The description of the selected test cases with their respective features and experimental data sources*

Test case	Features and experimental data source
Dam-break flow through multiple blocks	Highly transient flow narrowly constricted between sharp-edged obstacles followed by a downstream hydraulic jump. The spatial profiles of the depths and velocity magnitudes from the experimental measurements were obtained from Soares-Frazão & Zech (2008).
Flow separation at a T-junction	Steady subcritical flow separation considering two different T-junction configurations - with and without a small obstacle – with a recirculation zone along the lateral branch. The recirculation flow extent, and the lateral profiles of the experimental velocity components were obtained from Bazin et al. (2017).
Quasi-steady flow in sharp building cavities	Inflow with skewed velocities, and high-resolution measurements of 2D velocity fields containing small-scale eddies in the side cavities of two adjacent buildings. Relevant experimental data measured using particle image velocimetry (PIV) is provided in Rubinato et al. (2021).
Flooding in an urban residential area	Real-world flash flooding scenario around buildings on small piers simulated using a high-resolution digital elevation model (DEM). The DEM of the physical model, measured water level time histories and the spatial velocity vectors are sourced from Smith et al. (2016).

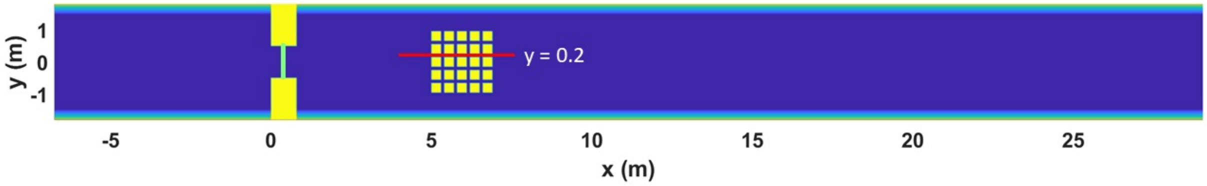

Figure 5.1: *Plan view of the spatial domain, indicating the location of the gate (green line) and the location of the extracted water level and velocity profiles (red line).*

In Eqs. 5.1 - 5.2, V^{EXP} and V^{NUM} are the velocity magnitudes from the experiments, whereas $\bar{V}^{EXP}$ and $\bar{V}^{NUM}$ represent their numerical counterparts calculated as space-averaged velocity magnitudes. N_s denotes the total number of sampled data with $k = 1$, ... N_s. The indices for the spatial profiles are calculated in a similar manner to the 2D velocity vectors, but by using the spatial point values instead of the velocity magnitudes. Besides these indices, another quantitative index, named the relevance index (RI), is used to analyse velocity field directions, and is expressed as:

$$\mathrm{RI} = \frac{1}{N_s}\left(\sum_{k=1}^{N_s} \frac{\left(u_k^{EXP} \times u_k^{NUM}\right) + \left(v_k^{EXP} \times v_k^{NUM}\right)}{V_k^{EXP} \times V_k^{NUM}}\right) \tag{5.3}$$

where u^{EXP} and v^{EXP} are the 2D velocity components from experimental observations and u^{NUM} and v^{NUM} are those from the numerical solvers. The coefficient RI is used to quantify the directional alignment of the predicted velocity fields to experimental observation, with the velocity alignment becoming higher as the RI approaches unity.

5.3 Test results and discussions

5.3.1 Dam-break flow through multiple blocks

This test is aimed to identify a range of practical applications at which local limiting within DG2 (DG2-LL) is needed. In Chapter 4, when analysing the hydrodynamics of a dam-break wave interaction around one building block (Sec. 4.3.6), the DG2-LL proved necessary to capture physically-meaningful depth and velocity time histories at fixed spatial points behind

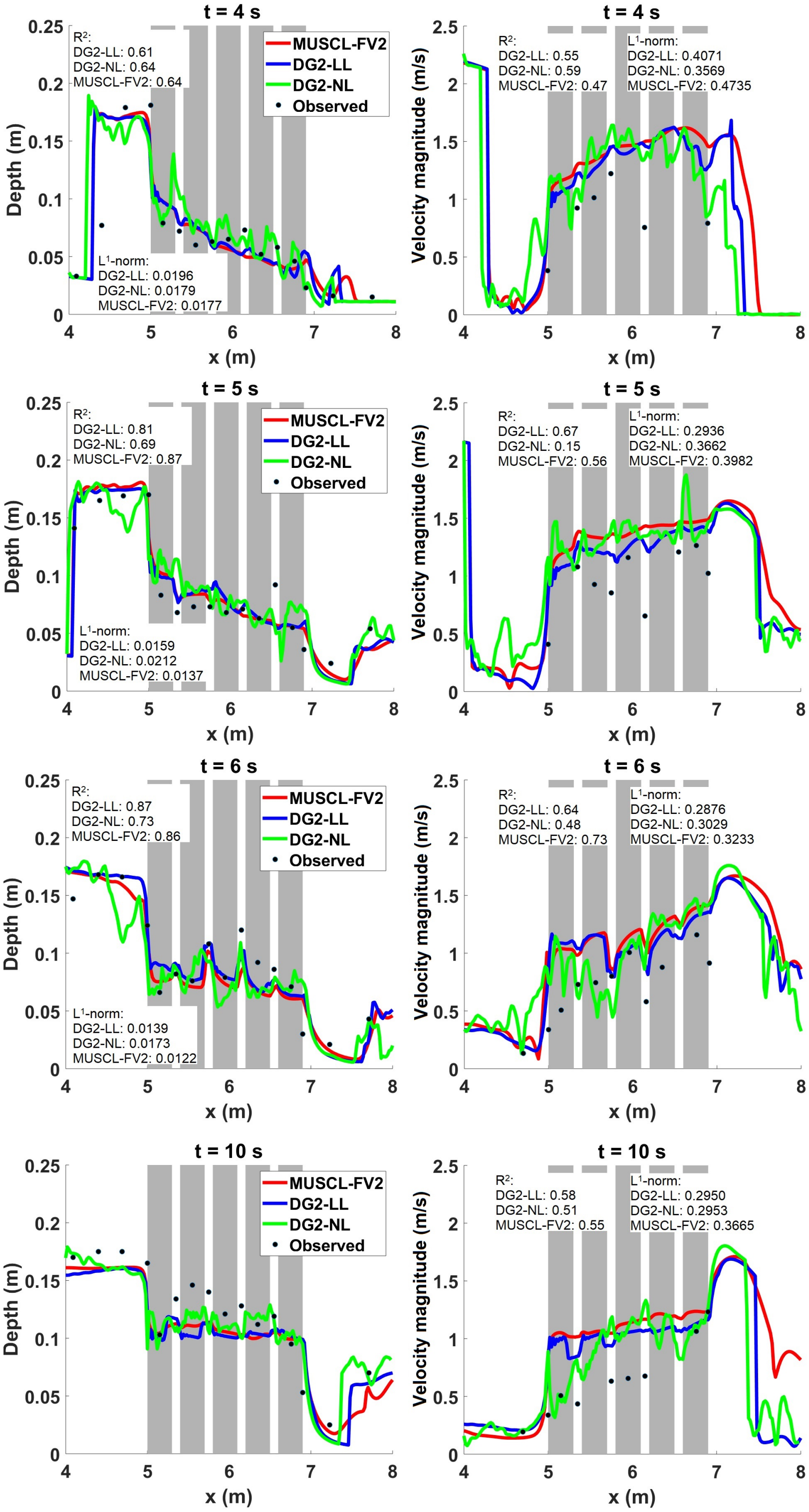

Figure 5.2: *Longitudinal profiles of the depths (left) and velocity magnitudes (right) of MUSCL-FV2 (red line), DG2-LL (blue line) and DG2-NL (green line) extracted along y = 0.2 m relative to the experimental observations (black dots) at t = 4, 5, 6 and 10 s. The grey shades indicate the building blocks, and the white strips between the blocks are the flow intersections. The* R^2 *coefficients and* L^1*-norm errors of each model are provided in the figure.*

the block. Therefore, a further investigation is required on the validity of the DG2-LL variant in a more challenging setting, such as when extracting depth and velocity spatial profiles at a given time and when the dam-break flow hydrodynamics is affected by the presence of multiple building blocks.

The test is based on the experiment of Soares-Frazão & Zech (2008). It consists of a long flume (Fig. 5.1) with a smooth bed surface ($n_M = 0.01$ m$^{1/3}$s^{-1}). The flume contains twenty-five square blocks, each of 0.3 m × 0.3 m dimension and separated by a 0.1 m gap. The blocks are meant to represent an idealised city located on a flat floodplain downstream of the flume, which also contains a gate separating a 0.4 m and a 0.011 m deep water body. When the gate is swiftly removed, a dam-break wave occurs to propagate toward the blocks and interact with them. The presence of the blocks on the floodplain constricts the flow from moving further into the narrow gaps except for a small amount of water that accelerates across the blocks and forms a hydraulic jump downstream. The constricted flow forms a backwater zone in which the water depth upstream of the blocks is raised. The backwater zone spreads to the flume side walls over time and pushes lateral flows between the building blocks until the flow stabilises. This simulation is run up to $t = 10$ s on a mesh with a grid size of 0.02 m. The longitudinal profiles of water depth and velocity magnitude obtained from DG2-NL, DG2-LL and MUSCL-FV2 at $t = 4$, 5, 6 and 10 s are extracted along $y = 0.2$ m (red line, Fig. 5.1). They are shown in Fig. 5.2, where they are also compared with observed longitudinal profiles.

As seen in Fig. 5.2, the DG2-LL produces relatively smooth patterns for the longitudinal profiles that are akin to those generated by MUSCL-FV2, but in a slightly better agreement with the observed profiles. In contrast, DG2-NL generates profiles with widespread noises, as expected when slope limiting is disabled within highly dynamic flow transitions around steep obstacles. Still, DG2-NL profiles are observed to follow the observed profiles reasonably well, in particular at the early stages of the dam-break wave propagation. This can be seen in the profiles predicted at $t = 4$ s, when the DG2-NL results are better correlated to the observed experimental data. As water becomes deeper within the gaps at $t = 5$ s, the DG2-LL retains

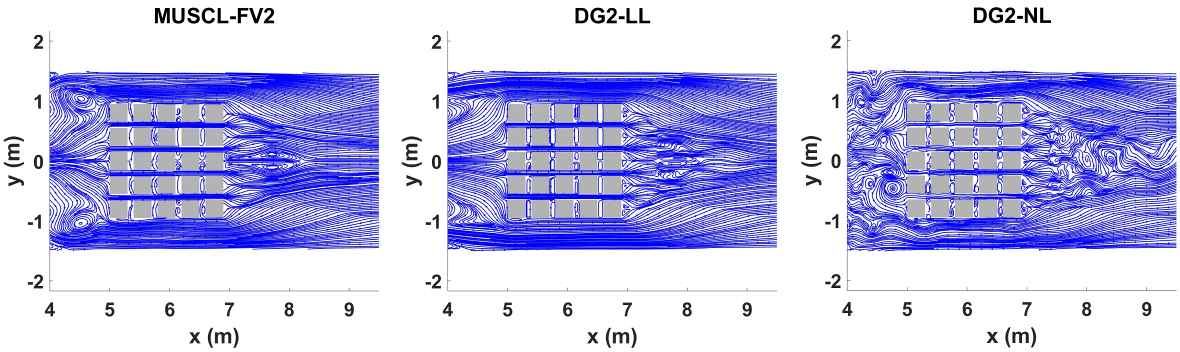

Figure 5.3: *Streamlines of 2D velocity fields produced by the MUSCL-FV2 (left), the DG2-LL (middle) and the DG2-NL (right) solvers around all blocks at* $t = 10$ *s.*

a significantly stronger correlation, whereas the DG2-NL shows the most deviated prediction from the experimentally observed profiles, as the largest L^1-norm error indicates. At $t = 6$ s and $t = 10$ s, the DG2-LL also stands out in producing profiles that more closely resemble those of the MUSCL-FV2 (compare their R^2 coefficients in Fig. 5.2) and are closer to the observed profiles compared to DG2-NL (compare their L^1-norm errors in Fig. 5.2). For the velocity magnitude profiles, in particular, DG2-LL gives the best fit of the profiles to the observed profiles at the output time, $t = 10$ s, where it shows the highest R^2 and the lowest L^1-norm errors amongst all the models. The findings in Fig. 5.2 suggest that the DG2-LL is a better option to more reliably predict velocities in highly transient flows including complex interactions with topographic structures.

To gain deeper insights into the velocity patterns observed in the longitudinal profiles in Fig. 5.2, analyses have been performed considering the streamlines extracted from the numerically predicted 2D velocity fields around the blocks at the output $t = 10$ s. The streamlines made from the predictions of the MUSCL-FV2, the DG2-LL and the DG2-NL are shown in Fig. 5.3. The DG2-LL displayed smooth streamlines, consistent with its longitudinal profiles (Fig. 5.2), with regular distribution patterns around the blocks particularly in the upstream backwater zone ($x < 5$ m), in the x-directional gaps between the blocks (5 m $\leq x \leq$ 6.9 m) and in the wake downstream, where successive converging crossflows are noted with two elongated eddies at the wake edge ($x > 6.9$ m). Similar features are also seen in the MUSCL-

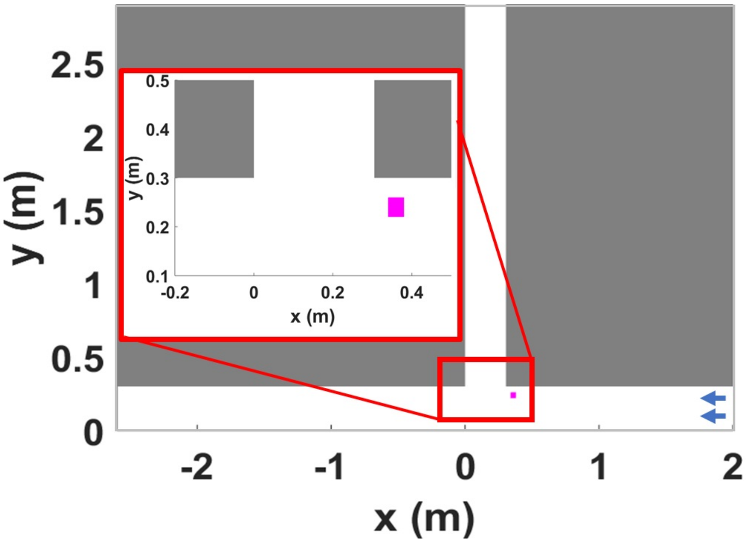

Figure 5.4: *T-junction spatial domain showing the main (white horizontal band) and the lateral (white vertical band) branches, and the upstream inflow (blue arrows) from the east of the main branch. The insert plot (red box) contains the zoomed-in view of the small obstacle position (magenta square) near the T-junction.*

FV2 streamlines, albeit with two distinct eddies formed in the backwater zone close to flume walls. However, the DG2-NL streamlines show chaotic distribution patterns with extensive spread of noises that are manifested as eddies in the backwater zone. These noises also lead to a very turbulent wake and forms swirling eddies at the wake edge resembling vortex shedding at $t = 10$ s. The analysis of the streamlines imply that the DG2-NL can lead to misleading 2D velocity predictions and should be avoided when modelling 2D velocity fields. Besides, for this 10 s simulation, the DG2-NL is 3 times more expensive to run than the DG2-LL because of the need to adopt increasingly smaller time-step (impacted by the noises). Instead, the DG2-LL seems a more reliable option for applications that require detailed capturing of 2D velocity fields, even with very smooth subcritical flow as demonstrated next.

5.3.2 Flow separation at a T-junction

This test case involves mainstream subcritical flow separated into the lateral branch of a right-angled T-junction, and is run to examine further the performance of DG2-LL and DG2-NL in producing spatial 2D velocity fields and the lateral profiles from experimental observation

(Bazin 2013, Bazin et al. 2017, Mignot et al. 2013). Two configurations are considered, as shown in Fig. 5.4: one without a 5 cm square obstacle located in the main branch, which represents a classical flow diversion into the lateral branch where the velocity field becomes more complex, and another with the obstacle that would also affect the velocity field in the main branch. For both configurations, a steady inflow discharge of 0.002 $\mathrm{m}^3\mathrm{s}^{-1}$ is considered, associated with a Froude number of 0.23, entering the main branch from the eastern boundary. Fixed water depths of 45.1 mm and 44.6 mm from Bazin (2013) are imposed at the end of the downstream and the lateral branches, respectively. The bed surface is flat and smooth with a roughness value of $n_M = 0.01$ $\mathrm{m}^{1/3}\mathrm{s}^{-1}$, which is within the range of roughness values measured in the laboratory experiment. The simulations are run on a mesh with grid size of 0.005 m, which is the finest size used by the 2D-SWE models in Bazin et al. (2017), until steady-state was reached. Simulations are performed for each of the configurations using the MUSCL-FV2, DG2-LL and DG2-NL solvers, and analyses were conducted by considering the streamlines produced from the simulated 2D velocity fields, and by comparing the components of the simulated spatial velocity profiles with the available experimental data.

For the no-obstacle configuration, the extracted streamlines shown in Fig. 5.5 indicate that, with all solvers, the mainstream flow is characterised by a region of separation along the eastern bank of the lateral branch. Within this region, MUSCL-FV2 streamlines exhibit a large flow recirculation centred close to the entrance of the lateral branch with regular, semi-elliptical patterns that narrows further downstream. In contrast, the DG2-LL and DG2-NL streamlines exhibit more uneven recirculation patterns, but resemble the measured flow recirculation pattern presented by Bazin et al. (2017), which is also quite uneven. Both the DG2-LL and DG2-NL streamlines also indicate a sequence of small-scale eddies within the inner zone of the recirculating flows, which is not observed with the MUSCL-FV2 streamlines. A major difference between the velocities predicted by DG2-LL and DG2-NL can, however, be observed for the u- and v-velocities extracted at the location $x = 0.15$ m near the entrance of the lateral branch. In Fig. 5.6, the corresponding velocity profiles are compared against the available experimental profiles of Bazin et al. (2017) . The DG2-NL profiles exhibit sharp

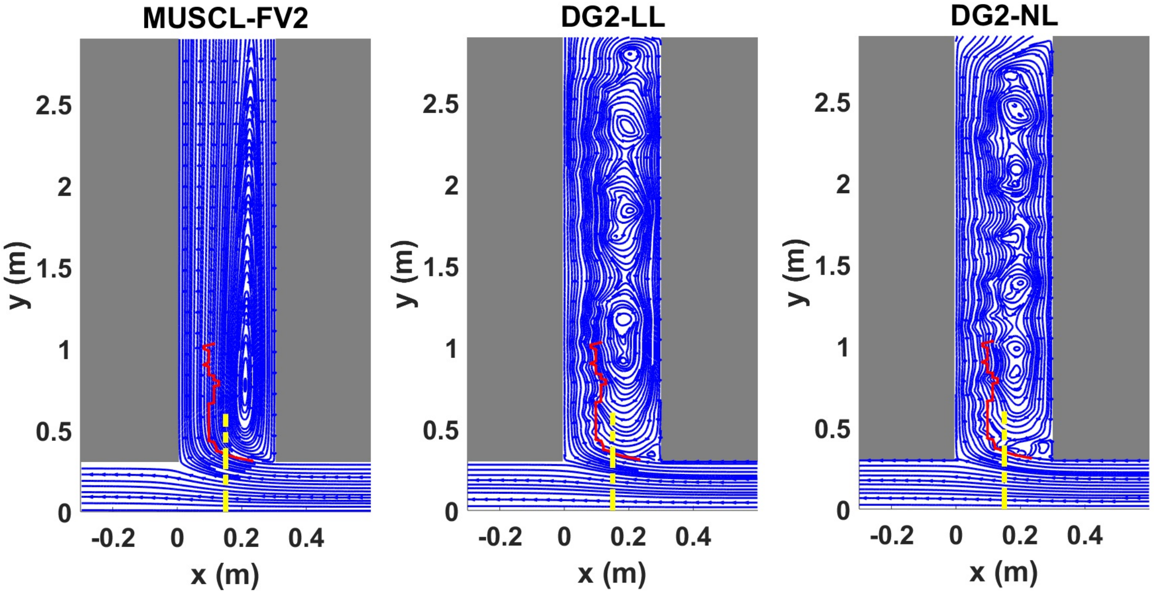

Figure 5.5: *Streamlines of the 2D velocity fields obtained with MUSCL-FV2 (left), DG2-LL (middle) and DG2-NL (right). In each subpanel, the measured recirculation extent in the lateral branch (red line) and the location of the extracted u-velocity and v-velocity at $x = 0.15$ m (yellow dashed line) for the case without the obstacle are also shown.*

wavy patterns that are more apparent in the v-velocity profile, where a very sharp dip is predicted just after the entrance of the lateral branch ($0.3 \text{ m} \leq y \leq 0.6 \text{ m}$), suggesting the presence of a negative spurious velocity component. Such a deficiency is confirmed by the fact that the DG2-NL generates the smallest R^2 correlation coefficient and the largest L^1-norm error, hence providing the least correlated and the most deviated predictions with respect to the experimental velocity profiles. In contrast, the profile of the DG2-LL velocity fields is much smoother and fits significantly better with the experimental velocity data and those extracted from MUSCL-FV2. These analyses confirm that the DG2-LL solver is a better alternative to the DG2-NL to capture complex 2D velocity fields more reliably even when these fields occur under a subcritical flow regime with a low Froude number.

Similar analyses are presented for the results obtained from the MUSCL-FV2, the DG2-NL and the DG2-LL solvers using the configuration that included the obstacle upstream of the T-junction. The extracted streamlines are shown in Fig. 5.7, which clearly indicates more complex velocity fields behind the obstacle in the main branch. The MUSCL-FV2 streamlines

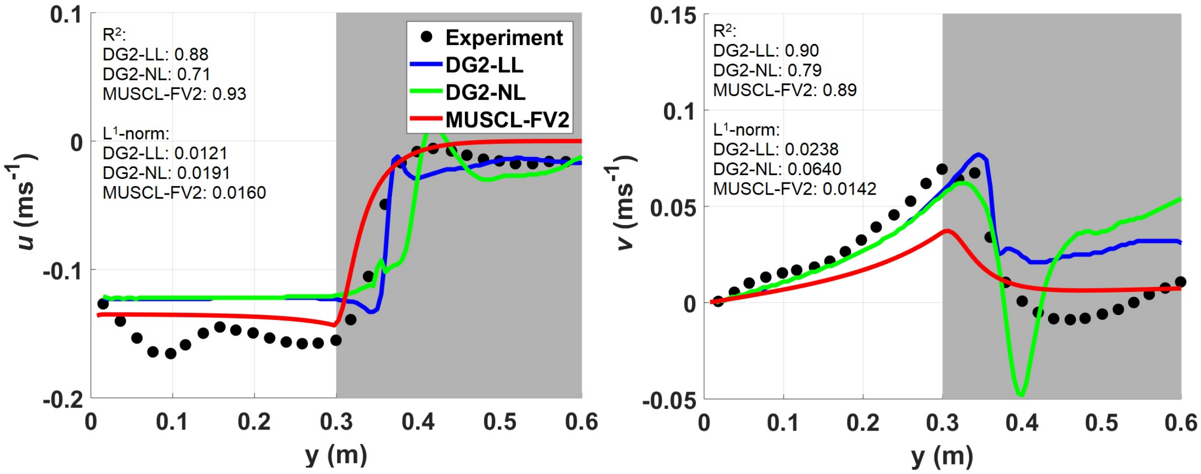

Figure 5.6: *Lateral profiles of the u-velocity (left) and v-velocity (right) from the MUSCL-FV2 (red line), the DG2-LL (blue line) and the DG2-NL (green line) solvers at $x = 0.15$ m, alongside the measured velocities (black dots) for the case without the obstacle. The R^2 and L^1-norm errors calculated along the lateral branch in each profile are also provided.*

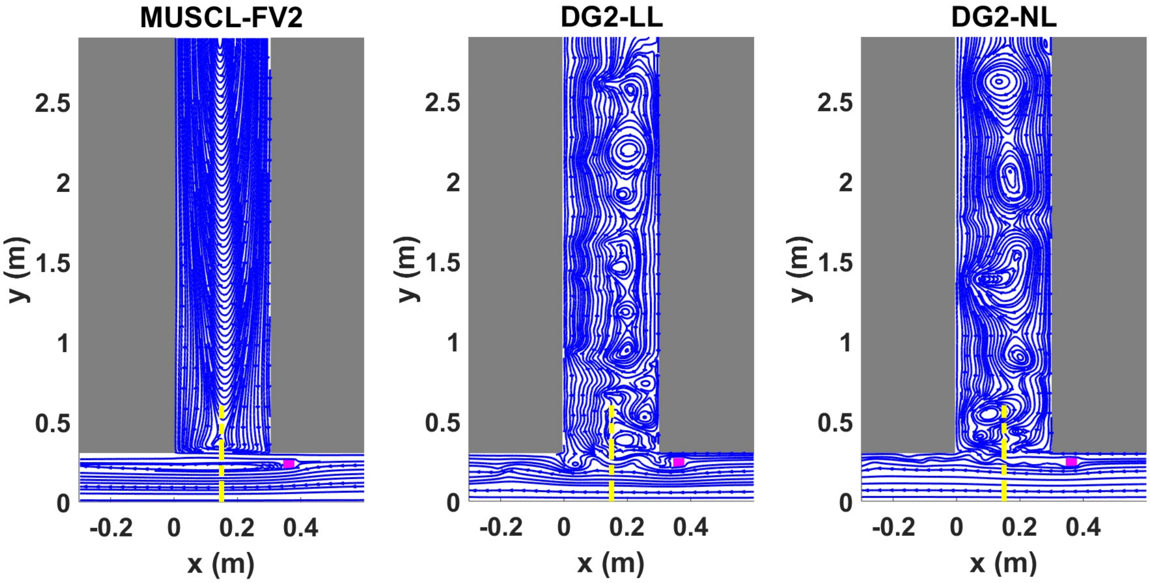

Figure 5.7: *Streamlines of the 2D velocity fields obtained with the MUSCL-FV2 (left), the DG2-LL (middle) and the DG2-NL (right) solvers for the case with the obstacle (magenta square). In each subpanel, the location of the extracted u-velocity and v-velocity at $x = 0.15$ m (yellow dashed line) is also shown.*

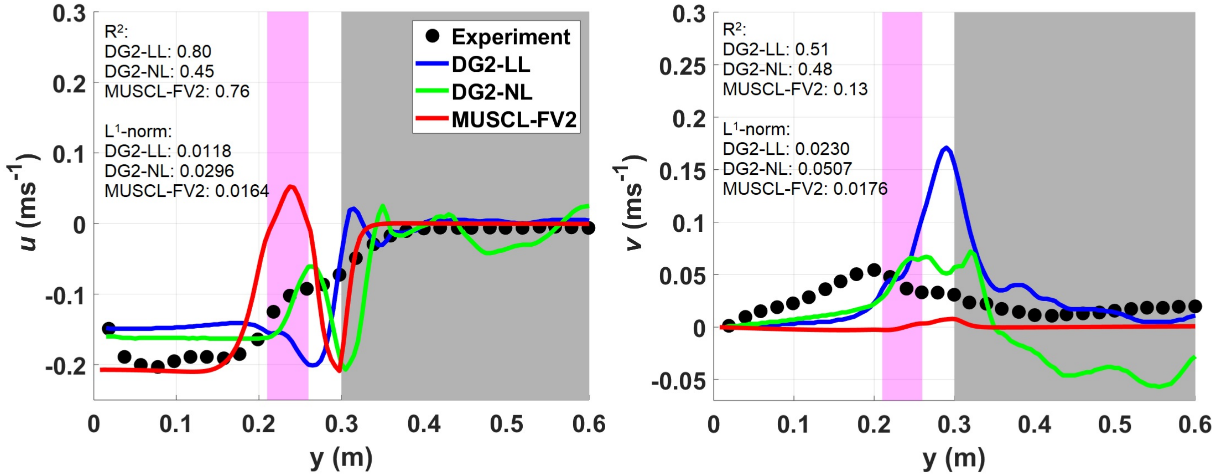

Figure 5.8: *Lateral profiles of the u-velocity (left) and v-velocity (right) for the MUSCL-FV2 (red line), the DG2-LL (blue line) and the DG2-NL (green line) solvers at x = 0.15 m, alongside the measured velocities (black dots) for the case with the obstacle (magenta square). The R^2 and L^1-norm errors calculated along the lateral branch in each profile are also provided.*

exhibit a wake behind the obstacle with smooth recirculation flows extending downstream. This wake deflects the mainstream flow to the downstream part of the main branch, and thus effectively expands the recirculating flows in the lateral branch. The DG2-NL streamlines also display a wake behind the obstacle, but this is much smaller and cleared of any streamline, which suggests the presence of a ”stagnant” zone (i.e. a zero velocity region). This smaller wake allows some of the mainstream flow to separate and form small-scale eddies within the lateral branch, which tend to progressively become more enlarged further downstream. In contrast, the DG2-LL streamlines do not show any wake behind the obstacle, suggesting that this solver can predict more mainstream flow separating into the lateral branch with a series of smaller-scale eddies that propagate along the eastern bank of the lateral branch.

Fig. 5.8 includes the lateral profiles of the u- and v-velocities predicted by the MUSCL-FV2, DG2-LL and DG2-NL solvers at $x = 0.15$ m. Because of the complexity of the flow patterns, neither the MUSCL-FV2 nor the DG2 solvers can produce profiles that capture the velocity profiles observed experimentally within the main branch (0 m $\leq y \leq$ 0.3 m). This means that the velocity fields in this region are too complex to be captured by the depth-averaged assumption featured in 2D SWE-based models without adding a turbulence closure or an eddy viscosity component (Bazin et al. 2017). Conversely, in the lateral branch, the u-velocity profiles from the MUSCL-FV2 and the DG2 solvers are comparatively more consistent with the experimental velocity data. Slight discrepancies are seen in the v-velocity profiles, in which DG2-NL yields the most deviated and least correlated predictions (compare R^2 coefficients and L^1-norm errors in Fig. 5.8). As supported further by the findings from Fig. 5.7 and Fig. 5.8, the DG2-LL is recommended for use when the aim of the application is focused on high-resolution analysis of spatial velocity fields that would be affected by the presence of sharp topographic edges, such as river groynes and building cavities.

5.3.3 Quasi-steady flow in sharp building cavities

In this test, the ability of the DG2-LL to produce more reliable spatial velocity fields is further examined by applying it to replicate high-resolution experimental data of 2D velocity fields. These data are obtained from particle image velocimetry (PIV) measurements performed in a physical model in the University of Sheffield involving one of the parking lots configurations with a closed manhole (Rubinato et al. 2021). The configuration is illustrated in Fig. 5.9, and installed on top of an existing experimental flume (Rubinato 2015). The flume slopes at 0.001 m/m and has a smooth surface (n_M = 0.011 $\mathrm{m^{1/3}s^{-1}}$), where a quasi-steady flow develops. The flow is driven by an inflow characterised by skewed velocities, which are extracted from the measured 2D velocity fields along the flume's southern boundary (red box, Fig. 5.9). At the northern boundary of the flume, free outflow conditions are imposed. DG2-LL and MUSCL-FV2 are run on a mesh with a grid size of 0.016 m, which matches the resolution of the PIV data. Simulated 2D velocity fields are extracted every 10 s and contrasted against the measured velocity fields based on the L^1-norm error.

The time histories of the L^1-norm errors, up to 350 s, are illustrated in Fig. 5.10, for the DG2-LL and the MUSCL-FV2 solvers in order to analyse the runtime costs in producing the least deviated 2D velocity fields predictions. A sharp decrease in L^1-norm errors is observed with both solvers in the first 20 s of the simulation. After then, a further decrease in the L^1-norm error is noted for the DG2-LL solver that stabilises from 40 s onwards, suggesting

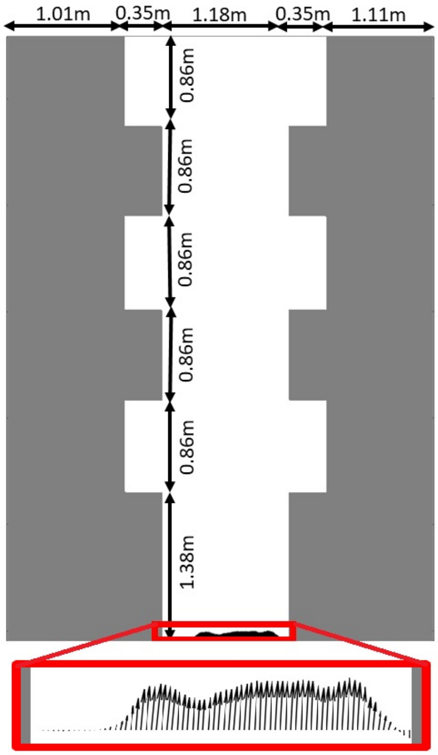

Figure 5.9: *The test configuration involving the large buildings (grey area) and side cavities. The black arrows in the red box indicate the inflow velocities extracted from the PIV-measured velocity fields along the southern boundary of the flume.*

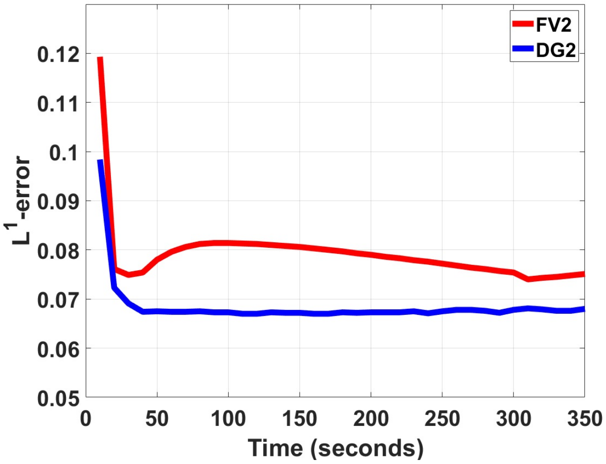

Figure 5.10: *The time history of L^1-norm errors based on the velocity fields produced by MUSCL-FV2 (red line) and DG2-LL (blue line) up to $t = 350$ s.*

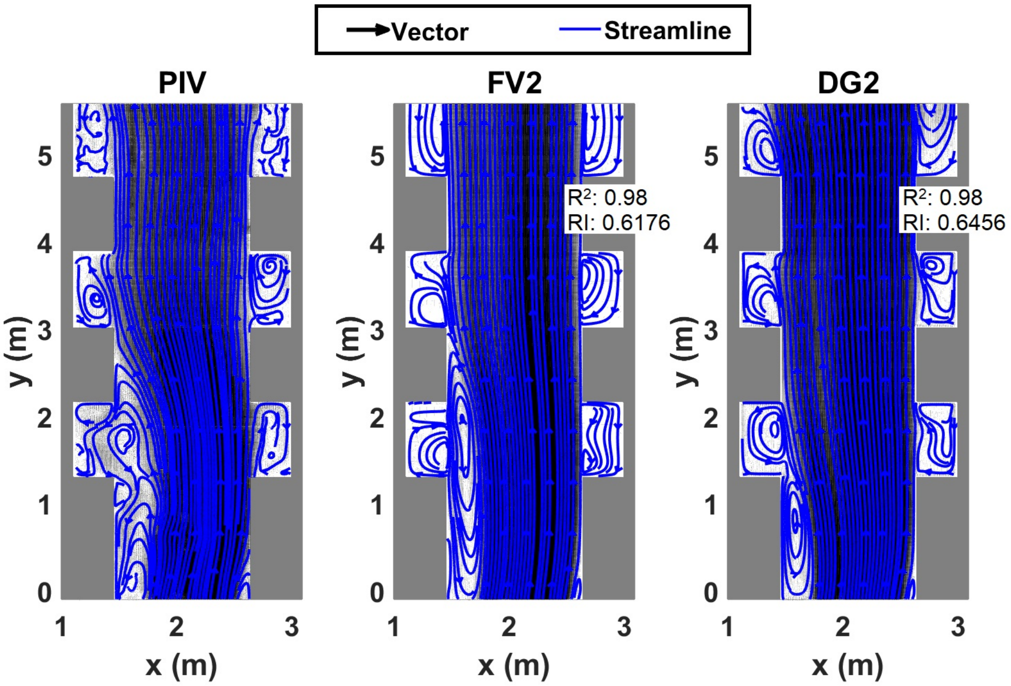

Figure 5.11: *Spatial vectors and streamlines of 2D velocity fields obtained from the PIV data (left), MUSCL-FV2 (middle) and DG2-LL (right) at t = 350 s with their respective R^2 and RI coefficients.*

that any 2D velocity prediction by this solver has the least deviation from the measured velocity fields after 40 s. In contrast, the MUSCL-FV2 solver seems to require at least 300 s of simulation time for the L^1-norm error to stabilise at values that result slightly larger than for the DG2-LL. Overall, the L^1-norm error analysis indicates that in order to predict the closest possible velocity fields to the experimental data, the MUSCL-FV2 solver should be around 7.5 times more expensive to run than the DG2-LL. Even at that cost, the MUSCL-FV2 results are not as accurate as those of the DG2-LL, as discussed next.

Fig. 5.11 displays the spatial vector map and its corresponding streamlines extracted from the 2D velocity fields experimentally measured using the PIV, compared to those predicted by the MUSCL-FV2 and the DG2-LL at $t = 350$ s. The spatial vector maps distinguish the regions of higher velocities, indicated by darker vector shades, to those with lower velocities, with much lighter vector shades. In the main channel, both DG2-LL and MUSCL-FV2 streamlines show consistently linear patterns that are relatively like the PIV streamlines in the high velocity region (darker vector shades), except near the upstream cavity of the left building where the velocities are low (lighter vector shades). Here, the extent of the recirculation flow region predicted by MUSCL-FV2 is strongly similar to those of the PIV but containing an overly elongated main channel eddy, with slightly underpredicted centre and position of the eddy in the upstream cavity of the left building. In contrast, DG2-LL streamlines replicates relatively well the main channel eddy's centre and the location of the upstream cavity's eddy, but with much smaller extent of the recirculation flow region. The observation on MUSCL-FV2 and DG2-LL streamlines shows that neither of the solvers can entirely capture recirculation flows in this region, highlighting the limitation of a 2D depth-averaged solvers in capturing complex 3D flows resulting from highly dynamic interactions of the eddies with the sharp edges of the upstream cavity. However, in low velocity region near the southern edge of the left middle cavity and near the northern edge of the right middle cavity, the DG2-LL solver perform much better in replicating the recirculation patterns of the eddies. The similarities between the streamline patterns of the DG2-LL and PIV-measured velocities can be quantitatively confirmed by particularly analysing the RI coefficient, instead of R^2, for which the solver yields a stronger fit in terms of both the magnitude and the directionality of the measured velocity fields. It is also worth noting that there could be some uncertainties present, particularly in the inflow data, that can affect the accuracy of the velocity fields obtained from the PIV measurements. Despite this limitation, the results of this test case and the previous one highlight the potential of applying the DG2-LL to produce more detailed and reliable velocity fields of quasi-steady flows and at a fraction of the computational cost.

5.3.4 Flooding in an urban residential area

This test further investigates the DG2-LL capabilities to reproduce spatial velocity fields measured in a physical model for a flash flooding that spreads over an urban residential area with buildings on small piers. The physical model was developed by Smith et al. (2016) and consisted of a 12.5 m long and 5 m wide prototype representing the Morgan-Selwyn

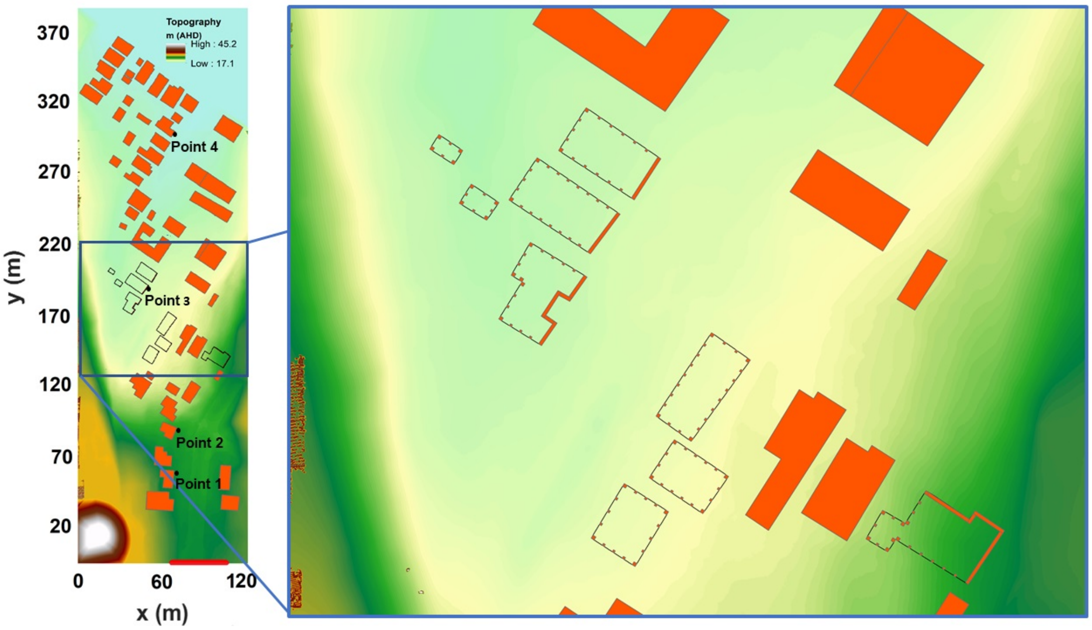

Figure 5.12: *The left panel illustrates the DEM of the Morgan-Selwyn floodway prototype, and includes the outlines of the buildings on piers (black boxes), water level sampling points (black dots) and the inflow boundary (red line, bottom of the panel). The blue box on the right provides a zoomed-in view of the walls and piers within the piered buildings (right panel).*

floodway in Merewether, Australia, to recreate the flooding scenario that occurred during the ‘Pasha Bulker’ storm. A steady-state inflow discharge of 19.7 m^3s^{-1}, which is the estimated peak flood discharge from the ‘Pasha Bulker’ storm, flows through a 38 m opening located at the southern boundary (red line, Fig. 5.12). This inflow propagates over the initially-dry topography that is constructed using road base materials. Free outflow conditions are imposed across the downstream boundary located at the north and wall boundary conditions are specified elsewhere. For the numerical model simulations, topographical survey points collated from the prototype are used to generate a digital elevation model (DEM) with a very fine grid size of 1 cm. This DEM is then resampled at a grid size of 17.5 cm (Ayog & Kesserwani 2021), in which square blocks with sizes of 52 cm for the corner piers and 35 cm for the side piers are added, as shown in Fig. 5.12. The dimensions of these piers are estimated by measuring the piers in the photographs provided in Smith et al. (2016). These piers are assumed to be unsubmerged along with other non-piered building blocks in the

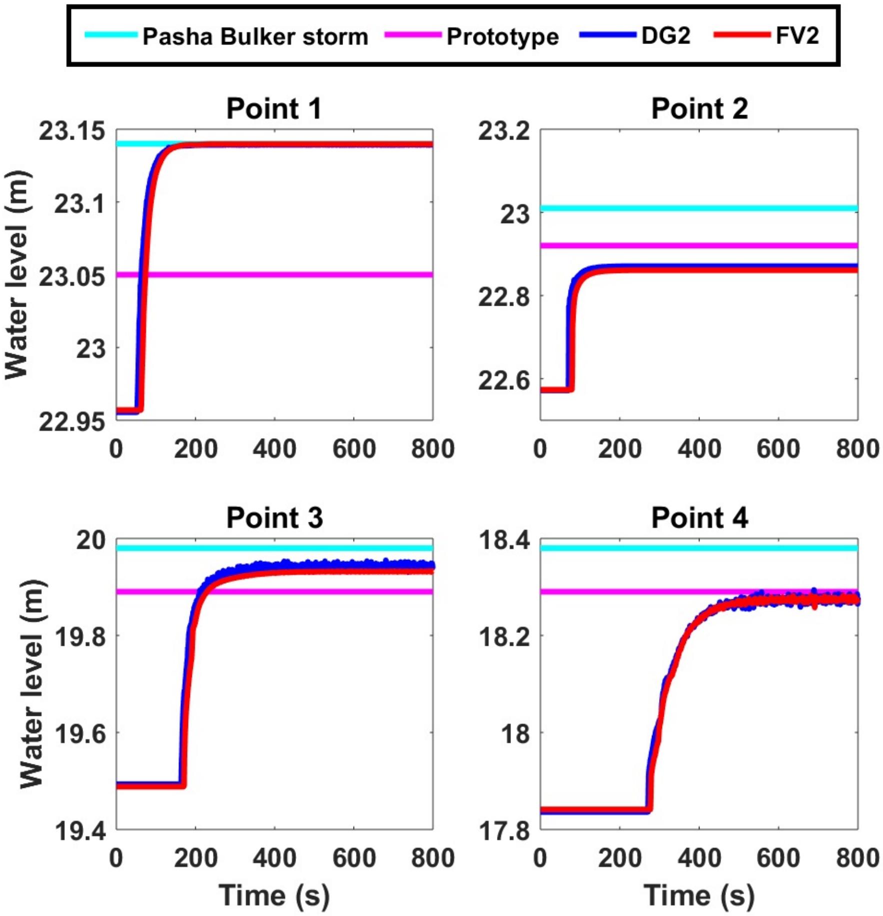

Figure 5.13: *The time histories of the water levels predicted by the DG2-LL and the MUSCL-FV2 solvers at all sampling points up to t = 800 s, alongside the historical flood levels records of the Pasha Bulker storm and the measured water level of the floodway prototype (Smith et al. 2016).*

prototype. The flood simulations are run at the resampled DEM grid size up to t = 800 s at which steady state is reached at sampling point 4 located downstream of the piered buildings (left panel, Fig. 5.12).

As recommended by Smith et al. (2016), the optimal roughness value, of $n_M = 0.042$ m$^{1/3}$s^{-1}, is calibrated by running both the MUSCL-FV2 and the DG2-LL solvers so as to closely reproduce the historical water level records of the 'Pasha Bulker' storm and the measured water levels of the prototype. Fig. 5.13 contains the associated time histories of the water level predicted by the MUSCL-FV2 and the DG2-LL solvers for this roughness value at

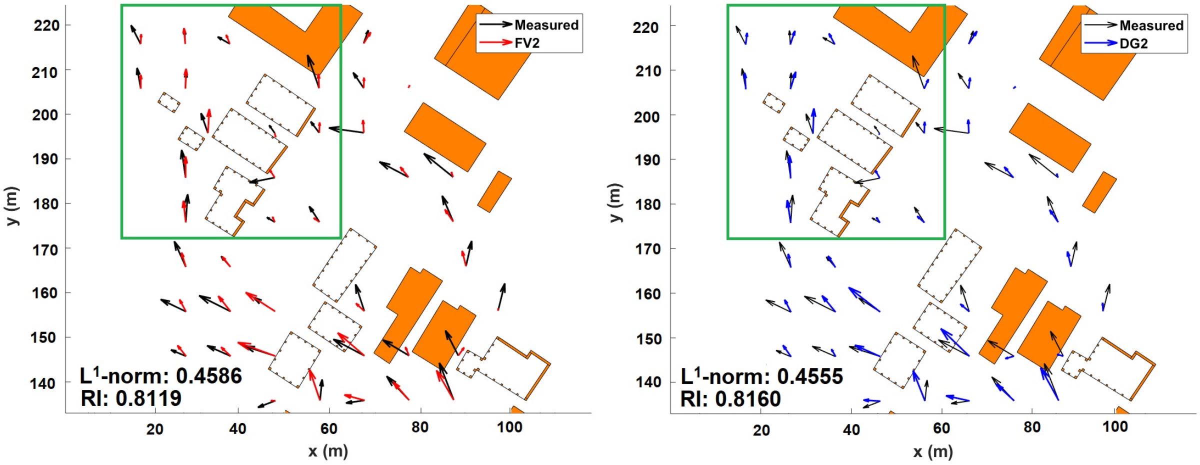

Figure 5.14: *The spatial vectors of the MUSCL-FV2 (left panel) and DG2-LL (right panel) velocity fields around the piered buildings at t = 800 s against the measured velocity vectors. The RI coefficient and L^1-norm errors are provided in each panel. The green boxes indicate the region where the streamlines of 2D velocity fields around the northwest piered buildings are analysed.*

the four sampling points shown in Fig. 5.12. It can be seen that the water level predictions by both solvers are in a good agreement with the measured water levels (maximum discrepancy of 0.1 m) and do not exceed the historical flood levels at point 1. To validate the velocity prediction around the piered buildings, velocity vectors produced by the MUSCL-FV2 and the DG2-LL solvers at t = 800 s were extracted at a 10 m spacing over the prototype where sparsely-measured velocity fields are available. Fig. 5.14 shows the velocity fields predicted by the solvers and the measured velocity vectors. Both solvers can effectively capture the sparsely-measured velocity fields within the region where the piered buildings are located. However, the DG2-LL solver yields slightly higher RI and lower L^1-norm error, indicating a better alignment with the measured velocity vectors.

A more detailed investigation of the local distribution of the velocity fields around the piers is conducted by analysing the streamlines of the MUSCL-FV2 and the DG2-LL fine-resolution velocity predictions at t = 800 s. Only zoomed-in portions are considered for the northwest piered buildings (green box, Fig. 5.14) where the flood wave interactions with the piers are more complex as shown in Fig. 5.15. The streamline plots indicate that the MUSCL-FV2 solver predicts chaotic recirculation patterns forming behind the front walls of buildings

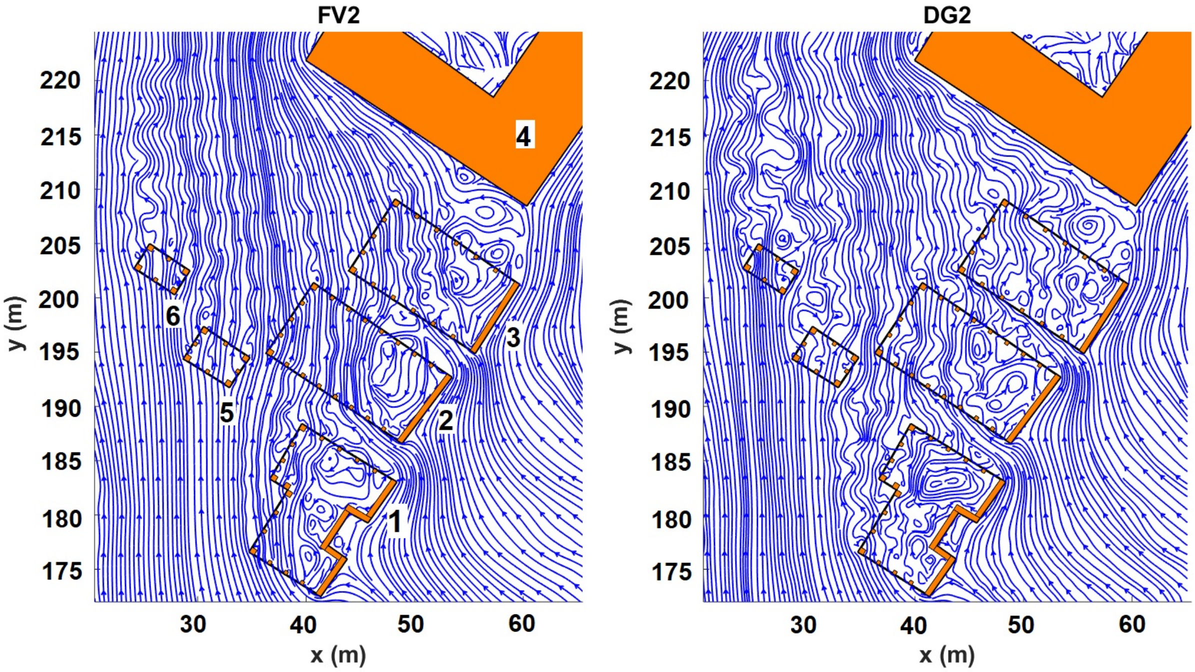

Figure 5.15: *The streamlines extracted from the MUSCL-FV2 (left panel) and the DG2-LL (right panel) velocity fields around the northwest piered buildings at t = 800 s. The building numbers are provided in the left panel.*

1, 2 and 3. Similar recirculation patterns are also observed in the DG2-LL streamlines, but these are characterised by smaller-scale eddies coinciding with those observed previously with the DG2-LL in the flow separation region in the previous T-junction test. The DG2-LL also produces relatively irregular streamlines downstream of the back piers of buildings 2 and 3, which are less smooth than the MUSCL-FV2 streamlines. Additionally, the DG2-LL streamlines exhibit larger swirling patterns with eddies around piers southwest of building 1 and north of buildings 5 and 6. Hence, the analysis of the streamlines indicate that the DG2-LL solver can provide more precise velocity fields, and allows to gain a better insight on the localised flow patterns and (re)distributions around small topographical structures, such as when modelling flooding around piered buildings.

5.4 Concluding remarks

This chapter has demonstrated the capabilities of a second-order discontinuous Galerkin (DG2) solver in reproducing detailed velocity fields when solving the depth-averaged shallow water equations without an eddy viscosity or turbulence term. These capabilities were investigated over four selected test cases for two DG2 variants with and without slope limiting, and by comparing their velocity predictions against those produced by the commonly used MUSCL-FV2 solver. The selected test cases required detailed capturing of small-scale velocity transients, at sub-metre scale, that occur at zones where the waves interact with steep topographies, for different flow conditions ranging from rapidly propagating transient flow to steady subcritical flow across a junction structure, within building side cavities, and behind small building piers. The solver predictions were compared using quantitative metrics and qualitative analysis of the predicted streamline at the zones of the recirculating flows. Performance analyses revealed that local limiting with the DG2 solver is needed to produce reliable velocity field predictions at sub-metre resolution even when the flow is subcritical and steady. Within this configuration, the DG2 solver is able to capture small-scale recirculation eddies in the velocity field prediction that are otherwise smeared out by the MUSCL-FV2 solver. Furthermore, the DG2 solver is more efficient than MUSCL-FV2, in the sense that it is much faster (around 7.5 times) to deliver the required steady state velocity predictions. These findings offer strong evidence that the DG2 solver is a valuable alternative to FV2 modelling, when detailed velocity fields are required within regions of wave-structure interactions, and without the need of additional mathematical complexity beyond the standard shallow water equations.

Chapter 6

Conclusions

In this concluding thesis chapter, a summary of the PhD research is provided in Sec. 6.1. Here, the key findings associated with the achievement are also discussed along with the research limitations. The significance of these findings to the current gaps of practical flood modelling applications is then briefly explained in Sec. 6.2, followed by some recommendations for potential future research in Sec. 6.3.

6.1 Summary of the thesis

The background of this research has been elucidated in the Chapter 1, in which the advantages and limitations of the finite volume 2D-SWE solvers adopted in industry-standard flood modelling applications have been discussed. An alternative to the industry finite volume solvers, namely the DG2 solver, is seen to have the capabilities to improve these flood modelling software packages, however it is rarely been explored for such application, even more so for industrial modelling practices. The exploration on the capabilities of the DG2 solver in flood modelling may have been discouraged by the fact that this solver, in its standard formulation, entails very long runtime due to its high mathematical complexity, added with the complications on ensuring conservation properties and stability are met when steep topographic structures are present. These challenges uncovered the opportunity to develop a novel 2D-SWE flood model based on a simplified DG2 solver that can implemented for practical flood inundation modelling, which serves as the main aim of this PhD research.

Based on this research aim, three objectives have been formed. The first objective, which is to develop and assess the performance of the simplified 2D-SWE DG2 model relative to the standard DG2 model, has been addressed and discussed in Chapter 3. In this chapter, the differences between these two DG2 formulation were analysed, and further investigation was later done on the simplified DG2 formulation considering two different topography discretisation. The capabilities of the simplified and standard DG2 formulation were compared against test cases that assess their 2D flow characteristics and shock-capturing ability in a radial dam-break on a flat bed. Another set of test cases was selected to analyse conservative properties relating to the well-balanced properties and accuracy of the simplified 2D-SWE DG2 solver over different types of topography and moving wetting and drying in a parabolic bowl.

The second objective, which is to assess the performance of the simplified DG2 solver relative to well-established FV-based software packages that commonly used for industry-scale modelling applications, has been addressed and studied in Chapter 4. Concurrently, the viability of using the simplified 2D-SWE flood model for this scope of applications is also studied and verified. In this chapter, the main similarities and differences between the simplified DG2 solver and the FV-based solvers (i.e. FV1 and MUSCL-FV2 solvers) were detailed, followed by an analytical assessments of the solvers' conservative properties of mass and energy over long simulation period and with two grid resolutions. Comparative analyses were later done on the outputs of the simplified DG2 flood model against those from four prominent FV-based industrial models (i.e. TUFLOW-FV1, TUFLOW-FV2, TUFLOW-HPC and Infoworks ICM) for the same resolution as the industrial models using six benchmark test cases published by the UK Environment Agency. Using the same tests, the simplified DG2 model was further analysed at twice-coarser resolution and compared to the outputs of an in-house MUSCL-FV2 model. The analyses were done quantitatively and qualitatively with respect to a reference solution that were either produced by running MUSCL-FV2 on the finest DEM resolution or by using available experimental data.

Finally, the third objective, which is to identify suitable settings for the simplified 2D-SWE DG2 model for different flood modelling applications, has been addressed in both Chapter 4 and Chapter 5. These settings are specifically relevant to the applicability of the local slope limiting within the simplified DG2 model considering flood modelling applications that are of catchment- and regional-scale with grid resolutions more than 5 m (Chapter 4), or of small-scale flooding in urbanised environment that is modelled at sub-meter resolution (Chapter 5). In particular, Chapter 5 is dedicated to explore the capabilities of the simplified 2D-SWE DG2 model in producing detailed spatial velocity fields with small-scale eddies in regions of wave-structure interactions without an eddy viscosity or turbulence term. Such capabilities are explored against a MUSCL-FV2 model over four test cases with experimental velocity fields, for different flow conditions across multiple building blocks, a junction structure, around building side cavities and for a real-world flooding scenario in an urban residential area.

The codes and data used in this thesis can be accessed in https://doi.org/10.5281/zenodo.5921132.

6.1.1 Key findings and limitation of the research

The achievement of the research objectives discussed earlier unfold the following key findings of the research:

The achievement of first objective revealed that the simplified DG2 formulation, which relies on the slope-decoupled discretisation based on the stencil in Fig. 3.2, reduces the amount of mathematical evaluations and operations from 32 to 12 when compared to the standard formulation. This in return allows the simplified DG2 formulation to provide runtime speed up by around 2.6 times per flow variable. Despite producing errors that are slightly larger than the standard formulation, the simplified DG2 formulation can equally deliver predictions at second-order accuracy and adequately track the evolution of the shock and rarefaction waves of a rapid dam-break. By employing the slope-decoupled approach to discretise the bed topography, the simplified DG2 formulation is able to fully ensure that the well-balanced properties are preserved for both mean and slope coefficients, and over smooth and steep topography shapes. Such capability along with the ability to retain second-order accurate predictions when subjected to constant wetting and drying processes on uneven topography, validates the simplified DG2 formulation to be further developed into a 2D-SWE flood model for practical modelling applications.

The achievements of the second and third objectives signify that a grid-based flood model based on simplified 2D-SWE DG2 solver is stable and robust to be applied for industry-standard and real-world modelling applications. It can significantly resist numerical dissipation for long simulation period compared to the FV-based solvers due to its better energy conservation property, and it is less sensitive to grid coarsening. For spatial scope covering a large catchment or a whole region with the modelled grid resolution > 5 m, DG2 with no slope limiting (DG2-NL) is found to be more appropriately applied than with the local slope limiting activated (DG2-LL) as the former can be run at 1.8-2.2 times faster with reliable predictions in simulating shockless flood flows. When modelled at twice-coarser resolution, DG2-NL is able to predict close predictions to the outputs of the industrial flood models in simulating topographic-driven flood flows with high friction effects and when sampling the water level hydrograph far from the flooding source is needed. However, the more expensive DG2-LL is still required for applications when the spatial scale is smaller, such as within an urban environment with dense coverage of sharp-edged building blocks, that is modelled at sub-meter grid resolution. In such type of applications, DG2-LL is able to provide detailed capturing of small-scale temporal and spatial variations of the flows around recirculation eddies that are formed due to complex wave-structure interactions, even without eddy viscosity or turbulence term. DG2-LL can also achieve steady state velocity predictions at around 7.5 times faster than MUSCL-FV2, and can produce more reliable predictions of the localised flow patterns and distribution around small piers of urban houses during a real-world flooding event.

The limitation when conducting this research is primarily on the availability of sufficient computational resources, which is particularly crucial when simulating large-scale flooding cases with very fine grid resolution (such as in modelling spatial velocity fields). Whilst it is preferred that computational runtime for all test cases to be considered in this research, constant recalibration and validation of the DG2 model for each test case especially on a single CPU core computer can still be extremely time-consuming. Another research limitation identified is in the difficulty of getting data of spatial velocity fields from real-world flooding event. It is notably acknowledged that the lack of such data may be contributed to the safety concerns associated with acquiring the data during an actual flooding, so a test case such as the one based on Morgan-Selwyn floodway in Merewether, which is first simulated in a physical model (but calibrated using actual flood level), was selected instead to get the closest representation of the spatial velocity fields in a real-world flooding scenario.

6.2 Significance of research findings

The key findings of the PhD research elaborated in Sec. 6.1.1 has finally validated the potential benefits offered by simplified 2D-SWE DG2 solver as an alternative to other classical numerical 2D-SWE solvers in practical flood modelling applications, as noted by some industrial communities (Engineers Australia 2012). As the simplified DG2 flood model can produce reliable predictions at coarser grid resolutions, it may serve as a useful modelling tool to aid urban flood risk management in developing countries and data sparse localities (Nkwunonwo et al. 2020). This DG2 model, with local slope limiting, is also a viable option to higher-order FV models in applications requiring detailed capturing small eddies in turbulent flows (Özgen-Xian et al. 2021). In a larger picture, the significance of these findings indicate that this newly developed DG2 flood model can contribute to the fulfillment of Goal 11, United Nation's Sustainable Cities and Communities, in assisting mitigation and adaptation to water-related disaster globally.

6.3 Recommendations for future research

Based on the research limitation stated in Sec. 6.1.1, the following recommendations for future research can be made:

Significant improvement can be made on the computational efficiency of the DG2 and MUSCL-FV2 solvers using CPU and GPU parallelisation technologies. Recently, these solvers have been embedded in LISFLOOD-FP modelling package which can be run on parallelised computing techniques. With this advantage, more assessment can be made on the computational runtimes and efficiencies between these two solvers considering real-world flooding events on very large and complex catchment(s) or on very fine grid resolutions around steep building or topographic structures, that may take days or months to simulate on a single CPU core computer.

The ability of the DG2 model (with local limiting) in producing spatial velocity fields with fine-scale recirculation eddies brings out other possibilities to analyse the applicability of the DG2 model for non-flood modelling applications, such as in the assessments relating to enviromental flows and sediment transport. For such applications, a comparative assessment between the DG2 and higher-order FV-based model may be able to illustrate the advantages (or limitations) of the DG2 model in capturing details of recirculation flows. In certain flow conditions, eddy viscosity or turbulence term may not be avoidable especially in highly turbulent flows, thus future investigation on how eddy viscosity improves the velocity field predictions of the DG2 model is highly recommended.

Appendix A

Before demonstrating why the proposed alternative topography projection is required to ensure complete well-balancedness of the simplified 2D-SWE DG2 solver for the mean and slope coefficients, a demonstration of the well-balanced properties of the DG2 solver is first considered for 1D case, shown in the following section.

Demonstration of well-balanced properties in a 1D case

As a background, the system of Eq. 3.1 becomes Eq. A.1 for the 1D case considering the variables in Eq. A.2:

$$\partial_t \mathbf{U} + \partial_x \mathbf{F}(\mathbf{U}) = \mathbf{S}(\mathbf{U}) \tag{A.1}$$

$$\mathbf{U} = \begin{bmatrix} h \\ q_x \end{bmatrix}, \quad \mathbf{F} = \begin{bmatrix} q_x \\ \frac{q_x^2}{h} + \frac{g}{2}h^2 \end{bmatrix}, \quad \text{and} \quad \mathbf{S} = \begin{bmatrix} 0 \\ -gh\partial_x z \end{bmatrix} \tag{A.2}$$

In such case, the simplified DG2 space operators are reduced to:

$$\mathbf{L}_c^0 = -\frac{1}{\Delta x}(\widetilde{\mathbf{F}}_E - \widetilde{\mathbf{F}}_W) + \mathbf{S}(\mathbf{U_h}(x_c, t)) \tag{A.3a}$$

$$\mathbf{L}_c^{1x} = -\frac{3}{\Delta x}\left\{(\widetilde{\mathbf{F}}_E - \widetilde{\mathbf{F}}_W) - (\mathbf{F}(\mathbf{U_h}(G_{x2},t)) + \mathbf{F}(\mathbf{U_h}(G_{x1},t)) \right.$$
$$\left. -\frac{3}{\Delta x}\left[\mathbf{S}(\mathbf{U_h}(G_{x2},t)) - \mathbf{S}(\mathbf{U_h}(G_{x1},t))\right]\right\} \tag{A.3b}$$

A DG2 solver is deemed able to preserve well-balancedness when it could achieve the still water motionless condition over an uneven topography for a long time (Duran & Marche 2014), for which the initial conditions are:

$$h + z = \textbf{constant} \quad \text{and} \quad q_x = 0 \tag{A.4}$$

The condition, $h + z = \textbf{constant}$ is particularly true at the local discrete level, that is for all grid elements Q_c given the continuity of z_h as per Eq. 3.27:

$$(h + z)_h = h_h + z_h = \textbf{constant} \tag{A.5}$$

After the application of depth-positivity preserving reconstructions at the eastern and western interfaces, the discrete still water in Eq. A.5 can be expressed as:

$$\overline{h}_c^{1x} + \overline{z}_c^{1x} = 0 \tag{A.6a}$$

$$\overline{h}_c^{0} = \frac{h_E^{-,*} + h_W^{+,*}}{2} \quad \text{and} \quad \overline{h}_c^{1x} = \frac{h_E^{-,*} - h_W^{+,*}}{2} \tag{A.6b}$$

$$\overline{z}_c^{1x} = \frac{z_E^{*} - z_W^{*}}{2} \tag{A.6c}$$

The local (i.e. over Q_c) approximate solution $\mathbf{U_h}$ consist mainly of water depth variable h_h expressed by means of positivity-preserving coefficients (Eq. A.6b) along with the bed slope coefficients (Eq. A.6c). Terms from the flux and source vectors remain due to the hydrostatic balance equation remaining within the momentum equation (mass equation vanishes with the still water condition in Eq. A.4); they are expressed as $f(h_h) = \frac{g}{2}h_h^2$ and $s(h_h) = -gh_h\partial_x z_h|_{Q_c}$ considering the coefficients in Eq. A.6 and Eq. 3.27.

Under the still water condition, with $\tilde{f}(h_E^{-,*}) = \frac{g}{2}(h_E^{-,*})^2$ and $\tilde{f}(h_W^{-,*}) = \frac{g}{2}(h_W^{+,*})^2$, the difference and sum of the Riemann flux evaluations can be manipulated to:

$$\tilde{f}(h_E^{-,*}) - \tilde{f}(h_W^{+,*}) = \frac{g}{2}[(2\overline{h}_c^{0})(2\overline{h}_c^{1x})] \tag{A.7a}$$

$$\tilde{f}(h_E^{-,*}) + \tilde{f}(h_W^{+,*}) = \frac{g}{2}[2(\overline{h}_c^{0})^2 + 2(\overline{h}_c^{1x})^2] \tag{A.7b}$$

The local volume integral of the flux term (involved in the slope spatial operator (Eq. A.3b)) becomes:

$$f(h_h(G_{x2})) + f(h_h(G_{x1})) = f\left(\overline{h}_c^{0} + \frac{\overline{h}^{1x}}{\sqrt{3}}\right) + f\left(\overline{h}_c^{0} - \frac{\overline{h}^{1x}}{\sqrt{3}}\right) = \frac{g}{2}\left[2(\overline{h}_c^{0})^2 + \frac{2}{3}(\overline{h}_c^{1x})^2\right] \tag{A.8}$$

The source term evaluations (involved in both mean and slope spatial operators in Eqs. A.3) becomes:

$$s(h_h(x_c)) = s(\overline{h}_c^{0}) = -g\overline{h}_c^{0}\left(\frac{2\overline{z}_c^{1x}}{\Delta x}\right) \tag{A.9a}$$

$$s(h_h(G_{x2})) - s(h_h(G_{x1})) = s\left(\overline{h}_c^{0} + \frac{\overline{h}_c^{1x}}{\sqrt{3}}\right) - s\left(\overline{h}_c^{0} - \frac{\overline{h}_c^{1x}}{\sqrt{3}}\right) = -g\left(\frac{2\overline{z}_c^{1x}}{\Delta x}\right)\left(\frac{2\overline{h}_c^{1x}}{\sqrt{3}}\right) \tag{A.9b}$$

The replacement of Eqs. A.7-A.9 in the spatial operators (Eqs. A.3) (for the remaining momentum terms) will produce:

$$\mathbf{L}_c^0 = -\frac{2g}{\Delta x}\left[\overline{h}_c^{0}\left(\overline{h}_c^{1x} + \overline{z}_c^{1x}\right)\right] \tag{A.10a}$$

$$\mathbf{L}_c^{1x} = -\frac{3g}{\Delta x}\left\{\frac{2}{3}\left(\overline{h}_c^{1x}\right)^2 - \frac{2}{3}\left[\left(-\overline{z}_c^{1x}\right)\left(\overline{h}_c^{1x}\right)\right]\right\} \tag{A.10b}$$

Given the slope coefficients relationship in Eq. A.6a (i.e. $-\bar{z}_c^{1x} = \bar{h}_c^{1x}$), Eqs. A.10 will then be zeroed:

$$\mathbf{L}_c^0 = -\frac{2g}{\Delta x}\left[\overline{h}_c^0\left(-\overline{z}_c^{1x} + \overline{z}_c^{1x}\right)\right] = 0 \tag{A.11a}$$

$$\mathbf{L}_c^{1x} = -\frac{3g}{\Delta x}\left\{\frac{2}{3}\left(\overline{h}_c^{1x}\right)^2 - \frac{2}{3}\left[\left(\overline{h}_c^{1x}\right)\left(\overline{h}_c^{1x}\right)\right]\right\} = 0 \tag{A.11b}$$

Demonstration of well-balanced properties in the 2D case

For the 2D case, consider again the system of Eq. 2.1 with the flow variables in Eq. A.13:

$$\partial_t\mathbf{U} + \partial_x\mathbf{F(U)} + \partial_y\mathbf{G(U)} = \mathbf{S(U)} \tag{A.12}$$

$$\mathbf{U} = \begin{bmatrix} h \\ q_x \\ q_y \end{bmatrix}, \quad \mathbf{F} = \begin{bmatrix} q_x \\ \frac{q_x^2}{h} + \frac{g}{2}h^2 \\ \frac{q_x q_y}{h} \end{bmatrix}, \quad \text{and} \quad \mathbf{S} = \begin{bmatrix} 0 \\ -gh\partial_x z \\ -gh\partial_y z \end{bmatrix} \tag{A.13}$$

The simplified DG2 spatial operators for the 2D case are as in Eqs. 3.21a-3.21c (refer also to Fig. 3.2):

$$\mathbf{L}_c^0 = -\frac{1}{\Delta x}\left(\widetilde{\mathbf{F}}_E - \widetilde{\mathbf{F}}_W\right) - \frac{1}{\Delta y}\left(\widetilde{\mathbf{F}}_N - \widetilde{\mathbf{F}}_S\right) + \mathbf{S}(\mathbf{U_h}(x_c, y_c), t)) \tag{A.14a}$$

$$\begin{aligned}\mathbf{L}_c^{1x} = -\frac{3}{\Delta x}\Bigg\{&(\widetilde{\mathbf{F}}_E + \widetilde{\mathbf{F}}_W) - (\mathbf{F}(\mathbf{U_h}(G_{x2}, t)) + \mathbf{F}(\mathbf{U_h}(G_{x1}, t))) \\ &- \frac{\Delta x\sqrt{3}}{6}\left[\mathbf{S}(\mathbf{U_h}(G_{x2}, t)) - \mathbf{S}(\mathbf{U_h}(G_{x1}, t))\right]\Bigg\}\end{aligned} \tag{A.14b}$$

$$\mathbf{L}_c^{1y} = -\frac{3}{\Delta y}\left\{ (\widetilde{\mathbf{F}}_N + \widetilde{\mathbf{F}}_S) - (\mathbf{G}(\mathbf{U_h}(G_{y2},t)) + \mathbf{G}(\mathbf{U_h}(G_{y1},t))) - \frac{\Delta y\sqrt{3}}{6}\left[\mathbf{S}(\mathbf{U_h}(G_{y2},t)) - \mathbf{S}(\mathbf{U_h}(G_{y1},t))\right] \right\} \tag{A.14c}$$

Under discrete still water conditions (i.e. $h + z = \mathbf{constant}$ and $(q_x, q_y) = 0$) and after depth positivity-preserving reconstruction, Eq. A.5 becomes:

$$\overline{h}_c^{1x} + \overline{z}_c^{1x} = 0 \quad \text{and} \quad \overline{h}_c^{1y} + \overline{z}_c^{1y} = 0 \tag{A.15a}$$

$$\overline{h}_c^{0x} = \frac{h_E^{-,*} + h_W^{+,*}}{2} \quad \text{and} \quad \overline{h}_c^{1x} = \frac{h_E^{-,*} - h_W^{+,*}}{2} \tag{A.15b}$$

$$\overline{h}_c^{0y} = \frac{h_N^{-,*} + h_S^{+,*}}{2} \quad \text{and} \quad \overline{h}_c^{1y} = \frac{h_N^{-,*} - h_S^{+,*}}{2} \tag{A.15c}$$

Now, the main variable is h_h, the mass conservation equation vanishes, and only hydrostatic balance equations remain within the momentum equations relative to both x- and y-directions.

Within these conditions, the fluxes and source terms involved in the momentum equations are:

$$\mathbf{F}(h_h) = \begin{bmatrix} \frac{g}{2}h_h^2 \\ 0 \end{bmatrix} \quad , \quad \mathbf{G}(h_h) = \begin{bmatrix} 0 \\ \frac{g}{2}h_h^2 \end{bmatrix} \quad , \quad \mathbf{S}(h_h) = \begin{bmatrix} -gh_h\partial_x z_h \\ -gh_h\partial_y z_h \end{bmatrix} \tag{A.16}$$

The difference and the sum of the Riemann fluxes become:

$$\widetilde{\mathbf{F}}(h_E^{-,*}) - \widetilde{\mathbf{F}}(h_W^{+,*}) = \frac{g}{2}\begin{bmatrix} (2\overline{h}_c^{0x})(2\overline{h}_c^{1x}) \\ 0 \end{bmatrix} \tag{A.17a}$$

$$\widetilde{\mathbf{G}}(h_N^{-,*}) - \widetilde{\mathbf{G}}(h_S^{+,*}) = \frac{g}{2}\begin{bmatrix} 0 \\ (2\overline{h}_c^{0y})(2\overline{h}_c^{1y}) \end{bmatrix} \tag{A.17b}$$

$$\widetilde{\mathbf{F}}(h_E^{-,*}) + \widetilde{\mathbf{F}}(h_W^{+,*}) = \frac{g}{2}\begin{bmatrix} 2(\overline{h}_c^{0x})^2 + 2(\overline{h}_c^{1x})^2 \\ 0 \end{bmatrix} \tag{A.17c}$$

$$\widetilde{\mathbf{G}}(h_N^{-,*}) + \widetilde{\mathbf{G}}(h_N^{+,*}) = \frac{g}{2}\begin{bmatrix} 0 \\ 2(\overline{h}_c^{0y})^2 + 2(\overline{h}_c^{1y})^2 \end{bmatrix} \tag{A.17d}$$

The volume integral of the flux term that is involved in the slope evolution operators (Eqs. A.14) become:

$$\mathbf{F}(h_h(G_{x_2})) + \mathbf{F}(h_h(G_{x_1})) = \begin{bmatrix} \frac{g}{2}\left[2\left(\overline{h}_c^{0x}\right)^2 + \frac{2}{3}\left(\overline{h}_c^{1x}\right)^2\right] \\ 0 \end{bmatrix} \tag{A.18a}$$

$$\mathbf{G}(h_h(G_{y_2})) + \mathbf{G}(h_h(G_{y_1})) = \begin{bmatrix} 0 \\ \frac{g}{2}\left[2\left(\overline{h}_c^{0y}\right)^2 + \frac{2}{3}\left(\overline{h}_c^{1y}\right)^2\right] \end{bmatrix} \tag{A.18b}$$

If considering the standard planar topography projection (i.e. $\partial_x z_h|_{Q_c} = \frac{2}{\Delta x} z_c^{1x}$ and $\partial_y z_h|_{Q_c} = \frac{2}{\Delta y} z_c^{1y}$), the source term evaluations involved in the spatial operators (Eqs. A.14) become Eqs. A.19:

$$\mathbf{S}(h_h(x_c)) = \begin{bmatrix} -g\overline{h}_c^{0x}\left(\frac{2\overline{z}_c^{1x}}{\Delta x}\right) \\ -g\overline{h}_c^{0y}\left(\frac{2\overline{z}_c^{1y}}{\Delta y}\right) \end{bmatrix} \tag{A.19a}$$

$$\mathbf{S}(h_h(G_{x2})) - \mathbf{S}(h_h(G_{x1})) = \begin{bmatrix} -g\left(\frac{2\overline{z}_c^{1x}}{\Delta x}\right)\left(\frac{\overline{h}_c^{1x}}{\sqrt{3}}\right) \\ -g\left(\frac{2\overline{z}_c^{1y}}{\Delta y}\right)\left(\frac{\overline{h}_c^{1x}}{\sqrt{3}}\right) \end{bmatrix} \tag{A.19b}$$

$$\mathbf{S}(h_h(G_{y2})) - \mathbf{S}(h_h(G_{y1})) = \begin{bmatrix} -g\left(\frac{2\overline{z}_c^{1x}}{\Delta x}\right)\left(\frac{\overline{h}_c^{1y}}{\sqrt{3}}\right) \\ -g\left(\frac{2\overline{z}_c^{1y}}{\Delta y}\right)\left(\frac{\overline{h}_c^{1y}}{\sqrt{3}}\right) \end{bmatrix} \tag{A.19c}$$

Replacing Eqs. A.16-A.19 in Eqs. A.14, considering only the remaining terms in the momentum conservation equation, the DG2 operators can be rearranged as follows:

$$\mathbf{L}_c^0 = \begin{bmatrix} -\frac{2g}{\Delta x}\left[\overline{h}_c^{0x}(\overline{h}_c^{1x} + \overline{z}_c^{1x})\right] \\ -\frac{2g}{\Delta y}\left[\overline{h}_c^{0y}(\overline{h}_c^{1y} + \overline{z}_c^{1y})\right] \end{bmatrix} \tag{A.20a}$$

$$\mathbf{L}_c^{1x} = \begin{bmatrix} -\frac{3g}{\Delta x}\left\{\frac{2}{3}(\overline{h}_c^{1x})^2 - \frac{2}{3}\left[\left(-\overline{z}_c^{1x}\right)\left(\overline{h}_c^{1x}\right)\right]\right\} \\ -\frac{g}{\Delta y}\left(\overline{z}_c^{1y}\overline{h}_c^{1x}\right) \end{bmatrix} \tag{A.20b}$$

$$\mathbf{L}_c^{1y} = \begin{bmatrix} -\frac{g}{\Delta x}\left(\overline{z}_c^{1x}\overline{h}_c^{1y}\right) \\ -\frac{3g}{\Delta y}\left\{\frac{2}{3}(\overline{h}_c^{1y})^2 - \frac{2}{3}\left[\left(-\overline{z}_c^{1y}\right)\left(\overline{h}_c^{1y}\right)\right]\right\} \end{bmatrix} \tag{A.20c}$$

By also applying the slope conditions in Eqs. A.15a, i.e. $-\overline{z}_c^{1x} = \overline{h}_c^{1x}$ and $-\overline{z}_c^{1y} = \overline{h}_c^{1y}$, Eqs. A.20 are simplified to:

$$\mathbf{L}_c^0 = \begin{bmatrix} 0 \\ 0 \end{bmatrix} \tag{A.21a}$$

$$\mathbf{L}_c^{1x} = \begin{bmatrix} 0 \\ \frac{g}{\Delta y}\left(\overline{z}^{1y}\overline{z}_c^{1x}\right) \end{bmatrix} \tag{A.21b}$$

$$\mathbf{L}_c^{1y} = \begin{bmatrix} \frac{g}{\Delta x}\left(\overline{z}^{1x}\overline{z}_c^{1y}\right) \\ 0 \end{bmatrix} \tag{A.21c}$$

Clearly, Eqs. A.21 show that only operator $\mathbf{L}_c^0$ vanishes, meaning that the scheme is well-balanced only for the mean (discharge) coefficients. As for the discharge slope coefficients, the well-balanced condition is partially met given the remaining cross-dimensional slope dependency introduced in $\mathbf{L}_c^{1x}$ and $\mathbf{L}_c^{1y}$ by using the standard planar topography projection to discretise the local bed slope terms.

Therefore, to ensure that the simplified DG2 operators are completely well-balanced, an alternative topography projection expressed in Eq. A.22:

$$\partial_x[z_h(0,y)|_{x=0}] = 0 \quad \text{and} \quad \partial_x z_h|_{y=0} = \partial_x[z_h(x,0)|_{Q_c}] = \left(\frac{2}{\Delta x}\right) z_c^{1x} \tag{A.22a}$$

$$\partial_y[z_h(x,0)|_{y=0}] = 0 \quad \text{and} \quad \partial_y z_h|_{x=0} = \partial_y[z_h(0,y)|_{Q_c}] = \left(\frac{2}{\Delta y}\right) z_c^{1y} \tag{A.22b}$$

must be considered instead prior to evaluating Eqs. A.21b and A.21c, which then lead to the following slope-decoupled versions of them:

$$\mathbf{S}(h_h(G_{x2})) - \mathbf{S}(h_h(G_{x1})) = \begin{bmatrix} -g\left(\frac{2\bar{z}_c^{1x}}{\Delta x}\right)\left(\frac{\bar{h}_c^{1x}}{\sqrt{3}}\right) \\ 0 \end{bmatrix} \tag{A.23a}$$

$$\mathbf{S}(h_h(G_{y2})) - \mathbf{S}(h_h(G_{y1})) = \begin{bmatrix} -g\left(\frac{2\bar{z}_c^{1y}}{\Delta y}\right)\left(\frac{\bar{h}_c^{1y}}{\sqrt{3}}\right) \\ 0 \end{bmatrix} \tag{A.23b}$$

In turn, Eqs. A.23 (together with Eqs. A.17-A.21a) in Eqs. A.14 lead to the full zeroing of the DG2 slope operators $\mathbf{L}_c^{1x}$ and $\mathbf{L}_c^{1y}$ to ensure completely well-balanced DG2 planar solutions and a slope-decoupled 2D-DG2 solver.

Bibliography

Afifi, Z., Chu, H. J., Kuo, Y. L., Hsu, Y. C., Wong, H. K. & Ali, M. Z. (2019), 'Residential flood loss assessment and risk mapping from high-resolution simulation', *Water (Switzerland)* **11**(4), 1–15.

Alcrudo, F. (2004), 'A State of the Art Review on Mathematical Modelling of Flood Propagation', *IMPACT Project* pp. 1–22.

Alho, P. & Aaltonen, J. (2008), 'Comparing a 1D hydraulic model with a 2D hydraulic model for the simulation of extreme glacial outburst flood', *Hydrological Processes* **22**, 1537–1547.

URL: *http://jamsb.austms.org.au/courses/CSC2408/semester3/resources/ldp/abs-guide.pdf*

Alkema, D. (2007), Simulating floods - on the application of a 2D-hydraulic model for flood hazard and risk assessment, PhD thesis, University of Utrecht.

Alvarez-Vázquez, L. J., Martínez, A., Vázquez-Méndez, M. E. & Vilar, M. A. (2008), 'An optimal shape problem related to the realistic design of river fishways', *Ecological Engineering* **32**(4), 293–300.

An, H. & Yu, S. (2014), 'An accurate multidimensional limiter on quadtree grids for shallow water flow simulation', *Journal of Hydraulic Research* **52**(4), 565–574.

URL: *https://doi.org/10.1080/00221686.2013.878404*

Arrighi, C., Pregnolato, M., Dawson, R. J. & Castelli, F. (2019), 'Science of the Total Environment Preparedness against mobility disruption by floods', *Science of the Total Environment* **654**, 1010–1022.

Ata, R. (2012), 'TELEMAC-2D new finite volume schemes for shallow water equations with source terms on 2D unstructured grids', *XIXth TELEMAC-MASCARET User Conference* .

Aureli, F., Dazzi, S., Maranzoni, A., Mignosa, P. & Vacondio, R. (2015), 'Experimental and numerical evaluation of the force due to the impact of a dam-break wave on a structure', *Advances in Water Resources* **76**, 29–42.
URL: *http://dx.doi.org/10.1016/j.advwatres.2014.11.009*

Ayog, J. L. & Kesserwani, G. (2021), 'Reconstructed DEM of the Morgan-Selwyn floodway with added building piers'.
URL: *http://doi.org/10.5281/zenodo.4645480*

Bai, F. P., Yang, Z. H. & Zhou, W. G. (2018), 'Study of total variation diminishing (TVD) slope limiters in dam-break flow simulation', *Water Science and Engineering* **11**(1), 68–74.
URL: *https://doi.org/10.1016/j.wse.2017.09.004*

Banks, J. C., Camp, J. V. & Abkowitz, M. D. (2014), 'Adaptation planning for floods: A review of available tools', *Natural Hazards* **70**(2), 1327–1337.

Barthélémy, S., Ricci, S., Rochoux, M. C., Le Pape, E. & Thual, O. (2017), 'Ensemble-based data assimilation for operational flood forecasting – On the merits of state estimation for 1D hydrodynamic forecasting through the example of the "Adour Maritime" river', *Journal of Hydrology* **552**, 210–224.

Bates, P. D., Pappenberger, F. & Romanowicz, R. J. (2014), *Uncertainty in flood inundation modelling*, number December 2015.

Bates, P. D., Wilson, C. A. M. E., Hervouet, J.-M. & Stewart, M. D. (1999), 'Two dimensional flnite element modelling of floodplain flow', *Earth Surface Processes and Landforms* **17**, 575–588.

Bazin, P.-H. (2013), Flows during floods in urban areas: influence of the detailed topography and exchanges with the sewer system, PhD thesis, Université Claude Bernard - Lyon I.

Bazin, P.-H., Mignot, E. & Paquier, A. (2017), 'Computing flooding of crossroads with obstacles using a 2D numerical model', *Journal of Hydraulic Research* **55**(1), 72–84.

Beden, N. & Ulke Keskin, A. (2021), 'Flood map production and evaluation of flood risks in situations of insufficient flow data', *Natural Hazards* **105**(3), 2381–2408.
URL: *https://doi.org/10.1007/s11069-020-04404-y*

Begnudelli, L. & Sanders, B. F. (2006), 'Unstructured Grid Finite-Volume Algorithm for Shallow-Water Flow and Scalar Transport with Wetting and Drying', *Journal of Hydraulic Engineering* **132**(April), 371–384.

Begnudelli, L. & Sanders, B. F. (2007), 'Conservative wetting and drying methodology for quadrilateral grid finite-volume models', *Journal of Hydraulic Engineering* **133**(3), 312–322.

Beisiegel, N., Vater, S., Behrens, J. & Dias, F. (2020), 'An adaptive discontinuous Galerkin method for the simulation of hurricane storm surge', *Ocean Dynamics* **70**(5), 641–666.

Berger, M., Aftosmis, M. J. & Murman, S. M. (2005), Analysis of Slope Limiters on Irregular Grids, *in* '43rd AIAA Aerospace Sciences Meeting', Reno, Nevada, pp. 1–22.

Biswas, R. & Devine, K. D. (1994), 'Parallel, adaptive finite element methods for conservation laws', *Applied Numerical Mathematics* **9274**(93).

Bladé, E., Cea, L., Corestein, G., Escolano, E., Puertas, J., Vázquez-Cendón, E., Dolz, J. & Coll, A. (2014), Iber: herramienta de simulación numérica del flujo en ríos, Technical Report 1.

BMT-WBM (2016), TUFLOW User Manual Build 2016-03-AE, Technical report, BMT WBM.

BMT-WBM (2018), TUFLOW Classic/HPC User Manual Build 2018-03-AD, Technical report, BMT WBM.

Bokhove, O. (2005), ‘Flooding and drying in discontinuous Galerkin finite-element discretizations of shallow-water equations. Part 1: One dimension’, *Journal of Scientific Computing* **22-23**(June), 47–82.

Bradford, S. F. & Sanders, B. F. (2002), ‘Finite-volume model for shallow-water flooding of arbitrary topography’, *Journal of Hydraulic Engineering* **128**(3), 289–298.

Brunner, G. (2016), Benchmarking of the HEC-RAS Two-Dimensional Hydraulic Modeling Capabilities, Technical Report April.

Brus, S. R., Wirasaet, D., Westerink, J. J. & Dawson, C. (2017), ‘Performance and Scalability Improvements for Discontinuous Galerkin Solutions to Conservation Laws on Unstructured Grids’, *Journal of Scientific Computing* **70**(1), 210–242.

Bunya, S., Kubatko, E. J., Westerink, J. J. & Dawson, C. (2009), ‘A wetting and drying treatment for the Runge–Kutta discontinuous Galerkin solution to the shallow water equations’, *Computer Methods in Applied Mechanics and Engineering* **198**, 1548–1562.

Caleffi, V., Valiani, A. & Bernini, A. (2006), ‘Fourth-order balanced source term treatment in central WENO schemes for shallow water equations’, *Journal of Computational Physics* **218**(1), 228–245.

Caleffi, V., Valiani, A. & Li, G. (2016), ‘A comparison between bottom-discontinuity numerical treatments in the DG framework’, *Applied Mathematical Modelling* **40**(17-18), 7516–7531.

Caviedes-Voullième, D. & Kesserwani, G. (2015), ‘Benchmarking a multiresolution discontinuous Galerkin shallow water model: Implications for computational hydraulics', *Advances in Water Resources* **86**, 14–31.

Cea, L., Puertas, J. & Vázquez-Cendón, M. E. (2007), 'Depth averaged modelling of turbulent shallow water flow with wet-dry fronts', *Archives of Computational Methods in Engineering* **14**(3), 303–341.

Chan, J., Wang, Z., Modave, A., Remacle, J.-F. & Warburton, T. (2016), 'GPU-accelerated discontinuous Galerkin methods on hybrid meshes', *Journal of Computational Physics* **318**, 142–168.
URL: *https://www.sciencedirect.com/science/article/pii/S0021999116300353*

Chartres, B. & Stepleman, R. (1972), 'A general theory of convergence for numerical methods'.

Cheng, C., Qian, X. & Zhang, Y. (2011), 'Estimation of the evacuation clearance time based on dam-break simulation of the Huaxi dam in Southwestern China', *Natural Hazards* **57**, 227–243.

Clare, M., Percival, J., Angeloudis, A., Cotter, C. & Piggott, M. (2020), 'Hydro-morphodynamics 2D modelling using a discontinuous Galerkin discretisation'.

Cobby, D. M., Mason, D. C. & Davenport, I. J. (2001), 'Image processing of airborne scanning laser altimetry data for improved river flood modelling', *ISPRS Journal of Photogrammetry and Remote Sensing* **56**(2), 121–138.

Cockburn, B. & Shu, C.-w. (2001), 'Runge-Kutta Discontinuous Galerkin Methods for Convection Dominated Problems', *Journal of Scientific Computing* **16**(3), 173–261.

Cohen, R., Hilton, J. & Prakash, M. (2016), Benchmark testing the Swift flood modelling solver : Version I. CSIRO Australia., Technical report.

Collecutt, G. & Syme, B. (2017), Experimental benchmarking of mesh size and time-step convergence for a 1st and 2nd order SWE finite volume scheme, *in* 'Proceedings of the 37th IAHR World Congress'.

Conroy, C. J. & Kubatko, E. J. (2016), 'hp discontinuous Galerkin methods for the vertical extent of the water column in coastal settings part I: Barotropic forcing', *Journal of Computational Physics* **305**, 1147–1171.
URL: *https://www.sciencedirect.com/science/article/pii/S0021999115007159*

Costabile, P., Costanzo, C., Lorenzo, G. D. & Macchione, F. (2020), 'Is local flood hazard assessment in urban areas significantly influenced by the physical complexity of the hydrodynamic inundation model ?', *Journal of Hydrology* **580**(September 2019), 124231.
URL: *https://doi.org/10.1016/j.jhydrol.2019.124231*

Cozzolino, L., Varra, G., Cimorelli, L., Pianese, D. & Della Morte, R. (2021), 'Friction decoupling and loss of rotational invariance in 2D flooding models', *Advances in Water Resources* **152**(October 2020), 103919.
URL: *https://doi.org/10.1016/j.advwatres.2021.103919*

CRED (2015), The Human Cost of Weather-Related Disasters, 1995-2015, Technical report.

Crossley, A., Lamb, R. & Waller, S. (2010), Fast solution of the shallow water equations using GPU technology, *in* 'BHS Third International Symposium: Managing Consequences of a Changing Global Environment', Newcastle, United Kingdom.

Dawson, C., Trahan, C. J., Kubatko, E. J. & Westerink, J. J. (2013), 'A parallel local timestepping Runge–Kutta discontinuous Galerkin method with applications to coastal ocean modeling', *Computer Methods in Applied Mechanics and Engineering* **259**, 154–165.
URL: *https://www.sciencedirect.com/science/article/pii/S0045782513000662*

de Almeida, G. A., Bates, P. & Ozdemir, H. (2018), 'Modelling urban floods at submetre resolution: challenges or opportunities for flood risk management?', *Journal of Flood Risk Management* **11**, S855–S865.

Delis, A. I. & Nikolos, I. K. (2013), ‘A novel multidimensional solution reconstruction and edge-based limiting procedure for unstructured cell-centered finite volumes with application to shallow water dynamics’, *International Journal for Numerical Methods in Fluids* **71**, 584–633.

Delis, A. I., Nikolos, I. K. & Kazolea, M. (2011), ‘Performance and Comparison of Cell-Centered and Node-Centered Unstructured Finite Volume Discretizations for Shallow Water Free Surface Flows’, *Arch Comput Methods Eng.* **18**, 57–118.

Dottori, F., Di Baldassarre, G. & Todini, E. (2013), ‘Detailed data is welcome, but with a pinch of salt: Accuracy, precision, and uncertainty in flood inundation modeling’, *Water Resources Research* **49**(9), 6079–6085.

Drago, M., Cescon, B. & Iovenitti, L. (2001), ‘A three-dimensional numerical model for eutrophication and pollutant transport’, *Ecological Modelling* .

Duan, J. G. (2005), Two-dimensional model simulation of flow field around bridge piers, *in* ‘World Water Congress 2005: Impacts of Global Climate Change - Proceedings of the 2005 World Water and Environmental Resources Congress’, Anchorage, Alaska.

DuChene, M., Spagnuolo, A. M., Kubatko, E., Westerink, J. & Dawson, C. (2011), ‘A Framework for Running the ADCIRC Discontinuous Galerkin Storm Surge Model on a GPU’, *Procedia Computer Science* **4**, 2017–2026.
URL: *https://www.sciencedirect.com/science/article/pii/S187705091100278X*

Duran, A. & Marche, F. (2014), ‘Recent advances on the discontinuous Galerkin method for shallow water equations with topography source terms’, *Computers and Fluids* **101**, 88–104.
URL: *http://dx.doi.org/10.1016/j.compfluid.2014.05.031*

Echeverribar, I., Morales-Hernández, M., Brufau, P. & García-Navarro, P. (2019), ‘2D numerical simulation of unsteady flows for large scale floods prediction in real time’, *Advances in Water Resources* **134**, 103444.

Engineers Australia (2012), Australian Rainfall & Runoff Revision Project 15: Two Dimensional Modelling in Urban and Rural floodplains, Stage 1 and 2 Draft Report, Engineers Australia, Technical Report November, Engineers Australia.

Ern, A., Piperno, S. & Djadel, K. (2008), 'A well-balanced Runge-Kutta discontinuous Galerkin method for the shallow-water equations with flooding and drying', *International Journal for Numerical Methods in Fluids* (58), 1–25.

Eskilsson, C., El-Khamra, Y., Rideout, D., Allen, G., Chen, Q. J. & Tyagi, M. (2009), A Parallel High-Order Discontinuous Galerkin Shallow Water Model, *in* G. Allen, J. Nabrzyski, E. Seidel, G. D. van Albada, J. Dongarra & P. M. A. Sloot, eds, 'Computational Science – ICCS 2009', Springer Berlin Heidelberg, Berlin, Heidelberg, pp. 63–72.

Eskilsson, C. & Sherwin, S. J. (2004), 'A triangular spectral/hp discontinuous galerkin method for modelling 2d shallow water equations', *International Journal for Numerical Methods in Fluids* **45**, 605–623.

Fu, G. & Shu, C.-W. (2017), 'A new troubled-cell indicator for discontinuous Galerkin methods for hyperbolic conservation laws', *Journal of Computational Physics* **347**, 305–327.
URL: *http://www.sciencedirect.com/science/article/pii/S0021999117305004*

Fuhry, M., Giuliani, A. & Krivodonova, L. (2014), 'Discontinuous Galerkin methods on graphics processing units for nonlinear hyperbolic conservation laws', *International Journal for Numerical Methods in Fluids* **76**(12), 982–1003.
URL: *https://onlinelibrary.wiley.com/doi/abs/10.1002/fld.3963*

García-Navarro, P., Murillo, J., Fernández-Pato, J., Echeverribar, I. & Morales-Hernández, M. (2019), 'The shallow water equations and their application to realistic cases', *Environmental Fluid Mechanics* **19**(5), 1235–1252.
URL: *https://doi.org/10.1007/s10652-018-09657-7*

Gerhard, N., Caviedes-Voullième, D., Müller, S. & Kesserwani, G. (2015), 'Multiwavelet-based grid adaptation with discontinuous Galerkin schemes for shallow water equations',

Journal of Computational Physics **301**, 265–288.
URL: *http://dx.doi.org/10.1016/j.jcp.2015.08.030*

Ghostine, R., Kapfer, C., Kannan, V. & Hoteit, I. (2019), 'Flood Modeling in Urban Area Using a Well-Balanced Discontinuous Galerkin Scheme on Unstructured Triangular Grids', *International Journal of Mathematical and Computational Sciences* **13**(2), 19–29.

Ghostine, R., Kesserwani, G., Vazquez, J., Rivière, N., Ghenaim, A. & Mose, R. (2009), 'Simulation of supercritical flow in crossroads: Confrontation of a 2D and 3D numerical approaches to experimental results', *Computers and Fluids* **38**(2), 425–432.
URL: *http://dx.doi.org/10.1016/j.compfluid.2008.05.003*

Godunov, S. K. (1959), 'A difference method for numerical calculation of discontinuous solutions of the equations of hydrodynamics', *Mat. Sb. (N.S.)* **47 (89)**(3), 271–306.

Gourgue, O., Comblen, R., Lambrechts, J., Kärnä, T., Legat, V. & Deleersnijder, E. (2009), 'Advances in Water Resources A flux-limiting wetting – drying method for finite-element shallow-water models , with application to the Scheldt Estuary', *Advances in Water Resources* **32**(12), 1726–1739.
URL: *http://dx.doi.org/10.1016/j.advwatres.2009.09.005*

Guo, K., Guan, M. & Yu, D. (2021), 'Urban surface water flood modelling-a comprehensive review of current models and future challenges', *Hydrology and Earth System Sciences* **25**(5), 2843–2860.

Henckens, G. & Engel, W. (2017), Benchmark inundatiemodellen: modelfunctionaliteiten en testbank berekeningen, Technical report, Stichting Toegepast Onderzoek Waterbeheer (STOWA), Amersfoort, The Netherlands.

Hinkelmann, R., Liang, Q., Aizinger, V. & Dawson, C. (2015), 'Robust shallow water models', *Environmental Earth Sciences* **74**(11), 7273–7274.

Horritt, M. S. & Bates, P. D. (2001), 'Predicting floodplain inundation: Raster-based modelling versus the finite-element approach', *Hydrological Processes* **15**(5), 825–842.

Horritt, M. S. & Bates, P. D. (2002), 'Evaluation of 1D and 2D numerical models for predicting river flood inundation', **268**, 87–99.

Horritt, M. S., Bates, P. D. & Mattinson, M. J. (2006), 'Effects of mesh resolution and topographic representation in 2D finite volume models of shallow water fluvial flow', *Journal of Hydrology* **329**(1-2), 306–314.

Horváth, Z., Buttinger-Kreuzhuber, A., Konev, A., Cornel, D., Komma, J., Blöschl, G., Noelle, S. & Waser, J. (2020), 'Comparison of Fast Shallow-Water Schemes on Real-World Floods', *Journal of Hydraulic Engineering* **146**(1), 1–16.

Hou, J., Liang, Q., Zhang, H. & Hinkelmann, R. (2014), 'Multislope MUSCL method applied to solve shallow water equations', *Computers and Mathematics with Applications* **68**(12), 2012–2027.
URL: *http://dx.doi.org/10.1016/j.camwa.2014.09.018*

Hou, J., Liang, Q., Zhang, H. & Hinkelmann, R. (2015), 'An efficient unstructured MUSCL scheme for solving the 2D shallow water equations', *Environmental Modelling and Software* **66**, 131–152.
URL: *http://dx.doi.org/10.1016/j.envsoft.2014.12.007*

Hunter, N. M., Bates, P. D., Horritt, M. S. & Wilson, M. D. (2007), 'Simple spatially-distributed models for predicting flood inundation: A review', *Geomorphology* **90**(3-4), 208–225.

Hunter, N. M., Bates, P. D., Neelz, S., Pender, G., Villanueva, I., Wright, N. G., Liang, D., Falconer, R. A., Lin, B., Waller, S., Crossley, A. J. & Mason, D. C. (2008), 'Benchmarking 2D hydraulic models for urban flooding', *Proceedings of the Institution of Civil Engineers - Water Management* **161**, 13–30.

Huxley, C., Syme, B. & Symons, E. (2017), UK Environment Agency 2D Hydraulic Model Benchmark Tests. 2017-09 TUFLOW Release Update, Technical report, BMT WBM Pty Ltd, Brisbane, Australia.

Hydronia LLC (2019), HydroBID Flood Two-Dimensional Flood and River Dynamics Model, Technical report.

Innovyze (2011), Infoworks 11.5 RS Help, Technical report, Broomfield, Colorado.

Inthasaro, P. & Wu, W. (2012), A 1-D aquatic ecosystem/ecotoxicology model in open channels, *in* 'Proceedings - 2012 International Conference on Biomedical Engineering and Biotechnology, iCBEB 2012', pp. 1144–1147.

James, R., Finney, K., Perera, N., James, B. & Peyron, N. (2013), SWMM5/PCSWMM integrated 1D-2D modeling, *in* 'Fifty Years of Watershed Modeling - Past, Present And Future'.
URL: *http://dc.engconfintl.org/watershed/12*

Jamieson, S. R., Lhomme, J., Wright, G. & Gouldby, B. (2012), 'A highly efficient 2D flood model with sub-element topography', *Proceedings of the Institution of Civil Engineers: Water Management* **165**, 581–595.

Jenkins, C. & Garcia, R. (2015), Benchmarking of 2D hydraulic modelling packages results, Technical report, Hydronia.
URL: *http://www.hydronia.com/tests-docs*

Jonkman, S. N., Bočkarjova, M., Kok, M. & Bernardini, P. (2008), 'Integrated hydrodynamic and economic modelling of flood damage in the Netherlands', *Ecological Economics* .

Karim, F., Dutta, D., Marvanek, S., Petheram, C., Ticehurst, C., Lerat, J., Kim, S. & Yang, A. (2015), 'Assessing the impacts of climate change and dams on floodplain inundation and wetland connectivity in the wet-dry tropics of northern Australia', *Journal of Hydrology* .

Kärnä, T., Kramer, S. C., Mitchell, L., Ham, D. A., Piggott, M. D. & Baptista, A. M. (2018), 'Thetis coastal ocean model: discontinuous Galerkin discretization for the three-dimensional hydrostatic equations', *Geoscientific Model Development Discussions* pp. 1–36.

Kesserwani, G. (2013), 'Topography discretization techniques for Godunov-type shallow water numerical models: a comparative study', *Journal of Hydraulic Research* **51**(4), 351–367.
URL: *http://www.tandfonline.com/doi/abs/10.1080/00221686.2013.796574*

Kesserwani, G., Ghostine, R., Vazquez, J., Ghenaim, A. & Mosé, R. (2008), 'Riemann Solvers with Runge–Kutta Discontinuous Galerkin Schemes for the 1D Shallow Water Equations', *Journal of Hydraulic Engineering* **134**(2), 243–255.

Kesserwani, G. & Liang, Q. (2010), 'Well-balanced RKDG2 solutions to the shallow water equations over irregular domains with wetting and drying', *Computers and Fluids* **39**(10), 2040–2050.
URL: *http://dx.doi.org/10.1016/j.compfluid.2010.07.008*

Kesserwani, G. & Liang, Q. (2011), 'A conservative high-order discontinuous Galerkin method for the shallowwater equations with arbitrary topography', *International Journal for Numerical Methods in Engineering* **86**, 47–69.

Kesserwani, G. & Liang, Q. (2012*a*), 'Dynamically adaptive grid based discontinuous Galerkin shallow water model', *Advances in Water Resources* **37**, 23–39.
URL: *http://dx.doi.org/10.1016/j.advwatres.2011.11.006*

Kesserwani, G. & Liang, Q. (2012*b*), 'Influence of Total-Variation-Diminishing Slope Limiting on Local Discontinuous Galerkin Solutions of the Shallow Water Equations', *Journal of Hydraulic Engineering* **138**(2), 216–222.
URL: *http://dx.doi.org/10.1061/(ASCE)HY.1943-7900.0000494*

Kesserwani, G. & Liang, Q. (2012*c*), 'Locally limited and fully conserved RKDG2 shallow water solutions with wetting and drying', *Journal of Scientific Computing* **50**(1), 120–144.

Kesserwani, G. & Liang, Q. (2015), 'RKDG2 shallow-water solver on non-uniform grids with local time steps: Application to 1D and 2D hydrodynamics', *Applied Mathematical Modelling* **39**(3-4), 1317–1340.
URL: *http://dx.doi.org/10.1016/j.apm.2014.08.009*

Kesserwani, G. & Sharifian, M. K. (2020), '(Multi)wavelets increase both accuracy and efficiency of standard Godunov-type hydrodynamic models: Robust 2D approaches', *Advances in Water Resources* **144**(July), 103693.

URL: *https://doi.org/10.1016/j.advwatres.2020.103693*

Kesserwani, G. & Wang, Y. (2014), 'Discontinuous galerkin flood model formulation: Luxury or necessity?', *Water Resources Research* **50**, 6522–6541.

Klöckner, A., Warburton, T., Bridge, J. & Hesthaven, J. S. (2009), 'Nodal discontinuous Galerkin methods on graphics processors', *Journal of Computational Physics* **228**(21), 7863–7882.

URL: *https://www.sciencedirect.com/science/article/pii/S0021999109003647*

Krivodonova, L., Xin, J., Remacle, J. F., Chevaugeon, N. & Flaherty, J. E. (2004), 'Shock detection and limiting with discontinuous Galerkin methods for hyperbolic conservation laws', *Applied Numerical Mathematics* **48**(3-4), 323–338.

Kubatko, E. J., Westerink, J. J. & Dawson, C. (2006), 'hp Discontinuous Galerkin methods for advection dominated problems in shallow water flow', *Computer Methods in Applied Mechanics and Engineering* **196**(1-3), 437–451.

Kvočka, D., Ahmadian, R. & Falconer, R. A. (2017), 'Flood inundation modelling of flash floods in steep river basins and catchments', *Water (Switzerland)* **9**(9).

Kvočka, D., Falconer, R. A. & Bray, M. (2015), 'Appropriate model use for predicting elevations and inundation extent for extreme flood events', *Natural Hazards* **79**(3), 1791–1808.

Kvočka, D., Falconer, R. A. & Bray, M. (2016), 'Flood hazard assessment for extreme flood events', *Natural Hazards* **84**(3), 1569–1599.

Lambrechts, J., Humphrey, C., McKinna, L., Gourge, O., Fabricius, K. E., Mehta, A. J., Lewis, S. & Wolanski, E. (2010), 'Importance of wave-induced bed liquefaction in the fine sediment budget of Cleveland Bay, Great Barrier Reef', *Estuarine, Coastal and Shelf*

Science **89**(2), 154–162.

URL: *http://dx.doi.org/10.1016/j.ecss.2010.06.009*

Latrubesse, E. M., Park, E., Sieh, K., Dang, T., Lin, Y. N. & Yun, S.-h. (2020), 'Geomorphology Dam failure and a catastrophic fl ood in the Mekong basin (Bolaven', *Geomorphology* **362**, 107221.

URL: *https://doi.org/10.1016/j.geomorph.2020.107221*

Le Bars, Y., Vallaeys, V., Deleersnijder, É., Hanert, E., Carrere, L. & Channelière, C. (2016), 'Unstructured-mesh modeling of the Congo river-to-sea continuum', *Ocean Dynamics* **66**(4), 589–603.

Le, H. A., Lambrechts, J., Ortleb, S., Gratiot, N., Deleersnijder, E. & Soares-Frazão, S. (2020), 'An implicit wetting–drying algorithm for the discontinuous Galerkin method: application to the Tonle Sap, Mekong River Basin', *Environmental Fluid Mechanics* (0123456789).

URL: *https://doi.org/10.1007/s10652-019-09732-7*

Leopardi, A., Oliveri, E. & Greco, M. (2002), 'Two-Dimensional Modeling of Floods to Map Risk-Prone Areas', *Journal of Water Resources Planning and Management* **128**(3), 168–178.

Leskens, J. G., Brugnach, M., Hoekstra, A. Y. & Schuurmans, W. (2014), 'Why are decisions in flood disaster management so poorly supported by information from flood models?', *Environmental Modelling and Software* **53**, 53–61.

Lhomme, J., Gutierrez-Andres, J., Weisgerber, A., Davison, M., Mulet-Marti, J., Cooper, A. & Gouldby, B. (2010), 'Testing a new two-dimensional flood modelling system: analytical tests and application to a flood event', *Journal of Flood Risk Management* **3**, 33–51.

Liang, D., Lin, B. & Falconer, R. A. (2007), 'A boundary-fitted numerical model for flood routing with shock-capturing capability', *Journal of Hydrology* **332**(3-4), 477–486.

Liang, Q. & Marche, F. (2009), 'Numerical resolution of well-balanced shallow water equations with complex source terms', *Advances in Water Resources* **32**(6), 873–884.
URL: *http://dx.doi.org/10.1016/j.advwatres.2009.02.010*

Löwe, R., Urich, C., Sto. Domingo, N., Mark, O., Deletic, A. & Arnbjerg-Nielsen, K. (2017), 'Assessment of urban pluvial flood risk and efficiency of adaptation options through simulations – A new generation of urban planning tools', *Journal of Hydrology* **550**, 355–367.
URL: *http://dx.doi.org/10.1016/j.jhydrol.2017.05.009*

Lu, X. & Xie, S. (2016), 'Conventional versus pre-balanced forms of the shallow-water equations solved using finite-volume method', *Ocean Modelling* **101**, 113–120.
URL: *http://dx.doi.org/10.1016/j.ocemod.2016.04.002*

Marras, S., Kopera, M. A., Constantinescu, E. M., Suckale, J. & Giraldo, F. X. (2016), 'A continuous/discontinuous Galerkin solution of the shallow water equations with dynamic viscosity, high-order wetting and drying, and implicit time integration', pp. 1476–1493.
URL: *http://arxiv.org/abs/1607.04547*

Marras, S., Kopera, M. A., Constantinescu, E. M., Suckale, J. & Giraldo, F. X. (2018), 'A residual-based shock capturing scheme for the continuous/discontinuous spectral element solution of the 2D shallow water equations', *Advances in Water Resources* **114**, 45–63.
URL: *http://linkinghub.elsevier.com/retrieve/pii/S0309170816302299*

McRae, A. T. T. (2015), Compatible finite element methods for atmospheric dynamical cores (PhD thesis), PhD thesis, Imperial College London.
URL: *http://hdl.handle.net/10044/1/31529*

Mignot, E., Zeng, C., Dominguez, G., Li, C. W., Rivière, N. & Bazin, P. H. (2013), 'Impact of topographic obstacles on the discharge distribution in open-channel bifurcations', *Journal of Hydrology* **494**, 10–19.
URL: *http://dx.doi.org/10.1016/j.jhydrol.2013.04.023*

Mintgen, F. & Manhart, M. (2018), 'A bi-directional coupling of 2D shallow water and 3D Reynolds-averaged Navier–Stokes models', *Journal of Hydraulic Research* **56**(6), 771–785.
URL: *https://doi.org/10.1080/00221686.2017.1419989*

Morales-Hernández, M., Sharif, M. B., Kalyanapu, A., Ghafoor, S. K., Dullo, T. T., Gangrade, S., Kao, S. C., Norman, M. R. & Evans, K. J. (2021), 'TRITON: A Multi-GPU open source 2D hydrodynamic flood model', *Environmental Modelling and Software* **141**(March).

Morita, M. (2011), 'Quantification of increased flood risk due to global climate change for urban river management planning', *Water Science and Technology* .

Mouri, G., Minoshima, D., Golosov, V., Chalov, S., Seto, S., Yoshimura, K., Nakamura, S. & Oki, T. (2013), 'Probability assessment of flood and sediment disasters in Japan using the total runoff-integrating pathways model', *International Journal of Disaster Risk Reduction* .

Mudashiru, R. B., Sabtu, N., Abustan, I. & Waheed, B. (2021), 'Flood Hazard Mapping Methods: A Review', *Journal of Hydrology* **603**, 126846.
URL: *https://doi.org/10.1016/j.jhydrol.2021.126846*

Mulamba, T., Bacopoulos, P., Kubatko, E. J. & Pinto, G. F. (2019), 'Sea-level rise impacts on longitudinal salinity for a low-gradient estuarine system', *Climatic Change* **152**(3-4), 533–550.

Mungkasi, S. & Roberts, S. G. (2013), 'Validation of ANUGA hydraulic model using exact solutions to shallow water wave problems', *Journal of Physics: Conference Series* **423**(1).

Musolino, G., Ahmadian, R., Xia, J. & Falconer, R. A. (2020), 'Mapping the danger to life in flash flood events adopting a mechanics based methodology and planning evacuation routes', *Journal of Flood Risk Management* **13**(4), 1–19.

Neal, J., Dunne, T., Sampson, C., Smith, A. & Bates, P. (2018), 'Optimisation of the two-dimensional hydraulic model lisfood-fp for cpu architecture', *Environmental Modelling and Software* **107**, 148–157.

Neal, J., Villanueva, I., Wright, N., Willis, T., Fewtrell, T. & Bates, P. (2012), 'How much physical complexity is needed to model flood inundation?', *Hydrological Processes* **26**(15), 2264–2282.

Neelz, S. & Pender, G. (2009), *Desktop Review of 2D Hydraulic Modelling Packages. DEFRA/Environment Agency, UK.*, DEFRA/Environment Agency, UK.

Neelz, S. & Pender, G. (2010), Benchmarking of 2D Dyfraulic Modelling Packages. DEFRA/Environment Agency, UK., Technical report.

Neelz, S. & Pender, G. (2013), Benchmarking the Latest Generation of 2D Hydraulic Modelling Packages. DEFRA/Environment Agency, UK., Technical report, Environment Agency.

Nikolos, I. K. & Delis, A. I. (2009), 'An unstructured node-centered finite volume scheme for shallow water flows with wet/dry fronts over complex topography', *Computer Methods in Applied Mechanics and Engineering* **198**(47-48), 3723–3750.
URL: *http://dx.doi.org/10.1016/j.cma.2009.08.006*

Nkwunonwo, U. C., Whitworth, M. & Baily, B. (2020), 'A review of the current status of flood modelling for urban flood risk management in the developing countries', *Scientific African* **7**, e00269.
URL: *https://doi.org/10.1016/j.sciaf.2020.e00269*

Özgen-Xian, I., Xia, X., Liang, Q., Hinkelmann, R., Liang, D. & Hou, J. (2021), 'Innovations towards the next generation of shallow flow models', *Advances in Water Resources* **149**, 103867.
URL: *https://doi.org/10.1016/j.advwatres.2021.103867*

Patel, D. P., Ramirez, J. A., Srivastava, P. K., Bray, M. & Han, D. (2017), 'Assessment of flood inundation mapping of Surat city by coupled 1D / 2D hydrodynamic modeling : a case', *Natural Hazards* **89**(1), 93–130.

Pavlíček, M. & Bruland, O. (2019), ‘Numerical modelling of flash flood event in steep river using Telemac 2D and Sisyphe’, *XXVIth Telemac & Mascaret Users Conference* pp. 1–7.

Pender, G. (2006), ‘Briefing: Introducing the Flood Risk Management Research Consortium’, *Proceedings of the Institution of Civil Engineers - Water Management* **159**(1), 3–8.
URL: *http://www.icevirtuallibrary.com/doi/10.1680/wama.2006.159.1.3*

Pham Van, C., de Brye, B., Deleersnijder, E., Hoitink, A. J., Sassi, M., Spinewine, B., Hidayat, H. & Soares-Frazão, S. (2016), ‘Simulations of the flow in the Mahakam river–lake–delta system, Indonesia’, *Environmental Fluid Mechanics* **16**(3), 603–633.

Pina, R. D., Braunschweig, F., Silva, A., Ochoa-rodriguez, S., Simões, N. E., Mijic, A., Sa Marques, A. & Maksimovic, C. (2015), Urban stormwater modelling with MOHID, *in* ‘10th International Urban Drainage Modelling Conference’.

Pistrika, A. K. & Jonkman, S. N. (2010), ‘Damage to residential buildings due to flooding of New Orleans after hurricane Katrina’, *Natural Hazards* **54**, 413–434.

Qiu, J. & Shu, C.-w. (2005), ‘A Comparison of Troubled-Cell Indicators for Runge-Kutta Discontinuous Galerkin Methods Using Weighted Essentially Nonoscillatory Limiters’, *SIAM Journal of Scientific Computing* **27**(3), 995–1013.

Roe, P. (1997), ‘Approximate riemann solvers, parameter vectors, and difference schemes’, *Journal of Computational Physics* **135**(2), 250–258.
URL: *https://www.sciencedirect.com/science/article/pii/S0021999197957053*

Rubinato, M. (2015), Physical scale modelling of urban flood systems, PhD thesis, The University of Sheffield.

Rubinato, M., Shucksmith, J., Martins, R. & Kesserwani, G. (2021), ‘Particle Image Velocimetry (PIV) dataset for the parking lot configuration with a closed manhole’.
URL: *http://doi.org/10.5281/zenodo.4596731*

Salmon, S. U., Hipsey, M. R., Wake, G. W., Ivey, G. N. & Oldham, C. E. (2017), 'Quantifying Lake Water Quality Evolution: Coupled Geochemistry, Hydrodynamics, and Aquatic Ecology in an Acidic Pit Lake', *Environmental Science and Technology* .

Samii, A., Michoski, C. & Dawson, C. (2016), 'A parallel and adaptive hybridized discontinuous Galerkin method for anisotropic nonhomogeneous diffusion', *Computer Methods in Applied Mechanics and Engineering* **304**, 118–139.
URL: *https://www.sciencedirect.com/science/article/pii/S0045782516300317*

Sanders, B. F. & Bradford, S. F. (2006), 'Impact of limiters on accuracy of high-resolution flow and transport models', *Journal of Engineering Mechanics* **132**(1), 87–98.

Schubert, J. E. & Sanders, B. F. (2012), 'Building treatments for urban flood inundation models and implications for predictive skill and modeling efficiency', *Advances in Water Resources* **41**, 49–64.
URL: *http://dx.doi.org/10.1016/j.advwatres.2012.02.012*

Schubert, J. E., Sanders, B. F., Smith, M. J. & Wright, N. G. (2008), 'Unstructured mesh generation and landcover-based resistance for hydrodynamic modeling of urban flooding', *Advances in Water Resources* **31**(12), 1603–1621.
URL: *http://dx.doi.org/10.1016/j.advwatres.2008.07.012*

Schuurmans, W. & Leeuwen, E. V. (2014), 3Di : A new Dutch hydrological model, Technical Report Figure 1.

Scottish Environment Protection Agency (2016), Flood Modelling Guidance for Responsible Authorities, Technical report.

Shaw, J., Kesserwani, G., Neal, J., Bates, P. & Sharifian, M. K. (2021), 'Lisflood-fp 8.0: the new discontinuous galerkin shallow-water solver for multi-core cpus and gpus', *Geoscientific Model Development* **14**(6), 3577–3602.
URL: *https://gmd.copernicus.org/articles/14/3577/2021/*

Shirvani, M., Kesserwani, G. & Richmond, P. (2020), 'Agent-based modelling of pedestrian responses during flood emergency: mobility behavioural rules and implications for flood risk analysis', *Journal of Hydroinformatics* **22**(5), 1078–1092.

Shirvani, M., Kesserwani, G. & Richmond, P. (2021), 'Agent-based simulator of dynamic flood-people interactions', *Journal of Flood Risk Management* **n/a**(n/a), e12695.
URL: *https://onlinelibrary.wiley.com/doi/abs/10.1111/jfr3.12695*

Shrestha, A., Bhattacharjee, L., Baral, S., Thakur, B., Joshi, N., Kalra, A. & Gupta, R. (2020), *Understanding Suitability of MIKE 21 and HEC-RAS for 2D Floodplain Modeling*, pp. 237–253.
URL: *https://ascelibrary.org/doi/abs/10.1061/9780784482971.024*

Siviglia, A., Stocchino, A. & Colombini, M. (2009), 'Case Study: Design of Flood Control Systems on the Vara River by Numerical and Physical Modeling', *Journal of Hydraulic Engineering* **135**(12), 1063–1072.

Smith, G. P., Rahman, P. F. & Wasko, C. (2016), 'A comprehensive urban floodplain dataset for model benchmarking', *International Journal of River Basin Management* **14**(3), 345–356.

Smith, G. P., Wasko, C. D. & Miller, B. M. (2012), Modelling the influence of buildings on flood flow, *in* 'Floodplain Management National Conference', Canberra, ACT, Australia.

Soares-Frazão, S. & Zech, Y. (2007), 'Experimental study of dam-break flow against an isolated obstacle', *Journal of Hydraulic Research* **45**, 27–36.
URL: *https://www.tandfonline.com/doi/full/10.1080/00221686.2007.9521830*

Soares-Frazão, S. & Zech, Y. (2008), 'Dam-break flow through an idealised city', *Journal of Hydraulic Research* **46**(5), 648–658.

Sommer, T., Karpf, C., Ettrich, N., Haase, D., Weichel, T., Peetz, J. V., Steckel, B., Eulitz, K. & Ullrich, K. (2009), 'Coupled modelling of subsurface water flux for an integrated flood risk management', *Natural Hazards and Earth System Science* .

Sweby, P. K. (1984), 'High Resolution Schemes Using Flux Limiters for Hyperbolic Conservation Laws', *SIAM Journal on Numerical Analysis* **21**(5), 995–1011.

Syme, W. J. (2008), Flooding in Urban Areas - 2D Modelling Approaches for Buildings and Fences, *in* '9th National Conference on Hydraulics in Water Engineering: Hydraulics', Engineers Australia, Barton, A.C.T.

Teng, J., Jakeman, A. J., Vaze, J., Croke, B. F., Dutta, D. & Kim, S. (2017), 'Flood inundation modelling: A review of methods, recent advances and uncertainty analysis', *Environmental Modelling and Software* **90**, 201–216.
URL: *http://dx.doi.org/10.1016/j.envsoft.2017.01.006*

Thacker, W. (1981), 'Some exact solutions to the nonlinear shallow-water wave equations', *Journal of Fluid Mechanics* **107**, 499–508.

Toombes, L. & Chanson, H. (2011), Numerical Limitations of Hydraulic Models, *in* 'IAHR World Congress - Balance and Uncertainty', Engineers Australia, Brisbane, Australia, pp. 2322–2329.

Toro, E. F. (1999), *Riemann Solvers and Numerical Methods for Fluid Dynamics: A Practical Introduction*, Applied mechanics: Researchers and students, Springer.

Toro, E. F. (2001), *Shock-Capturing Methods for Free-Surface Shallow Flows*, John Wiley & Sons, West Sussex.

Toro, E. F. & Garcia-Navarro, P. (2007), 'Godunov-type methods for free-surface shallow flows: A review', *Journal of Hydraulic Research* **45**(6), 736–751.
URL: *http://www.tandfonline.com/doi/abs/10.1080/00221686.2007.9521812*

TYGRON (2019), Water module theory: Tygron Geodesign Platform, Technical report.
URL: *https://support.tygron.com/wiki/Water_Module_Theory*

Van Leer, B. (1979), 'Towards the ultimate conservative difference scheme', *Journal of Computational Physics* **32**, 101–136.

Vater, S., Beisiegel, N. & Behrens, J. (2019), 'A limiter-based well-balanced discontinuous Galerkin method for shallow-water flows with wetting and drying: Triangular grids', *International Journal for Numerical Methods in Fluids* **91**(8), 395–418.

Vetsch, D., Siviglia, A., Caponi, F., Ehrbar, D., Gerke, E., Kammerer, S., Koch, A., Peter, S., Vanzo, D., Vonwiller, L., Facchini, M., Gerber, M., Volz, C., Farshi, D., Mueller, R., Rousselot, P., Veprek, R. & Faeh, R. (2018), 'System Manuals of BASEMENT, Version 2.8. Laboratory of Hydraulics, Glaciology and Hydrology (VAW)'.
URL: *http://www.basement.ethz.ch.*

Vu, T. T., Nguyen, P. K. T., Chua, L. H. C. & Law, A. W. K. (2015), 'Two-Dimensional Hydrodynamic Modelling of Flood Inundation for a Part of the Mekong River with TELEMAC-2D', *British Journal of Environment & Climate Change (BJECC)* **5013**(2), 162–175.

Wang, J. W. & Liu, R. X. (2005), 'Combined finite volume-finite element method for shallow water equations', *Computers and Fluids* **34**(10), 1199–1222.

Webster, T., McGuigan, K., Collins, K. & MacDonald, C. (2014), 'Integrated river and coastal hydrodynamic flood risk mapping of the lahave river estuary and town of Bridgewater, Nova Scotia, Canada', *Water* .

Wirasaet, D., Kubatko, E. J., Michoski, C. E., Tanaka, S., Westerink, J. J. & Dawson, C. (2014), 'Discontinuous Galerkin methods with nodal and hybrid modal/nodal triangular, quadrilateral, and polygonal elements for nonlinear shallow water flow', *Computer Methods in Applied Mechanics and Engineering* **270**, 113–149.
URL: *http://dx.doi.org/10.1016/j.cma.2013.11.006*

Wirasaet, D., Tanaka, S., Kubatko, E. J., Westerink, J. J. & Dawson, C. (2010), 'A performance comparison of nodal discontinuous Galerkin methods on triangles and quadrilaterals', *International Journal for Numerical Methods in Fluids* **64**(August), 1336–1362.

Wood, D., Kubatko, E. J., Rahimi, M., Shafieezadeh, A. & Conroy, C. J. (2020), 'Implementation and evaluation of coupled discontinuous Galerkin methods for simulating overtopping of flood defenses by storm waves', *Advances in Water Resources* **136**(January 2019).

Xia, X., Liang, Q. & Ming, X. (2019), 'A full-scale fluvial flood modelling framework based on a high-performance integrated hydrodynamic modelling system (HiPIMS)', *Advances in Water Resources* **132**, 103392.
URL: *https://doi.org/10.1016/j.advwatres.2019.103392*

Xing, Y. (2016), 'High order finite volume WENO schemes for the shallow water flows through channels with irregular geometry', *Journal of Computational and Applied Mathematics* **299**, 229–244.
URL: *http://dx.doi.org/10.1016/j.cam.2015.11.042*

Xing, Y. & Shu, C.-W. (2014), 'A Survey of High Order Schemes for the Shallow Water Equations', *Journal of Mathematical Study* **47**(3), 221–249.

Yamamoto, S., Kano, S. & Daiguji, H. (1998), 'An efficient CFD approach for simulating unsteady hypersonic shock-shock interference flows', *Computers and Fluids* **27**(5-6), 571–580.

Yu, D. & Coulthard, T. J. (2015), 'Evaluating the importance of catchment hydrological parameters for urban surface water flood modelling using a simple hydro-inundation model', *Journal of Hydrology* .

Zhao, J., Özgen, I., Liang, D. & Hinkelmann, R. (2018), 'Improved multislope MUSCL reconstruction on unstructured grids for shallow water equations', *International Journal for Numerical Methods in Fluids* **87**, 401–436.

Zischg, A. P., Mosimann, M., Bernet, D. B. & Röthlisberger, V. (2018), 'Validation of 2D flood models with insurance claims', *Journal of Hydrology* **557**, 350–361.
URL: *https://doi.org/10.1016/j.jhydrol.2017.12.042*

Şen, O. & Kahya, E. (2017), ‘Determination of flood risk: A case study in the rainiest city of Turkey’, *Environmental Modelling and Software* **93**, 296–309.